

Scientific Research Associates, inc.

2

50 Nye Road, P.O. Box 1058
Glastonbury, Connecticut 06033
(203) 659-0333 FAX (203) 633-0676

AD-A275 264



R93-9245-F

FLUID DYNAMIC NOISE IN A CENTRIFUGAL PUMP

Final Report for Contract N00014-91-C-0172

by

D.G.N. Tse

Scientific Research Associates, Inc.
50 Nye Road, P.O. Box 1058
Glastonbury, CT 06033

and

J.H. Whitelaw

Imperial College
Exhibition Road
London SW7 2BX
England

This document has been approved
for public release and sale; its
distribution is unlimited.

August 1993

94 1 31 239

11096

94-03155



ABSTRACT

Pressure distributions and frequency spectra have been obtained in a centrifugal pump having flow rates between the design point and near shut-down. The pump was comprised of a radial flow impeller with four backswept blades and a single volute. Measurements were obtained at the design flow rate and at off-design conditions to advance understanding of noise generation, to quantify the contribution of tonal, narrowband and broadband components to the overall noise and to develop strategies for suppressing fluid dynamic noise by flow control and active control.

Fluid dynamic noise was generated by the unsteady conditions encountered by the impeller blade. Unsteady conditions originated from non-uniformities at the inlet and the impeller outlet at design and off-design conditions. Inlet flow non-uniformity was induced by separation regions. Flow separations are inherent in turbomachinery because of growth of the boundary layer and the disturbance effect of the rotating impeller. Flow non-uniformity at the impeller outlet stemmed from inlet flow non-uniformities in the inlet, from propagation of pressure waves in a vaneless diffuser, and from scroll effects. Fluid dynamic noise in the pump contained blade-tone, narrowband and broadband noises. The blade tone was of the order of 60 dB above the background level, the narrowband, 40 dB above background and broadband noise, 30 dB above background. Flow separation generated shear, turbulence and flow non-uniformity, which generated broadband noise. The broadband noise level increased with reducing the flow rate as a result of increased level of flow non-uniformity. The flow non-uniformity at the inlet is an important fluid dynamic noise generation source due to its subsequent interaction with the rotating impeller, an interaction that produced narrowband noise of magnitude greater than the broadband noise.

DTIC QUALITY INSPECTED &

Accession For	
NTIS CRA&I	<input checked="" type="checkbox"/>
DTIC TAB	<input type="checkbox"/>
Unannounced	<input type="checkbox"/>
Justification	
By <u>A249446</u>	
Distribution /	
Availability Codes	
Dist	Avail and/or Special
<u>A-1</u>	

1 . INTRODUCTION

This report discusses pressure measurements obtained with a miniature pressure transducer to investigate the links between fluid dynamics and noise generation in centrifugal pumps, to identify broadband and narrowband noise sources, to quantify their contributions to the overall noise level, and to develop strategies to suppress broadband and narrowband noise. This program is a follow-on investigation of an earlier ONR ARI program, Contract N00014-89-C-0090, which studied the fundamentals of broadband noise in centrifugal pumps. The findings of the earlier investigation have been documented in Tse, et al. (1992a). This two-year program was conducted by Scientific Research Associates (SRA) in collaboration with Imperial College. The findings of the first year are documented in Tse, et al. (1992b). The results presented in Tse, et al. (1992b) are included in this final report. Pressure measurements were obtained at SRA in a pump to characterize the acoustical behavior to complement the velocity measurements made at Imperial College for the same flow configuration. The corresponding frequency spectra of the pressure distributions were obtained by Fourier analysis to characterize the frequency content of the noise. Experimental rig and the contribution from Imperial College are presented in the Appendix. The commercially available centrifugal pump had four backswept blades on an impeller of five inch diameter and was operated at a rotational speed of approximately 3600 rpm at conditions which varied between the design flow rate and close to shut-off. The geometries, rotational speeds and flow conditions investigated are relevant to the pumps of naval vessels.

Fluid dynamic noise originates in the shear layers, wakes and separation bubbles of turbomachinery. It is known that careful management of shear layers can lead to fluid dynamic noise suppression (Schadow, et al., 1986), as can active control by the feed-back of pressure-based signals (Dowling and Ffowcs-Williams, 1983). In general, most research related to the performance of centrifugal machinery has focused upon compressors; see, for example, the investigations of Eckhardt (1976, 1980), Schodl (1984), Sideris and Van den Braembussche (1987), Khezzar, et al. (1987) and Paone, et al. (1989). In general, these references describe investigations confined to locations accessible through the inlet and limited regions of the impeller passage. Understanding of the performance of the compressors is based on a substantial body of literature, which is reviewed in Cumpsty (1989). These early studies include extensive measurements of wall pressure and velocity in the intake and exit ducts. Much less emphasis has been placed directly on pumps, partly because their performance is closely linked to that of compressors, with added assumption of incompressible flow, and partly because performance improvements in pumps have less

financial benefit than in high speed compressors. The study of Brentner (1990) showed that thickness, loading and quadrupole sources contribute to the pressure field that generates noise and that the quadrupole source is important at high Mach number (e.g. $M > 1$). His results further indicate that, in an incompressible flow, the thickness and loading sources alone determine the pressure perturbation, while the quadrupole source accounts for local kinetic energy in the fluid. Thus, noise generation mechanisms in centrifugal pumps are similar to those of compressors, but differences in flow conditions and geometry make a direct application of the results questionable. The main purpose of this effort is to study the phenomena that generate fluid dynamic noise in centrifugal pumps. A summary of recent studies focusing on flow characteristics of centrifugal pumps has been given by Miner, et al. (1989). The flow characteristics of the current pump have been reported in Liu, et al. (1991). However, pressure characteristics are also required and must be linked to the flow field to provide the essential understanding for noise generation.

The following section describes the flow configuration, the instrumentation and the possible sources of uncertainty. Pressure measurements are presented in Section 3. The implication of the results on fluid dynamic noise generation and their relationship to the velocity measurements published in Liu, et al. (1991) are discussed in Section 4. Methods of suppressing broadband and narrowband noise are described in Section 5. Summary conclusions are stated in the final section.

2. FLOW CONFIGURATION AND INSTRUMENTATION

Figure 1 shows the experimental arrangement, including the pump, the circuit for the temperature-controlled liquid, the laser velocimeter and the encoder which identifies the shaft position and rotating speed of the impeller. The centrifugal pump (Price model SC100-150) was driven by an electric motor at a speed of 3150 rpm (N) and circulated liquid from and to a 150 liter tank through 36 mm and 28.5 mm inlet and outlet pipes, respectively. The impeller, Figure 2, has four backswept blades of 2.5 mm thickness, with the blade height tapered from 11.2 mm at the 21 mm inner radius to 6.2 mm at the 62.7 mm outer radius. The clearance between the impeller tip and shroud was adjusted to 0.5 mm, smaller than the manufacturer's nominal value, and the resulting passage width was 11.7 and 6.7 mm at the radii of 21 and 62.7 mm, respectively, where the circumferential cross-section areas of the passage were 1427 and 2572 mm². The curve of the impeller blade was a logarithmic spiral with blade angle of around 30° in the entrance section between radii of 40 and 62.3 mm, with a smooth transition from 30 to 58° between radii of 20 and 40 mm.

The working fluid was a mixture of 68.2% (by volume) turpentine and of 1,2,3,4-tetrahydronaphthalene (tetraline) with density (ρ) and kinematic viscosity (ν) of 0.893 kg/m^3 and $1.74 \times 10^{-6} \text{ m}^2/\text{s}$, respectively, at 25°C . The mixture was maintained at a temperature of $25 \pm 0.2^\circ\text{C}$ by a temperature controller, with a heater and cooler installed within the storage tank and a platinum resistance sensor near the pump outlet to maintain a refractive index of 1.49, identical to that of the cast acrylic. The flow rate of the mixture was regulated between 2.52×10^{-3} and $4 \times 10^{-4} \text{ m}^3/\text{s}$ by a valve downstream of the pump outlet, which corresponded to a range of flow coefficients (Φ) between 0.054 and 0.0086. The design flow coefficient was 0.058 and the pressure and velocity measurements were obtained at up to 93% of the design flow coefficient because of pressure losses in the pipework. The flow rate was measured by a turbine meter with an accuracy of better than 3%.

A rotating system includes a Coriolis force, which is important when its magnitude is comparable with the other forces in the system, i.e., the inertial and viscous forces. The non-dimensional parameters of Ekman (Ek) and Rossby (Ro) numbers are defined based on the ratio of viscous to Coriolis forces and inertial to Coriolis forces, respectively, and allow an estimate of the relative importance of the forces in the system. Typical values of the Ekman and Rossby numbers were calculated based on the impeller diameter and tip velocity as 3.4×10^{-7} and 0.5, respectively, and suggest similar magnitudes for the Coriolis and inertial forces and a smaller value for the viscous force, except in the boundary layer, where the three can have similar values.

The design point of a pump with a volute diffuser is determined from the criteria of equal angular momentum of the flow at the impeller discharge and at the throat of the volute, (Karassik, et al., 1976). This usually corresponds to the condition of highest efficiency, and depends on the rotating speed. The flow rate at the design point of the pump running at 3510 rpm was $3.26 \times 10^{-3} \text{ m}^3/\text{s}$ (Q_n), based on theoretical velocities at the impeller discharge plane and at the throat of the volute, which is equivalent to a flow coefficient of 0.058. The flow conditions for the pressure measurements comprised a range of flow rates from 93% to approximately 15% of the design flow rate, presented in Table 1, which also provides the conditions of the velocity measurements obtained in a parallel investigation conducted at Imperial College, Liu, et al. (1991). The rotational speeds of the impeller were different for the velocity and pressure measurements; the former was conducted at 2910 rpm and the latter at 3510 rpm. The difference is attributed to the main power supply available to the two institutes. Since the design flow rate and the flow coefficient are both dependent on the rotational speed, the pressure measurements were obtained at 3.02×10^{-3} , 1.88×10^{-3} , 9.60×10^{-4} and $4.0 \times 10^{-4} \text{ m}^3/\text{s}$ to match the flow coefficients of the velocity

measurements obtained at 0.93, 0.57, 0.29, and 0.15 Q_n . This allow a direct comparison of the velocity and pressure results. Pressure measurements were also obtained at flow rates of 2.52×10^{-3} , 1.57×10^{-3} and 8×10^{-4} m^3/s , which corresponded to flow rates of 0.77, 0.49 and 0.24 Q_n , to assist the understanding of the differences observed between each condition. The original cast stainless steel casing of the pump was used in the pressure measurements and was replaced by a cast acrylic component of rectangular external shape and internal dimensions identical to those of the metal components in the velocity measurements, Liu, et al. (1991). The internal dimensions were measured and found to be within 0.5 mm of those of the stainless steel casing. The performance of the two pumps is characterized by the head coefficient (Γ) of Figure 3, which shows that it is almost identical to that of the manufacturer's specification with the metal casing, and is higher with the perspex casing by 18% near the design flow coefficient and by 15% near shut-down. The differences are probably due to the smaller impeller tip clearance (≈ 0.5 mm) and the machined and polished inner surfaces of the perspex casing, which reduced the leakage flow and friction.

A Kulite miniature transducer was used for pressure measurements inside the casing and the scroll. The transducer was flush mounted on the shroud wall at $\Psi = 0, 20, 40, 110, 150, 210, 270, 300$ and 330° at a radius of 62 mm to obtain time-resolved measurements which provide a circumferential pressure distribution at the edge of the impeller. The measuring position was selected by installing the miniature transducer at the appropriate pressure tap. The data acquisition system was based on an IBM/PC-compatible microcomputer with the triggering provided by the shaft encoder. The data acquisition hardware obtained instantaneous pressure measurements throughout the 360° rotation as a function impeller angle. A marker pulse from the shaft encoder identified the starting angle for each rotation. The processing software was specially developed for these rotating machinery studies and provided values of ensemble averages of each single-trace distribution at each location.

The miniature pressure transducer involved an uncertainty of 3% and the measurements presented in Section 3 show that the pressure gradient is less than 1% of the local pressure so that spatial-gradient broadening is insignificant. Statistical uncertainty in the mean pressure measurements associated with a finite sample size can be estimated using the equation:

$$\overline{U}_c = \frac{S}{\sqrt{N}} \times \frac{\sqrt{u^2}}{U} \quad [1]$$

where S is equal to 2 for a 95% confidence limit. The sample size in each ensemble average was 330 and the turbulence intensities were below 16% in all cases. The resulting statistical uncertainty was less than 2% in each ensemble-averaged pressure. The corresponding uncertainty in the rms values can be estimated from the expression:

$$\sqrt{u_c^2} = \frac{S}{\sqrt{2N}} \quad [2]$$

which indicates, with 95% confidence, an accuracy of better than 7% for the sample size used in the measurements. The above analysis indicates that the overall uncertainty in the mean and rms pressure measurements was less than 4% and 8%, respectively.

3. RESULTS

The coordinate systems of the experiment are identified in Figure 2 and were chosen to facilitate presentation of results in different parts of the pump and in absolute and rotating frames. The inlet and exit flows are described by the stationary Cartesian coordinates, x - y - z , located in the inlet and exit pipes, respectively, and the absolute flows in the impeller and volute are described by the cylindrical coordinates, r - Θ - z , located in the volute, with an additional set of cylindrical coordinates, r - θ - z , for the relative flow within the impeller. The impeller shaft angle ϕ was measured in a counter-clockwise direction, with its origin at $\Psi = 330^\circ$. The exit pipe was normal to the plane of $\Psi = 330^\circ$, which was also the origin of the x -coordinate in the exit pipe. The relative angular coordinate on the impeller, Ω , was measured in a direction from suction to pressure surface, with its origin at the center of the blade thickness. The velocity measurements were based on a stationary probe volume with the angle-dependent velocity resolved according to the impeller and volute identified by the volute circumferential angle, Ψ , measured in a counter-clockwise direction from the cutwater, which was on an angular plane 30° to that of $\Psi = 330^\circ$.

Preliminary measurements were obtained with a sampling frequency of 21.6 kHz and led to a resolution of around 21 Hz in spectra of up to 10.8 kHz. The initial results, Figure 4a, show a fundamental frequency of around 240 Hz and another 10 harmonic frequencies, with the eleventh harmonic just distinguishable from the background level. In Figure 4, the frequency has been normalized by 240 Hz. The initial results were obtained to cover a broad spectrum to identify the frequency range of interest. These results showed that there was nothing of interest above 2.7 kHz and most of the energy in the spectra was in the

frequencies below 1.35 kHz. Results obtained with a sampling frequency of 5.4 kHz, Figure 4b, indicate the same eleven harmonic frequencies, but fail to resolve the narrowband noise. The subsequent sampling frequency used to obtain the pressure measurements was 2.7 kHz. This leads to a resolution of 2.6 Hz in the frequency spectra of up to 1.35 kHz and provides a detailed examination of the high amplitude spikes. Figures 5a to 5i show the ensemble-averaged static pressure distributions obtained at a flow rate of 0.93 Q_n and an angular speed of 3510 rpm at nine circumferential locations on the shroud wall. The frequency spectra at various angular positions show that the pressure distributions at these locations are generated by sinusoids of different amplitudes and frequencies at multiples of approximately 60 Hz (speed of rotation) and 240 Hz (fundamental of the blade tone). The amplitude of the fundamental frequency at all circumferential locations is approximately 55 dB above the background level, the second harmonic, 50 dB, the third, 45 dB, the fourth, 40 dB and the fifth 35 dB. Similar amplitudes are observed in those spectra obtained at flow rates of 0.57 and 0.15 Q_n , Figures 6a-6i and Figures 7a-7i. Similar results are obtained with the remaining conditions, 0.77, 0.49, 0.29 and 0.24 Q_n ; therefore, they are not presented here. The overall intensity of the blade tone is represented by the sum of the fundamental frequency and its harmonics and is of the order of 60 dB above the background level. Noise generation is strongly related to local pressure gradient, Beard, et al. (1978). The steep pressure gradients associated with the blade wake identified in Figures 5 to 7 are attributed to the blade wakes which are responsible for the blade tone.

Figures 8a to 8f show the ensemble-averaged static pressure distribution at $\Psi = 330^\circ$ as a function of flow rate. Measurements obtained at 0.24 Q_n are not presented here because they are similar to those obtained at 0.29 and 0.15 Q_n . The 60 Hz spike in the results of Tse, et al. (1992a) was initially thought to originate from geometrical variation of the impeller. The inlet velocity profiles presented in Liu, et al. (1991) shows that the inflow at 0.93 Q_n is very uniform and the blade-to-blade variations in the pressure distribution at the impeller outlet at 0.93 Q_n , Figure 8a, are very small. The blade-to-blade variations in the pressure distribution increased considerably as the flow rate reduced, Figures 8b to 8f, and the velocity measurements of Liu, et al. (1991) show large variations in the inlet velocities. Geometrical influence will be consistent; it affects all the flow rates evenly and is shown to be small in the pressure distribution of Figures 8a to 8f. Thus, the increase in blade-to-blade variation at reduced flow rates is a direct influence of the asymmetry in the inlet flow and is induced by flow non-uniformity, rather than geometrical non-uniformity.

According to Groeneweg and Rice (1987), the primary noise generation mechanism in turbomachinery with subsonic tip speeds is the unsteady fluctuations encountered by the blade. In spectral terms, random fluctuations produce broadband or narrowband noise.

Narrowband noise is produced by repeated chopping of the large scale turbulence eddies. The resulting noise radiation contains random frequency peaks at discrete multiples, Brooks and Schlinker (1982). The spatial jittering of the large scale eddies, relative to the impeller blade, can give rise to Doppler shifts. Doppler shifts are not observed in the current results. Thus, the jittering of the large scale eddies is small in the current setup. The small scale turbulence eddies, which do not experience multiple chopping, contribute to broadband noise of the fluctuation. Comparison of the distributions obtained with ensemble-averaged distribution and with instantaneous single point trace obtained with flow rates between 0.93 and 0.15 Q_n , Figures 8a to 8f with Figures 9a to 9f, shows that the background noise level of the former (the ensemble average) is 15 to 20 dB lower than that of the latter (the instantaneous) and that the 60 Hz spike and its harmonics are only evident in the ensemble-averaged spectra. These findings indicate that the tonelike 60 Hz spectrum and its harmonics are intermittent in nature and they represent narrowband noise. Fluid dynamic noise associated with the current pump, attributed to unsteady flow, contains both broadband and narrowband noise. The relative importance of the broadband and narrowband noise is indicated by the relative spectral level. The broadband noise can be identified by the differences in background noise level between the ensemble-averaged measurements and instantaneous measurements, Figures 8a to 8f and 9a to 9f. The overall magnitude of the narrowband noise is the sum of the 60 Hz spectrum and its harmonics and is of the order of 40 dB above the background level. Ensemble averaging has a tendency of reducing the signature of the random fluctuations which produce broadband noise. It is evident from the figures that the broadband noise is of the order of 15 to 20 dB above background for the flow rates above 0.49 Q_n and is roughly 30 dB above background for flow rates below 0.29 Q_n . Thus, the broadband noise level at near shut-off conditions is 10 dB higher than that at design conditions, i.e., at least 3 times stronger. Furthermore, the narrowband noise level is 10 to 20 dB higher than that of broadband noise, i.e., 3 to 10 times stronger, and will have a stronger effect on the far-field sound characteristics.

Circumferential variations are evident in the pressure distributions, Figures 5 to 7, and the velocity distributions of Liu, et al. (1991). They are induced by flow non-uniformity at the inlet and the impeller outlet and the former is clearly evident in the inlet velocity profiles (Liu, et al., 1991). Inlet flow disturbances can be divided into two categories: those originating external to the pump and drawn into the inlet and those originating inside the pump. The non-uniformity in the inlet is attributed to growth of boundary layer induced by friction, to viscous drag of the impeller, to reverse flow in the impeller, and to propagation of swirl associated with the disturbance of the rotating impeller, Breuglemans and Sen (1982), Japikse (1984), Kammer and Rantenberg (1985) and Tse, et al. (1991). Thus, the

inlet flow non-uniformity will originate within the pipework and from the disturbances of the rotating impeller itself, even if the inflow supply can deliver a uniform, fully-developed, turbulent profile. It has long been recognized that ingested disturbances affect noise generation in turbomachinery, Hanson (1974), and inlet flow control of Tyler and Sofrin (1962) has shown to greatly reduce the fundamental blade tone. Thus, the influence of inlet flow disturbances can be minimized by using appropriate inlet control introduced by means of suitable guide vanes. A fixed inlet guide vane is optimized at one condition and may be ineffective when the operation condition changes. Retractable vortex generators and jet vortices used in aircraft engine inlet flow control can operate over a wide range of conditions and their potential in suppression of broadband and narrowband noise by flow control and active control are worth investigating. This approach is further discussed in Section 5. The finding of Tyler and Sofrin (1962) indicates that the interaction of rotating impeller and inlet flow disturbances gives rise to blade tone. However, their research effort was on blade tone and earlier discussion showed that the resolution of the frequency is dependent on sampling frequency. The frequency spectra of Figures 8a to 8f and 9a to 9f show clearly that the narrowband and broadband noise changes with flow rate, i.e., variation in inlet velocity profiles. Increases in flow separation, shear, turbulence and flow non-uniformities are clearly evident in the velocity measurements presented in Liu, et al. (1991). Comparison of the velocity and pressure measurements indicates that higher shear, turbulence and flow non-uniformity associated with increased flow separation at reduced flow rates leads to higher levels of broadband noise. Thus, broadband noise generation in centrifugal pumps is attributed to separation regions, which augment the production of shear, turbulence and flow non-uniformities in their vicinities. The flow non-uniformity and separation in the inlet are of extreme importance in fluid dynamic noise generation. The flow non-uniformity itself generates broadband noise (15 to 20 dB). The inlet flow non-uniformity ingested into the pump will subsequently interact with the rotating impeller to produce narrowband noise (40 dB) of magnitude considerably greater than that of the broadband noise.

4. DISCUSSION

Since the pump has an asymmetric volute diffuser, the circumferential variations of pressure and velocity are induced by the geometrical influence of the volute diffuser. According to Sideris and Van den Braembussche (1987), there is only one operating point per constant-speed line for which the volute-type collector imposes a circumferentially uniform pressure at the diffuser outlet. At smaller mass flows, the volute acts like a diffuser, resulting in a static pressure rise between the volute inlet ($\Psi = 0^\circ$) and the outlet. At larger mass flows, the volute is too small and the flow accelerates, resulting in a decreasing pressure from the volute inlet to outlet. The velocity measurements, Liu, et al. (1991), showed that the velocities in the volute passage decelerated in the circumferential direction at off-design condition $0.57 Q_n$, when the geometry of the volute was over-sized. The maximum circumferential variation in the pressure distributions at $0.93 Q_n$ (Figure 5c and 5i) and $0.57 Q_n$ (Figure 6c and 6i) are 13% and 25%, respectively. The corresponding variation in the velocity distribution at $0.57 Q_n$ is 25%. As expected, pressure and velocity distributions are interrelated so that the same order of difference is observed in the circumferential variation. An asymmetric volute diffuser gives rise to different volute pressure at different angular positions and in the case of a vaneless diffuser, this volute pressure distribution propagates and results in non-uniformity outlet conditions for the rotating impeller. Thus, circumferential variations of velocity and pressure will exist, even if the inlet condition is uniform. The non-uniform velocity and pressure distribution at the impeller outlet impose a circumferential variation of blade loading and result in net uneven radial forces acting on the impeller shaft, Senoo and Ishida (1986). The uneven radial forces generate out-of-balance vibration and consequently act as a 60 Hz tonelike narrowband noise source. Interaction of diffuser guide vanes and impeller outlet flow disturbances is a major noise source in turbomachinery. However, the current results show that the interaction of the rotating impeller with disturbance generated by itself leads to fluid dynamic noise of around 60 dB above the background level. Furthermore, the unsteady rotor outlet flow gives rise to extra losses which affect the surge limit, e.g., Klassen, et al. (1977, 1978), Ishida and Senoo (1981) and Harada (1985), and flow uniformity in the exit pipe. There is no disturbance source in the exit pipe to interact with the non-uniformity to act as a major noise source. The non-uniformity in the pipe will be dampened by natural turbulence and its effect will diminish with increasing downstream distance. In addition, noise associated with flow non-uniformity in the exit pipe can be attenuated by lining the pipe wall with sound-absorbing material. Surge affects cavitation and stall, which in turn have drastic influence on vibration and noise generation. Currently, very little information is

available on cavitation and stall to determine whether noise associated with cavitation and stall is tonal, narrowband or broadband. Circumferential pressure variation affects the vorticity field, which influences the generation of fluid dynamic noise. Potential theory suggests that any circumferential variation of radial velocity at the exit of a backswep impeller leads to a decrease in the torque. Experiments conducted by other researchers do not confirm this prediction. One can conclude that the real flow is not irrotational and that the circumferential variations of velocity and pressure give rise to trailing edge vorticities, Ishida and Senoo (1981). Broadband noise generation is strongly related to vorticities. An increase in vorticity increases circulation and consequently leads to increase in lift. Broadband noise generation is related to lift and the first derivatives of lift (Equation [3]) or the lift coefficient and the first derivatives of the lift coefficient (Equation [4]), Ho (1993).

$$S(t) = k_1'[L(t) + k_2' dL(t)/dt] \quad [3]$$

$$S(t) = k_1[C_L(t) + k_2' dC_L(t)/dt] \quad [4]$$

Where $S(t)$ denotes broadband noise level, k_1' , k_2' , k_1 and k_2 are constants and $L(t)$ and $C_L(t)$ denote lift and lift coefficient. Vorticity contributes to the first terms in Equations [3] and [4]. In addition, a small deflection in the vorticity field can result in strong secondary flows. Broadband noise generation is strongly related to secondary flow, Quandt (1992). Mass variation in the recirculation bubble induces changes in the inertia of the bubble. The bubble behaves like a Joukowski Airfoil and changes in circulation in the bubble induce fluctuation in lift. Lift fluctuation contributes to the first terms in Equations [3] and [4]. A recirculation bubble increases the turbulent intensity in its vicinity and increases the fluctuations that generate noise. Blade wake generates mainly blade tone noise, but the unsteady conditions in a wake would generate narrowband and broadband noise which can be quantified by the pressure distribution in the volute diffuser.

The current investigation shows that, consistent with the finding of Groeneweg and Rice (1987), fluid dynamic noise is generated by unsteady conditions encountered by the impeller blade. Unsteady conditions originate from non-uniformities at the inlet and at the impeller outlet at design and off-design conditions. Inlet non-uniformity is induced by boundary layer flow and by the propagation of the disturbance effect associated with the rotating impeller. Flow non-uniformity at the impeller outlet is induced by transient acceleration and deceleration of the volute flow and by propagation of volute pressure in a vaneless diffuser.

5. RECOMMENDATIONS

A prime objective of this program has been to develop new strategies to suppress fluid dynamic noise in centrifugal pumps. This section considers new methods of reducing fluid dynamic noise based on the pressure and velocity measurements described in Section 3 and the Appendix.

Fluid dynamic noise is generated by flow non-uniformity and secondary flows. Engine face flow distortion is one of the most troublesome and least understood problems for designers of modern inlet engine systems, AGARD 1986 and Bowditch and Coltrin (1983), because there are numerous sources of flow field distortion that are ingested by the inlet and generated by the inlet duct itself. Fluid dynamic noise in centrifugal pumps is generated by flow non-uniformity. Similar to engine face flow distortion, flow non-uniformity encountered in centrifugal pumps can be generated by ingestion of external fluctuations or fluctuations generated by the pumps and the associated pipework. Pump inlet flow non-uniformity and engine face flow distortion are two similar problems and may have a common solution. Vortex generators are commonly used in the aircraft industry to control engine face flow distortion. The use of vortex generators may also be an effective and economic means of controlling broadband and narrowband noise in ship-board machinery. Vortex generators in use today are small wing sections mounted on the inside surface of the inlet, inclined at an angle to the oncoming flow, to generate shed vortices. The generators are usually sized to the local boundary layer height for best interaction between the shed vortices and boundary layer, and are usually placed in groups of two or more, upstream of the problem area. The principle of boundary layer control by vortex generators relies on induced mixing between the cross-flow and the boundary layer. This mixing is promoted by vortices trailing longitudinally near the edge of the boundary layer. Fluid particles with high momentum in the streamwise direction are swept along helical paths towards the duct surface to mix with and, to some extent, replace the low momentum boundary layer flow. This is a continuous process that provides a source of re-energization to counter the natural boundary layer growth caused by friction, adverse pressure gradients, and low energy secondary flow accumulation.

Counter-rotating, equal strength generators have been used in a number of aircraft ducts. These types of vortex generators are very effective in reducing flow separation if the vortex generators are placed slightly upstream of the region of separation. The disadvantage of these types of generators, as opposed to co-rotating generators, is that the induced vortices tend to lift off the surface, thus reducing their effectiveness and causing higher loss. The main advantage of co-rotating vortex generators is their downstream

effectiveness and a more effective usage of the vortex energy within the affected boundary layer. The induced vortices will remain close to the wall and consequently a less disturbed cross-flow will result. Similar fluid dynamic behavior is expected in a centrifugal pump. Co-rotating vortex generators would be preferred on the grounds that they would yield a more uniform cross-flow.

Anderson and Levy (1988) indicated that there exists an optimum axial location for the installation of co-rotating vortex generators, and within the configuration they investigated, there exists a maximum spacing between generator blades above which engine face distortion increases rapidly. Installed vortex generator performance is sensitive to Reynolds number and thereby the generator scale, i.e. the ratio of generator blade height to local boundary layer thickness. Installations of co-rotating vortex generators work well in terms of minimizing engine face distortion within a limited range of generator scale. Thus, the design of a vortex generator installation system is a point design, and all other conditions are off-design. Active control is thus needed to achieve the flow control necessary for noise reduction over a wide range of conditions. Retractable vortex generators can adjust for variations in flow conditions by changing the scale in a controlled manner. However, the boundary layer thickness encountered in centrifugal pumps is expected to be much smaller than that in aircraft intake ducts and the much smaller scale creates problems in controlling the movement of the vortex generator. The energization of the low momentum near-wall fluid can alternatively be accomplished by injection of fluid jet. The injection process can be controlled by fast-response solenoid valves driven by the feed-back of pressure-based signals. The high pressure fluid can be channeled from the exit of the pump. Only a small amount of fluid is required to counter boundary layer growth to remove separation regions and low noise levels can be achieved without a heavy penalty in efficiency over a wide range of conditions.

6. CONCLUSIONS

Pressure measurements and the corresponding frequency spectra have been obtained for several conditions to provide a better understanding of the physical mechanisms associated with noise generation in centrifugal pumps. The results also provide a basis for a future investigation of active control of hydrodynamic noise of centrifugal pumps. The following conclusions can be extracted from the results obtained at flow rates in the range 93% to 15% of the design flow rate and impeller speed of 3510 rpm:

1. Fluid dynamic noise was generated by the unsteady conditions encountered by the impeller blade. Unsteady conditions originated from non-uniformities at the inlet and the impeller outlet at design and off-design conditions. Inlet flow non-uniformity was induced by separation regions. Flow separation is inherent in turbomachinery because of growth of the boundary layer, the adverse pressure gradients encountered, and the disturbance effect of the rotating impeller. Flow non-uniformity at the impeller outlet was induced by inlet flow non-uniformity, by transient acceleration and deceleration of the volute flow, and by propagation of pressure wave in a vaneless diffuser. Fluid dynamic noise in the current pump contained blade-tone, narrowband and broadband noises. The blade tone was of the order of 60 dB above the background level and the narrowband, 40 dB above background. The broadband noise level was 15 to 20 dB above background for the design flow rate and for near shut-off conditions, 30 dB above background.

2. Flow separation generated shear, turbulence and flow non-uniformity, which generated broadband noise. Broadband noise level increased with reducing flow rate because of an increased level of flow non-uniformity. Flow non-uniformity at the inlet was important in fluid dynamic noise generation because subsequent interaction with the rotating impeller produced narrowband noise of greater magnitude.

3. Flow non-uniformity in the impeller outlet led to circumferential variations of pressure, which increased with reducing flow rate. Circumferential variations of pressure led to an uneven radial force and resulted in out-of-balance vibration, which generated a 60 Hz narrowband noise. The variations gave rise to trailing edge vorticities, which affected the flow characteristics within the blade passage, as well as tip vortices, tip leakage and blade wake. The disruption of uniformity by trailing edge vorticities led to flow non-uniformity and recirculation and the effect was more noticeable at low flow rate because the cross-flow had a low momentum. Mass variation in the recirculation bubble induced changes in inertia of the bubble and lift forces on the impeller, which led to fluctuations that generated narrowband and broadband noises. A recirculation bubble increased the turbulent intensity in its vicinity and increased the fluctuations that generate noise.

4. The unsteady rotor outlet flow resulted in fluctuations in the exit pipe. Flow non-uniformity in the exit pipe was not a major noise source because there was no disturbance with which it could interact. The non-uniformity would be dampened by natural turbulence and its effect would diminish with increasing downstream distance.

5. The blade-to-blade variations increased considerably as the flow rate reduced. The increase in blade-to-blade variation at reduced flow rate was attributed mainly to flow asymmetry and was induced by flow non-uniformity, rather than geometrical non-uniformity.

ACKNOWLEDGEMENTS

This work was carried out under ONR ARI Program Contracts N00014-89-C-0090 and N00014-91-C-0172, in collaboration with Imperial College, whose assistance at all stages of the program is acknowledged. Thanks are due to Mr. Gary Winch of SRA for maintenance of the experimental facilities.

REFERENCES

Advisory Group for Aerospace Research Development - AGARD (1986) Engine Response to Distorted Inflow Conditions. AGARD CP-400.

Anderson, B.H. and Levy, R.(1988) A Design Strategy for the Use of Vortex Generators to Manage Inlet-Engine Distortion Using Computational Fluid Dynamic.

Beard, M.G., Pratt, C.M. and Timmis, P.H. (1978) Recent experience on centrifugal compressors for small gas turbines. ASME Paper No. 78-GT-193.

Bowditch, D.N. and Coltrin, R.E. (1983) A Survey of Inlet Engine Distortion Compatibility, AIAA-83-1166.

Brentner, K.S. (1990) The sound of moving body, Ph.D. thesis, University of Cambridge.

Brooks, T.F. and Schlinker, R.H. (1983) Progress in rotor broadband noise research. Vertica, Vol. 7, No. 4, pp. 287-307.

Breuglemans, F.A.E. and Sen, M. (1982) Prerotation and fluid recirculation in the suction pipe of centrifugal pumps, Proc. 11th Annual Turbomachinery Symposium, Texas A&M University, pp. 165-180.

Cumpsty, N.A. (1989) Compressor Aerodynamics. Longman, U.K.

Dowling, A.P., and Ffowcs-Williams, J.E. (1983) Sound and Sources of Sound. Ellis-Howard Publishers.

Eckhardt, D. (1976) Detailed flow investigations within a high-speed centrifugal compressor impeller. *J. Fluids Eng., Trans. ASME*, 98, 390.

Eckhardt, D. (1980) Flow field analysis of radial and backswept centrifugal compressor impellers. Part 1: flow measurements using a laser velocimeter. in *Performance Prediction of Centrifugal Pumps and Compressors*, ASME Paper 77.

Groeneweg, J.F. and Rice, E.J. (1987) Aircraft turbofan noise, *J. Turbomachinery*, Trans. ASME, 109, 130.

Hanson, D.B. (1974) Spectrum of rotor noise caused by atmospheric turbulence. *J. Acoustical Soc. of America*, 56, 110-126.

Harada, H. (1985) Performance characteristics of shrouded and unshrouded impellers of a centrifugal compressor. *J. Eng. for Gas Turbines and Power*, Trans. ASME, 107, 528.

Ho, C-H., (1993) Physical Mechanism of axial fan noise. Mechanical, Aerospace and Nuclear Engineering Department, University of California, Los Angeles, L.A. California 90024. Personal Communication.

Ishida, M. and Senoo, Y. (1981) On the pressure losses due to the tip clearance of centrifugal blowers. *J. of Eng. for Power*, Trans. ASME, 103, 271.

Japikse, D. (1984) A critical evaluation of stall concepts for centrifugal compressors and pumps - Studies in component performance, Part 7, Instability, Stall and Surge in Compressors and Pumps, ASME, Dec. 1984.

Kammer, N. and Rautenberg, M. (1985) A distinction between different types of stall in centrifugal compressor stage, ASME Paper No. 85-GT-123.

Karassik, I.J., Krutzsch, W.C., Fraser, W.H. and Messina, J.P. (editors) (1976) Pump Handbook. McGraw-Hill Inc.

Khezzar, L., Vafidis, C. and Whitelaw, J.H. (1987) Laser velocimetry for the measurement of air velocity in a centrifugal compressor. Imperial College, Fluids Section Report FS/87/36.

Klassen, H.A., Wood, J.R. and Schumann, L.F. (1977) Experimental performance of a 16.10-centimeter-tip-diameter sweptback centrifugal compressor designed for a 6:1 pressure ratio. NASA Technical Memorandum X-3552.

Klassen, H.A., Wood, J.R. and Schumann, L.F. (1977) Experimental performance of a 13.65-centimeter-tip-diameter tandem-bladed sweptback centrifugal compressor designed for a pressure ratio of 6. NASA Technical Paper 1091.

Liu, C.H., Vafidis, C. and Whitelaw, J.H. (1991) Flow characteristics in a centrifugal pump. University of London, Imperial College Report TF/91/31.

Miner, S.M., Beaudoin, R.J. and Flack, R.D. (1989) Laser velocimeter measurements in a centrifugal flow pump, *J. Turbomachinery*, Trans. ASME, 111, 205.

Paone, N., Riethmuller, M.L. and van den Braembussche, R.A. (1989) Experimental investigation of the flow in the vaneless diffuser of a centrifugal pump by particle image displacement velocimetry. *Exp. in Fluids*, 7, 371.

Quandt, E., (1992) The application of unsteady potential flow vortex loop/dipole theory to the work and acoustics of low-speed turbomachinery, DTRC-PAS-91/55. David Taylor Research Center, Bethesda, MD 20084-5000.

Schadow, K.C., Gootmark, E., Parr, T.P., Parr, D.M., and Wilson, K.J. (1986) Massive shear flow control to minimize ramjet combustion instabilities. Proceedings 23rd JANNAF Combustion Meeting.

Schodl, R. (1984) Optical techniques for turbomachinery flow analysis. Lecture to NATO Advanced Study Institute on Thermodynamics and Fluid Mechanics of Turbomachinery, held in Turkey.

Senoo, Y. and Ishida, M. (1986) Pressure loss due to the tip clearance of impeller blades in centrifugal and axial blowers. *J. of Eng. for Gas Turbines and Power*, ASME, 108, 32-37.

Sideris, Th.M. and van den Braermbussche, R. A. (1987) Influence of a circumferential exit pressure distortion on the flow in an impeller and diffuser," *J. of Turbomachinery*, Trans. ASME, 109, 48.

Tse, D.G.N., Sabnis, J.S., and McDonald, H. (1991) Velocity and Pressure Characteristics of a Model SSME High Pressure Fuel Turbopump, Scientific Research Associates Report R91-900065-F.

Tse, D.G.N., Sabnis, J.S., McDonald, H. and Whitelaw, J.H. (1992a) Active control of pressure, sound and velocity of centrifugal pumps. Scientific Research Associates, Inc., Report R91-920036-F.

Tse, D.G.N., Kreskovsky, J.P. and Whitelaw, J.H., (1992b) Active control of pressure, sound and velocity of centrifugal pumps, Scientific Research Associates Report R92-920045-A.

Tyler, J.M. and Sofrin, T.G. (1962) Axial flow compressor noise studies. *SAE Trans.*, 70, 309-332.

Table 1. Experimental Conditions.

VELOCITY MEASUREMENTS (2920 rpm $W_{tip} = 19.7$ m/s)

FLOW CONDITION	1	2	3	4
$Q(m^3/s) \times 10^{-3}$	2.52	1.57	0.80	0.40
Q / Q_n	0.93	0.57	0.29	0.15
Re_{exit}	69,000	43,000	22,000	11,000

PRESSURE MEASUREMENTS (3510 rpm $W_{tip} = 23.65$ m/s)

FLOW CONDITION	I	1a	2	2a	3	3a	4
$Q(m^3/s) \times 10^{-3}$	3.02	2.52	1.88	1.57	0.96	0.80	0.40
Q / Q_n	0.93	0.77	0.57	0.49	0.29	0.24	0.15
Re_{exit}	83,000	69,000	51,000	43,000	26,000	22,000	11,000

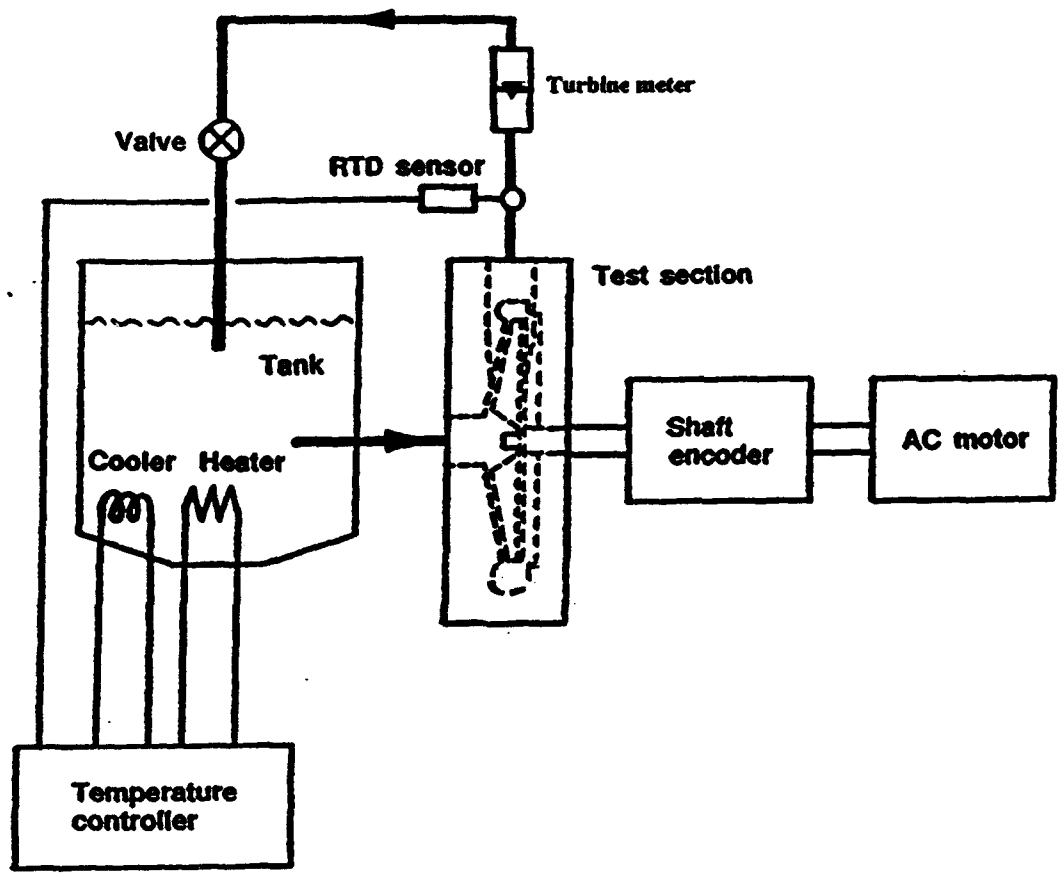


Figure 1. Flow configuration and instrumentation.

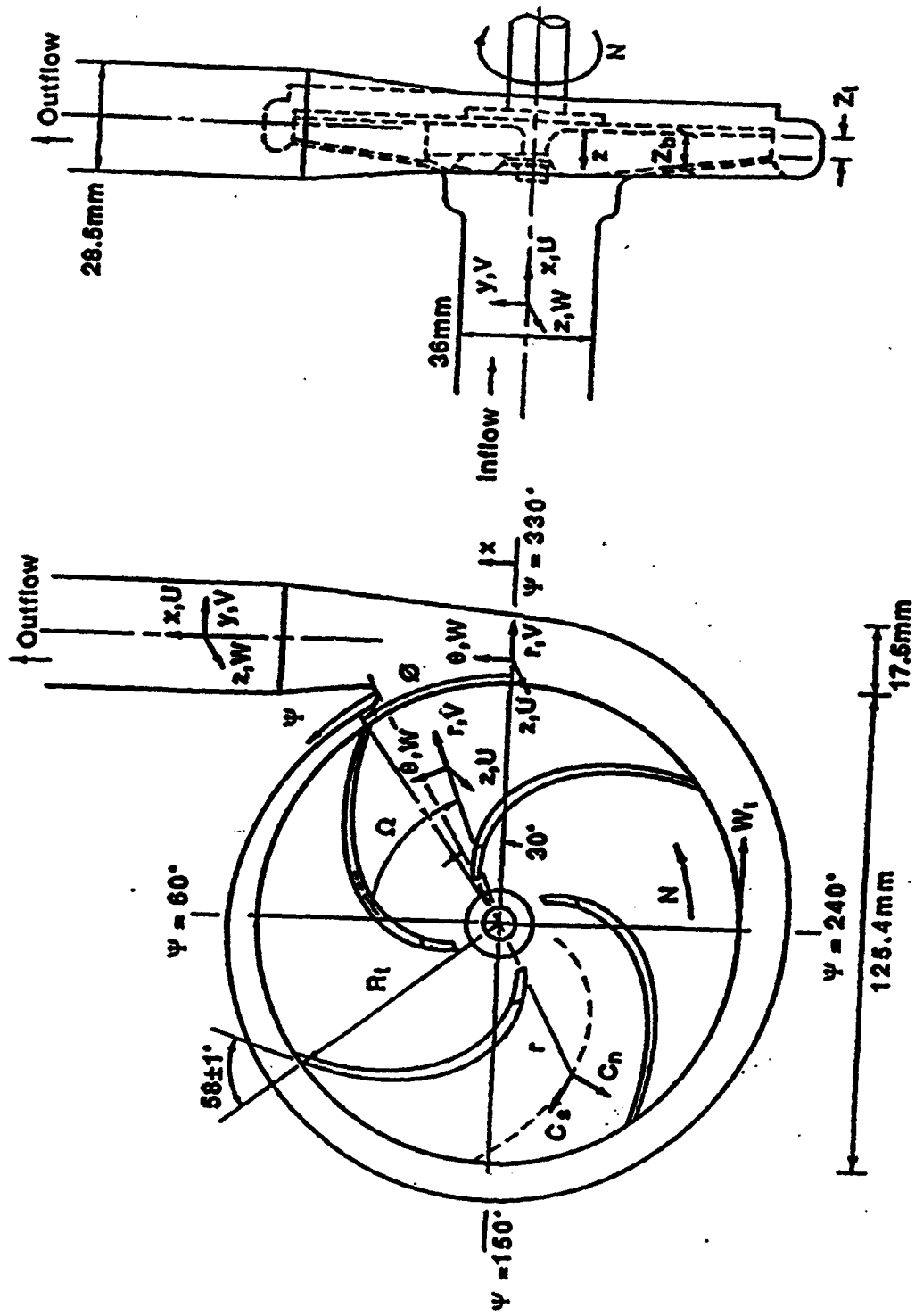


Figure 2. Dimensions of the centrifugal pump and coordinate systems.

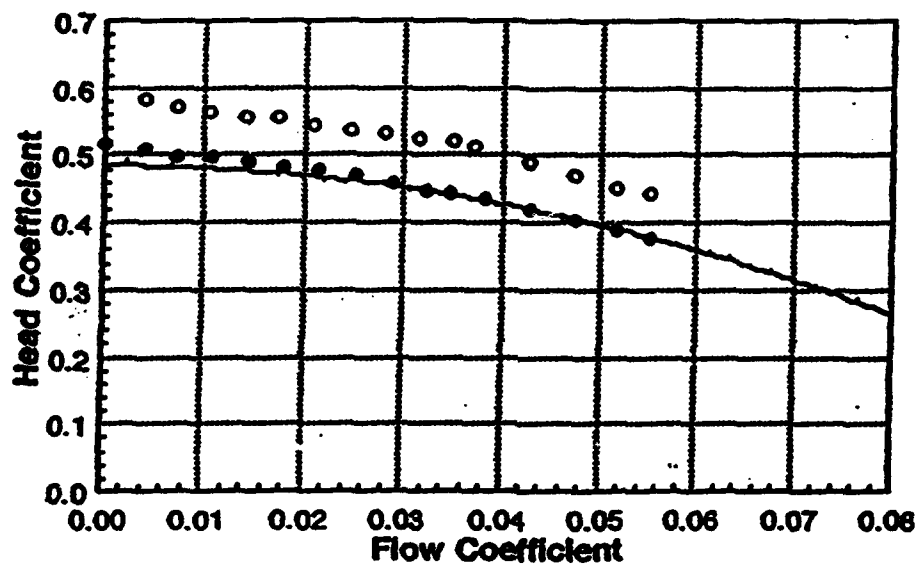
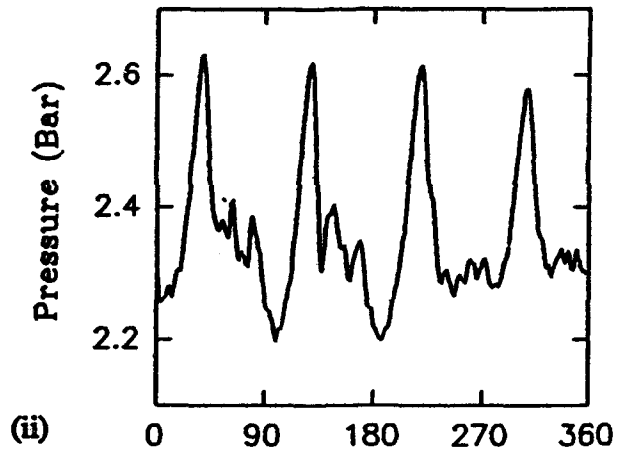
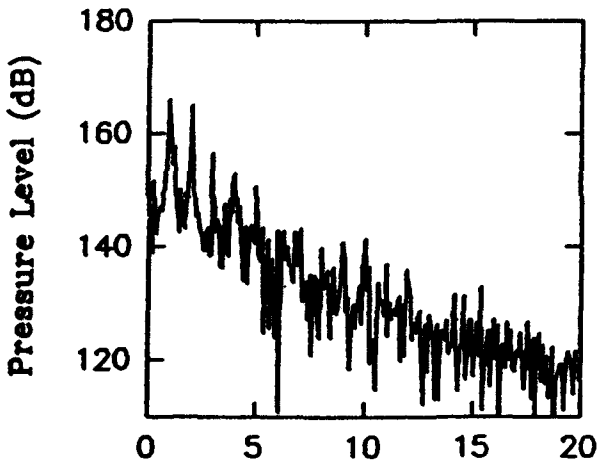
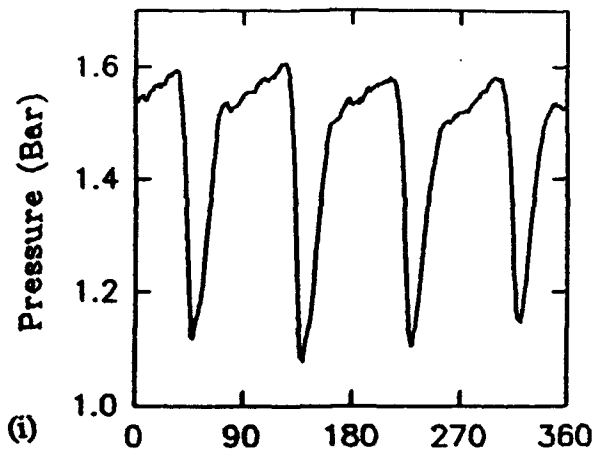
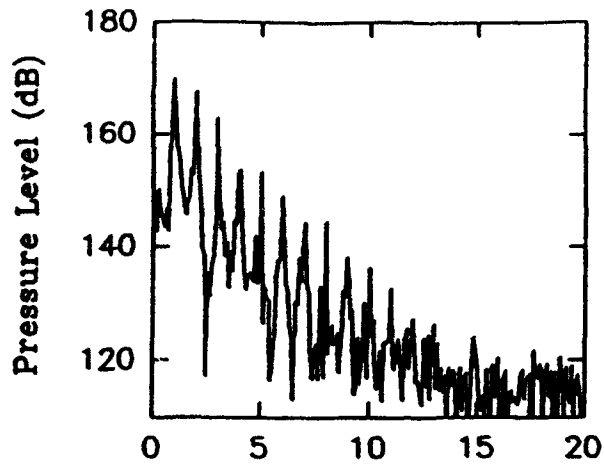


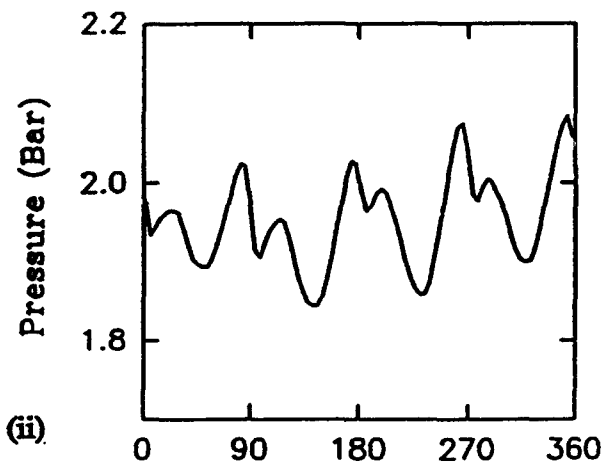
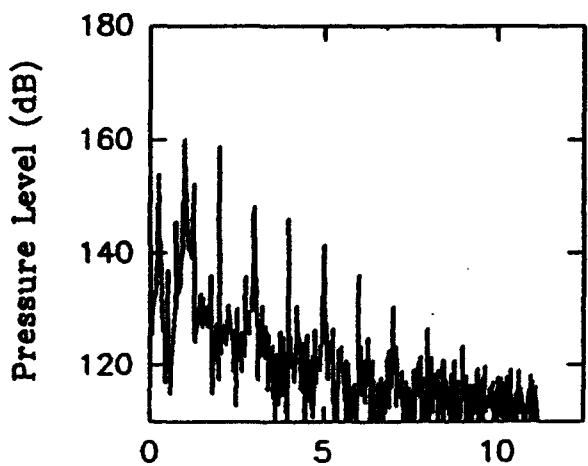
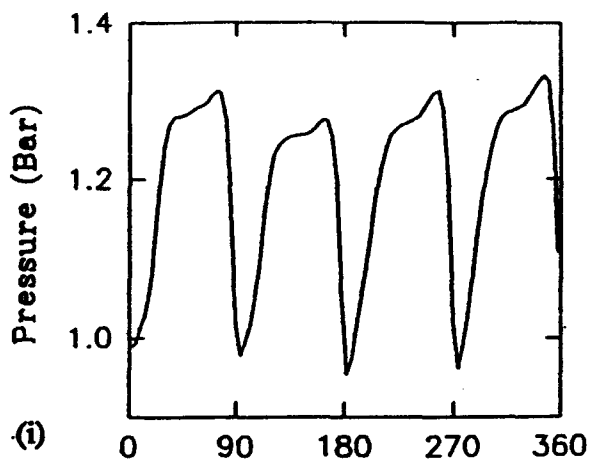
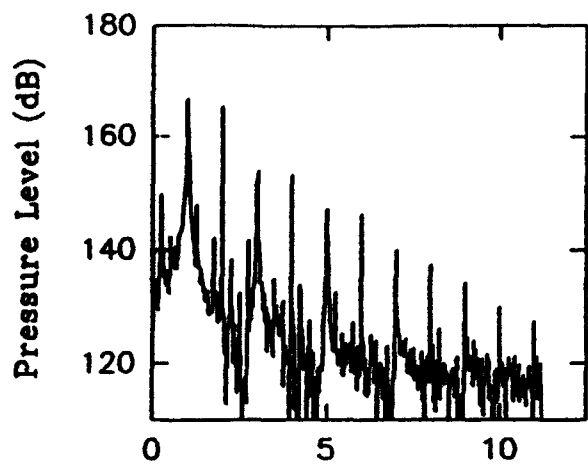
Figure 3. Head coefficient of the pump running at 2910 rpm.
 (○ perspex casting; ● metal casting; — manufacturer's specification).



Normalized Frequency

Shaft Angle (Degree)

Figure 4a. Pressure distribution and frequency spectra obtain at $\psi = 0$ with a sampling frequency of 21.6 kHz
 (i) $0.93 Q_n$ (ii) $0.15 Q_n$.



Normalized Frequency

Shaft Angle (Degree)

Figure 4b. Pressure distribution and frequency spectra obtain at $\psi = 110$ with a sampling frequency of 5.4 kHz.
 (i) 0.93 Q_n (ii) 0.15 Q_n .

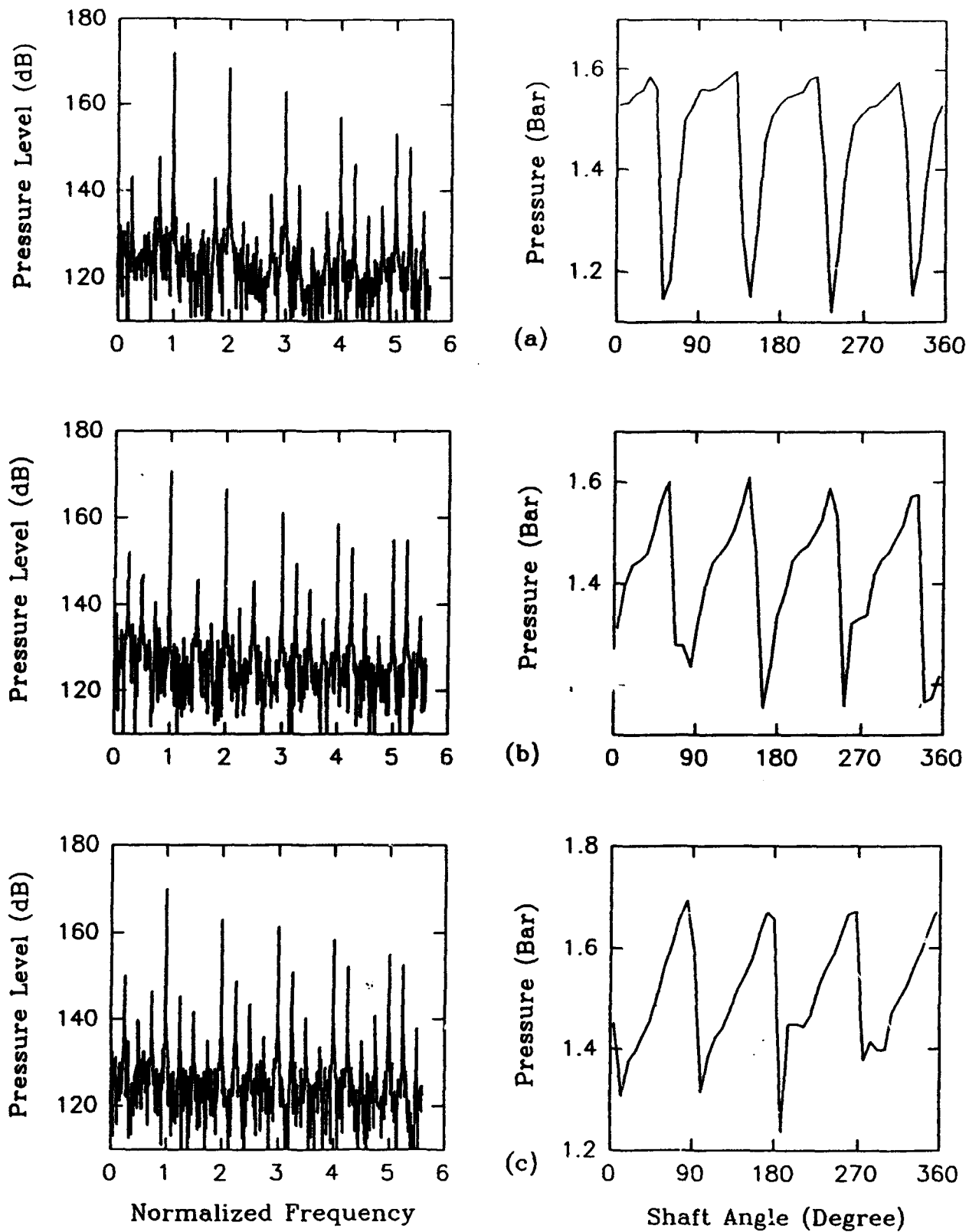


Figure 5. Ensemble averaged static pressure distribution at $0.93 Q_n$.
 (a) $\psi = 0$ (b) $\psi = 20$ (c) $\psi = 40$ (d) $\psi = 110$ (e) $\psi = 150$
 (f) $\psi = 210$ (g) $\psi = 270$ (h) $\psi = 300$ (i) $\psi = 330$.

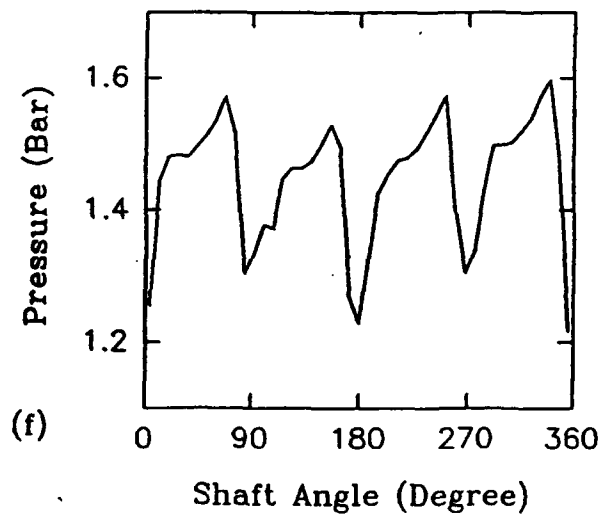
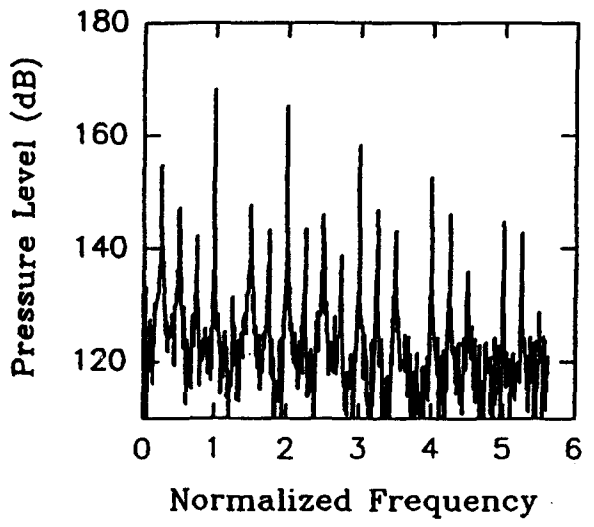
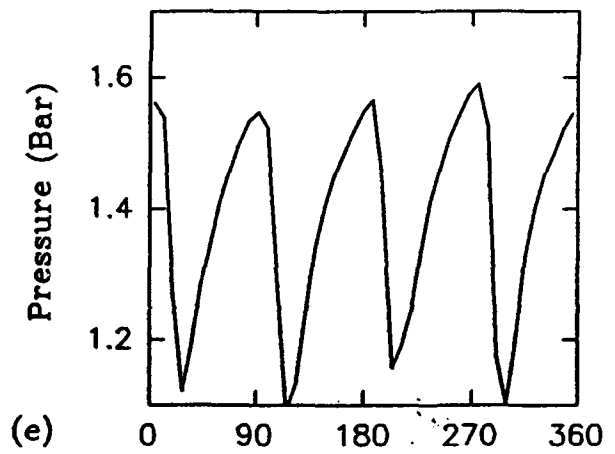
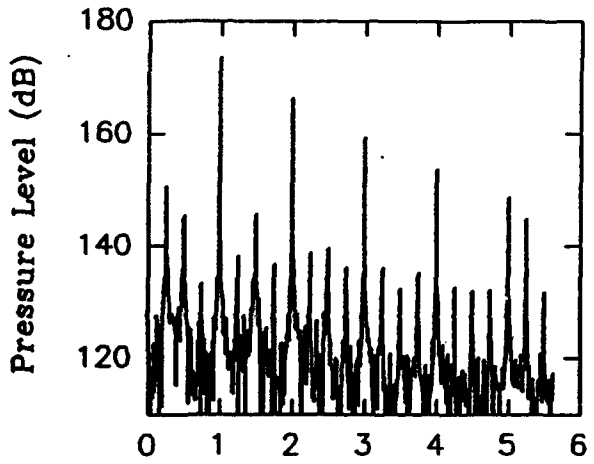
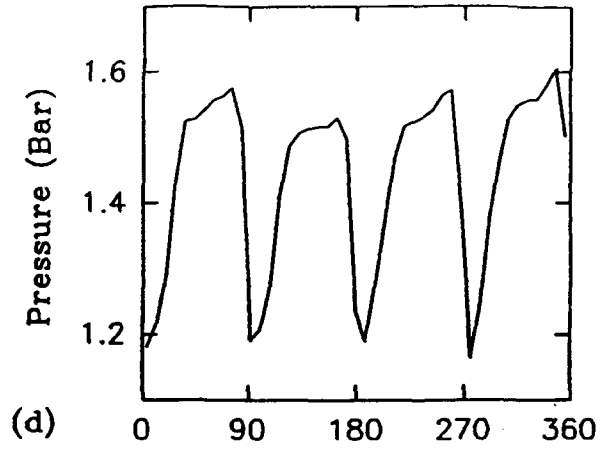
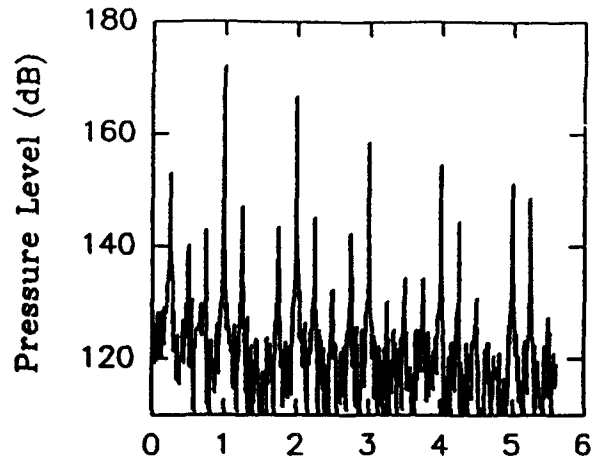


Figure 5. Continued

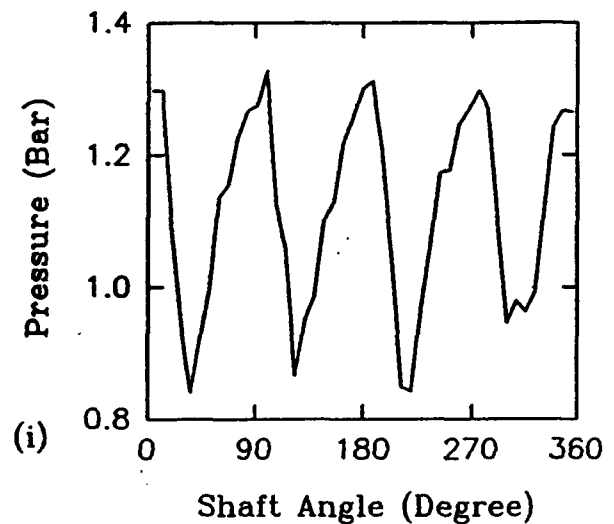
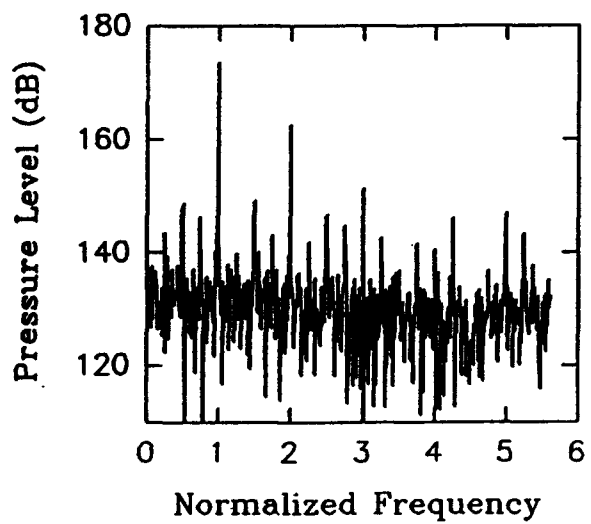
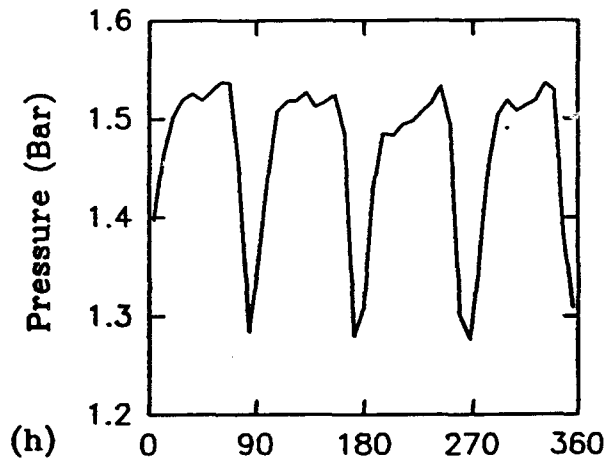
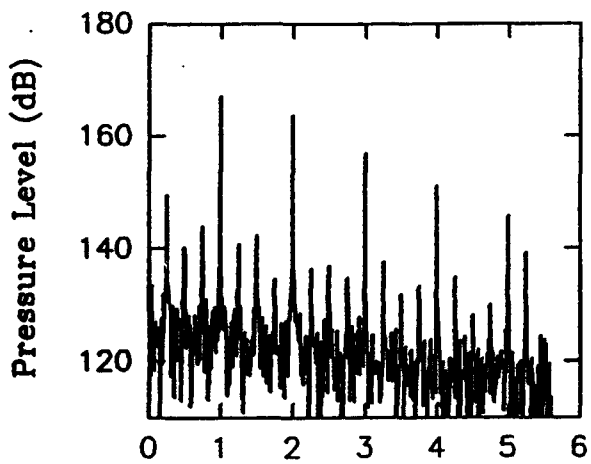
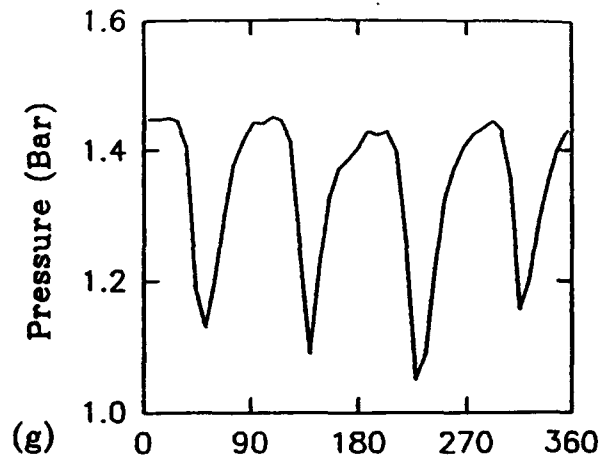
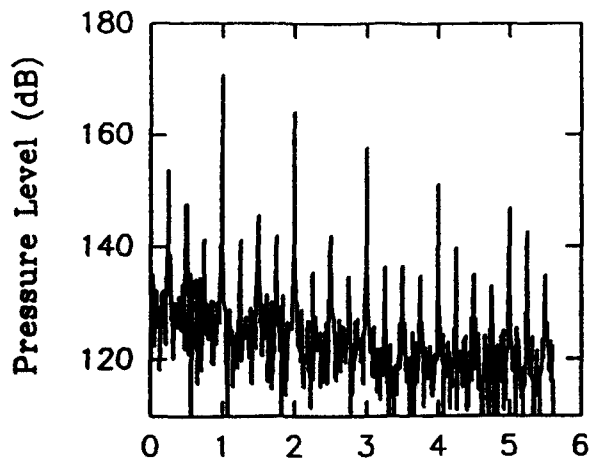


Figure 5. Continued

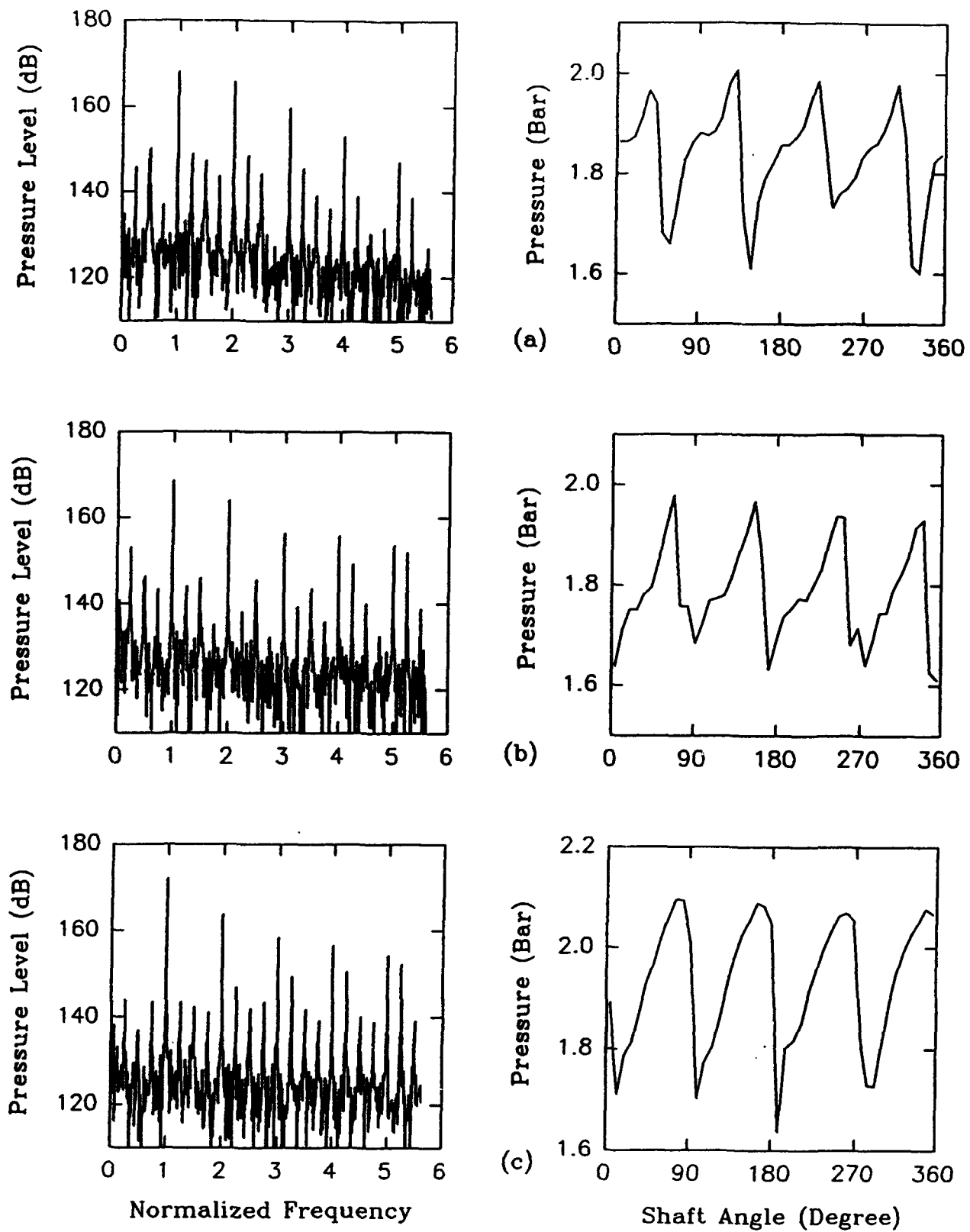


Figure 6. Ensemble averaged static pressure distribution at $0.57 Q_n$.
 (a) $\psi = 0$ (b) $\psi = 20$ (c) $\psi = 40$ (d) $\psi = 110$ (e) $\psi = 150$
 (f) $\psi = 210$ (g) $\psi = 270$ (h) $\psi = 300$ (i) $\psi = 330$.

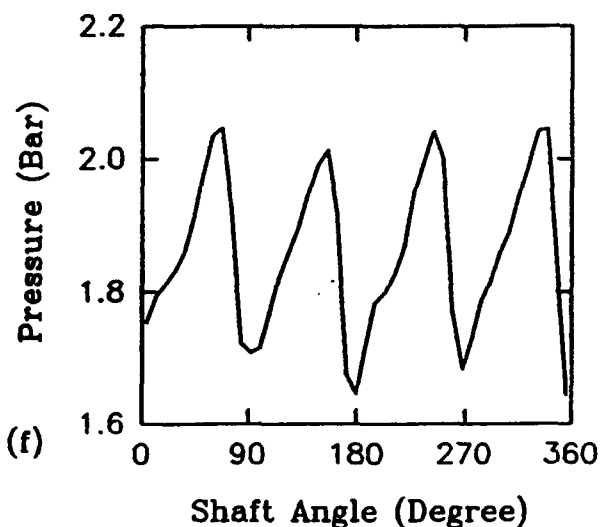
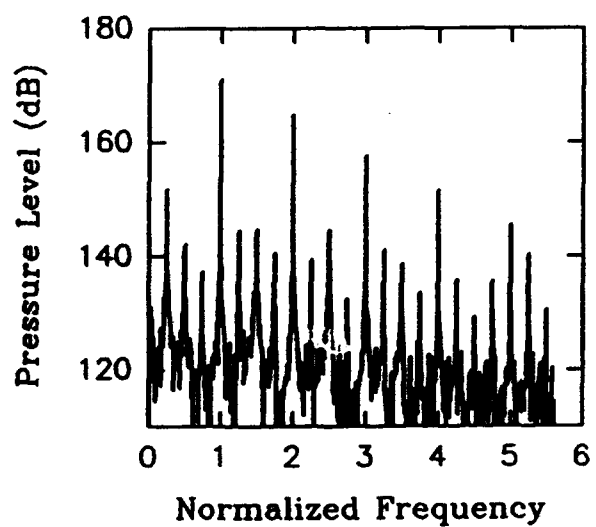
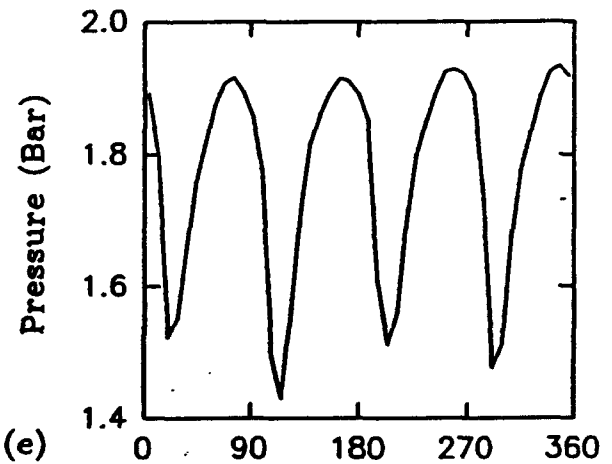
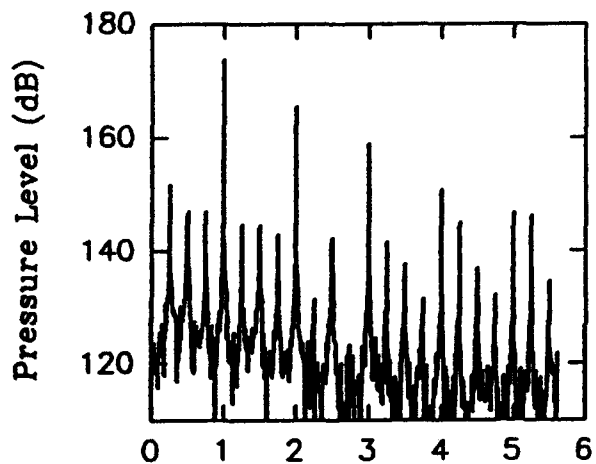
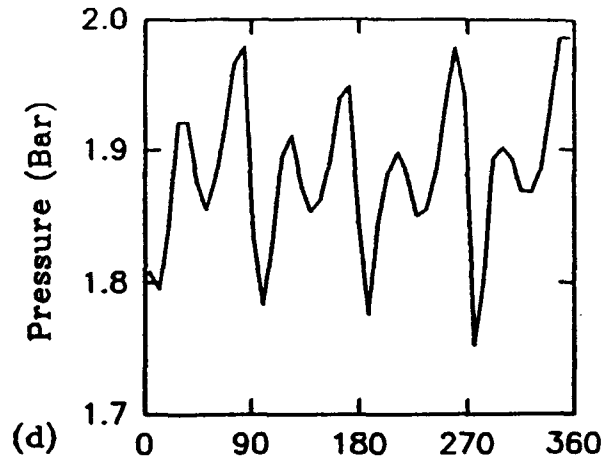
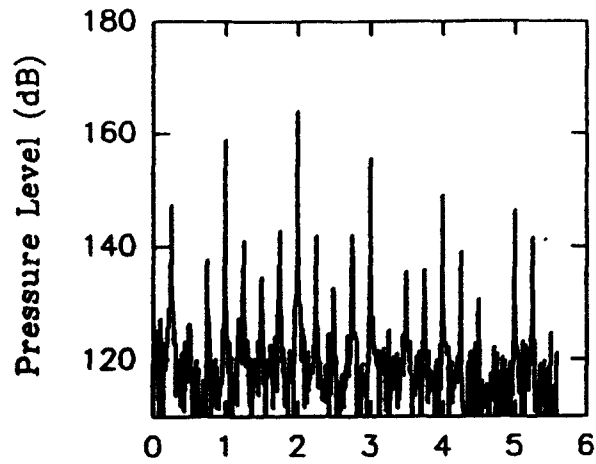


Figure 6. Continued

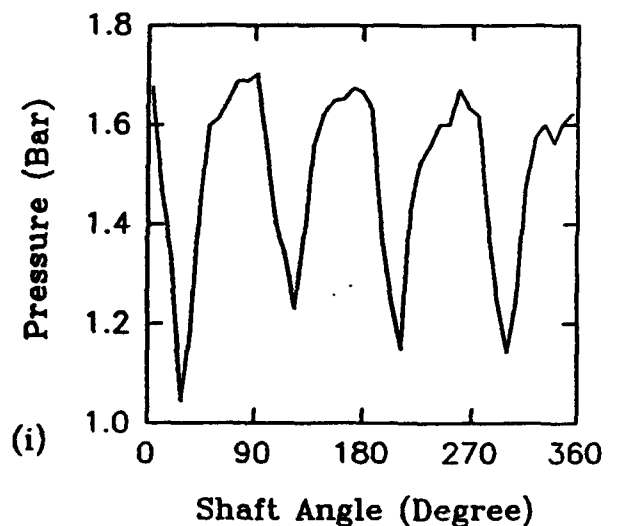
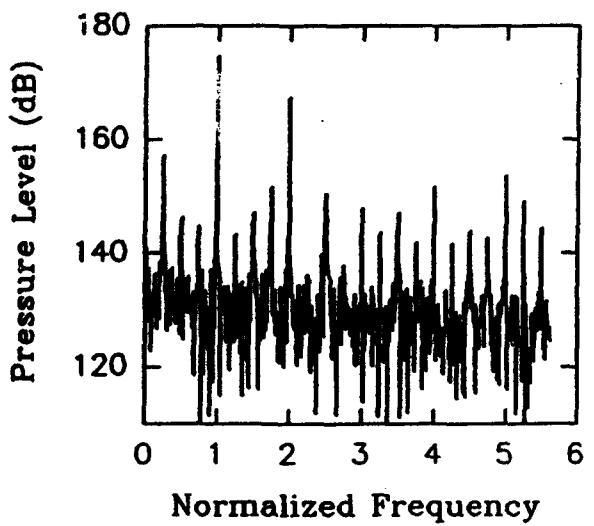
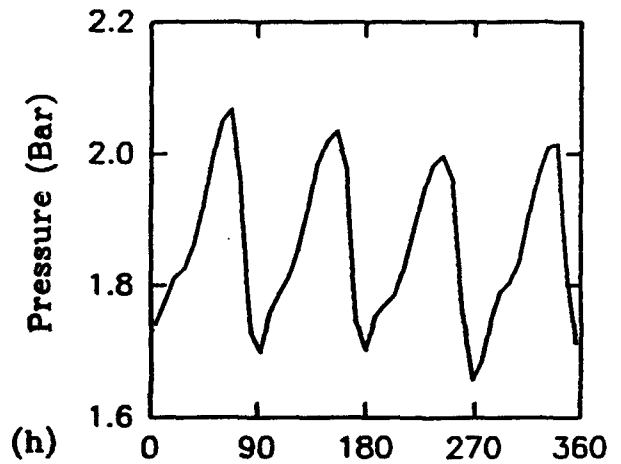
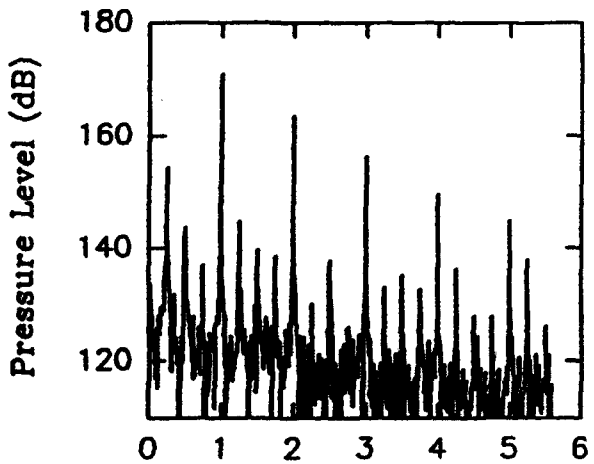
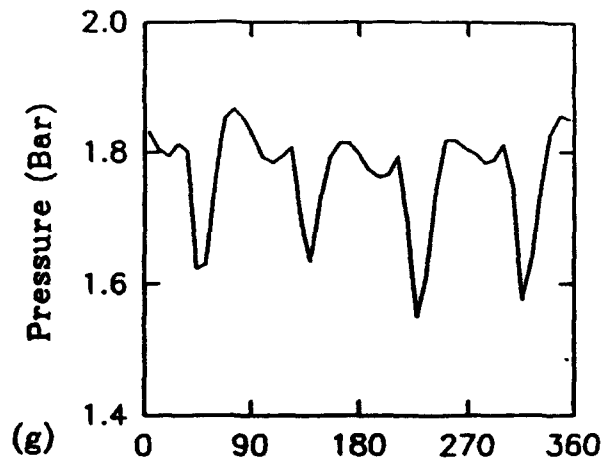
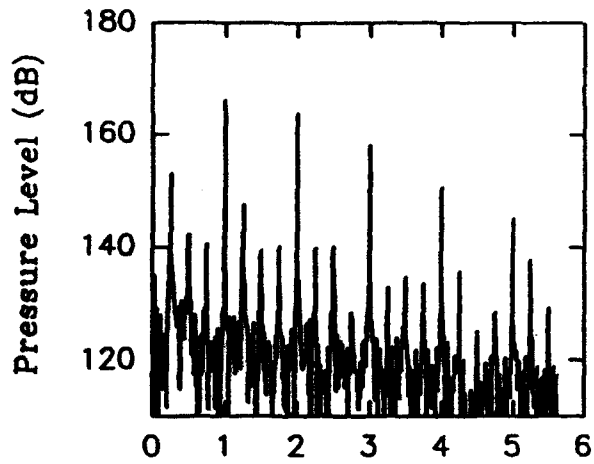


Figure 6. Continued

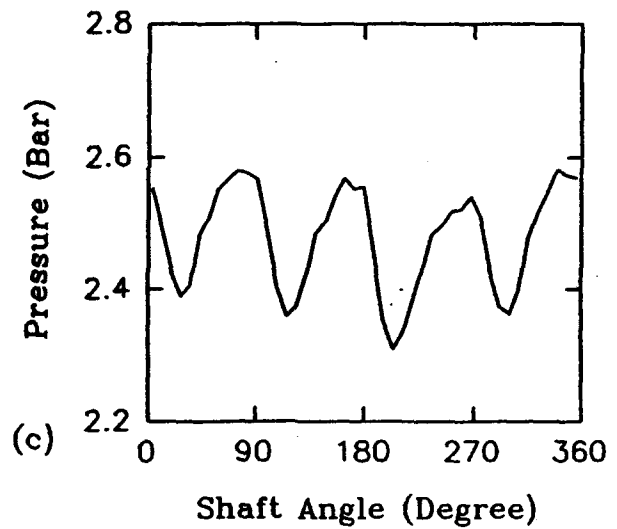
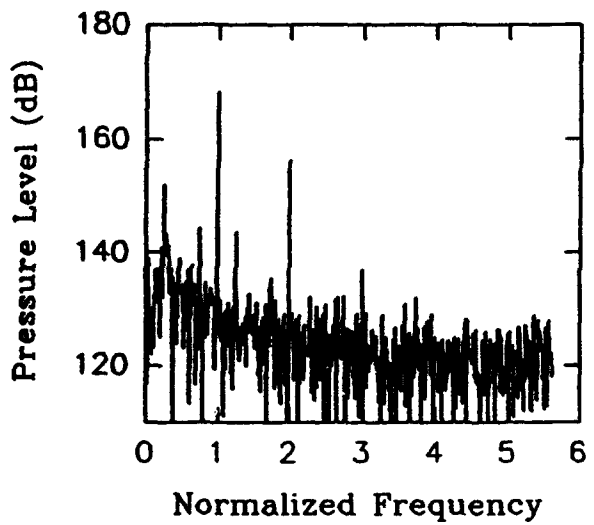
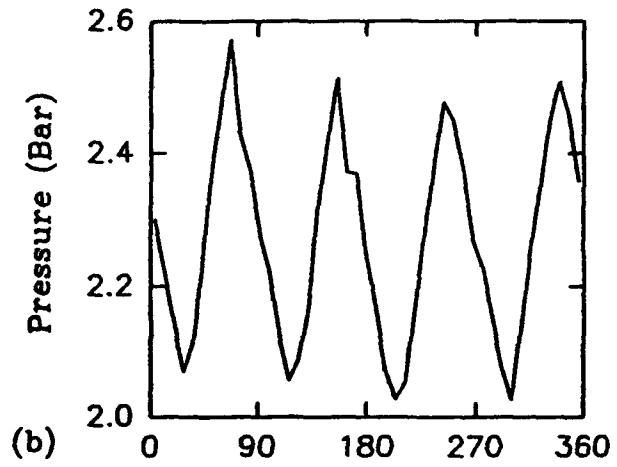
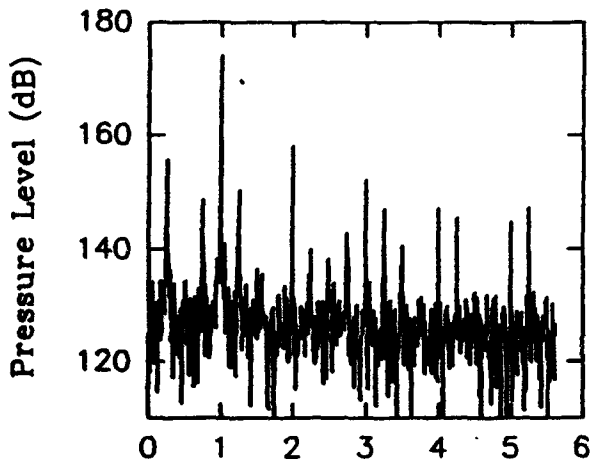
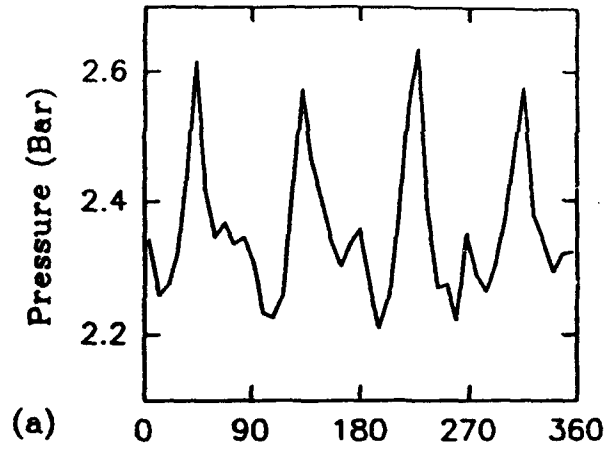
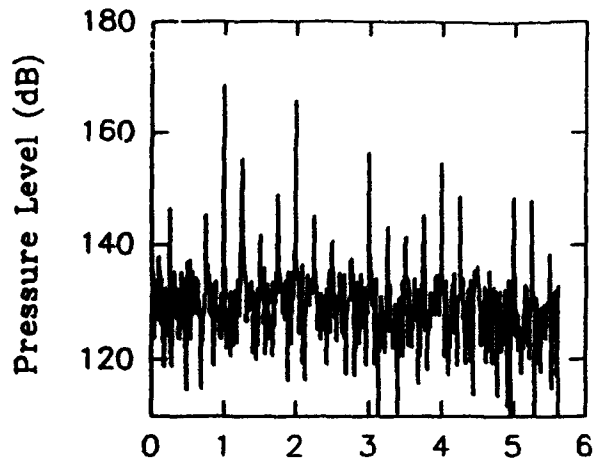
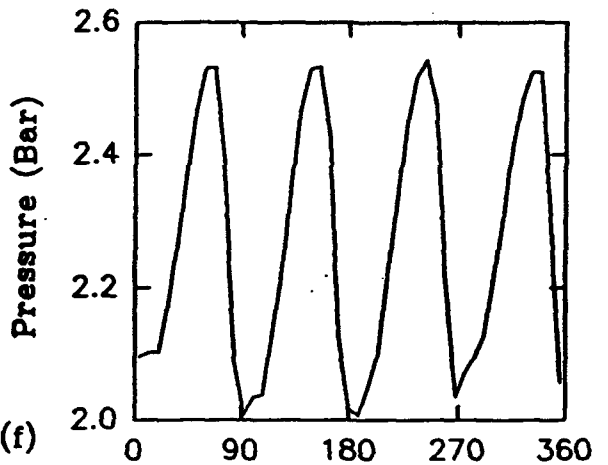
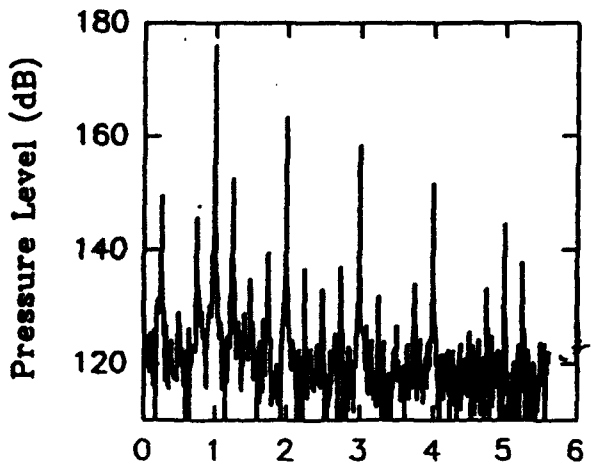
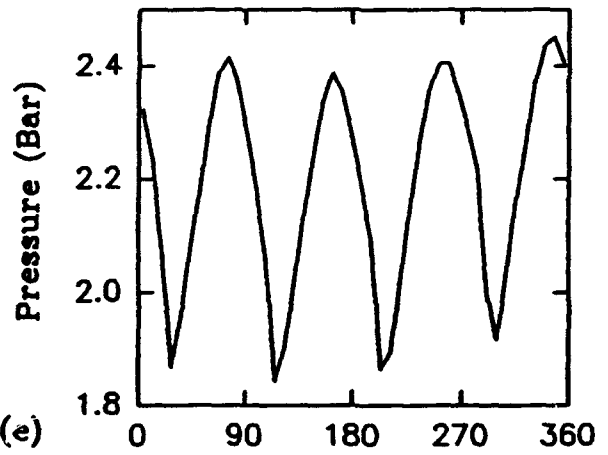
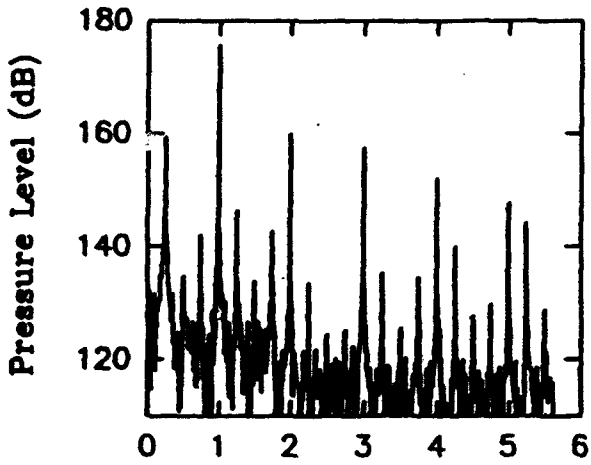
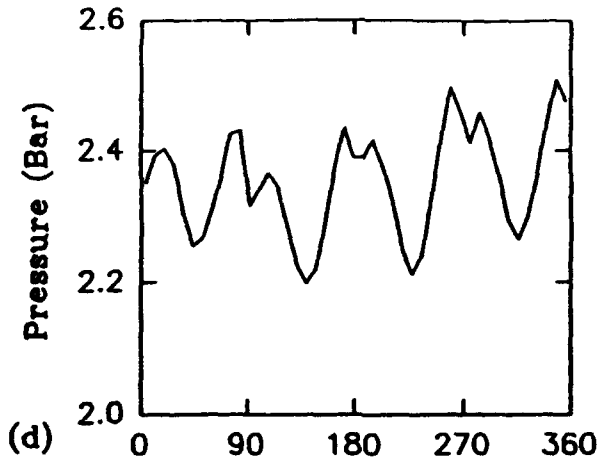
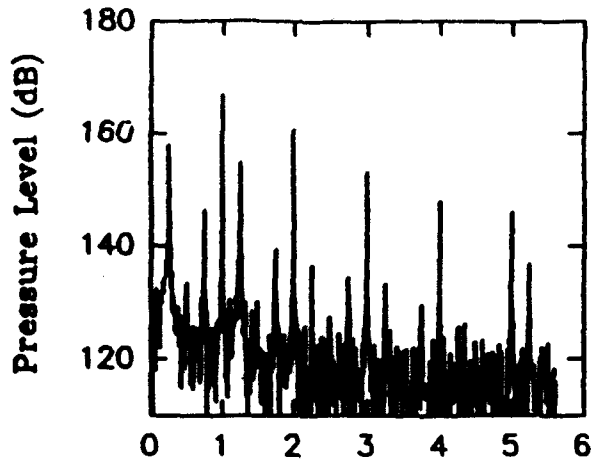


Figure 7. Ensemble averaged static pressure distribution at $0.57 Q_n$.
 (a) $\psi = 0$ (b) $\psi = 20$ (c) $\psi = 40$ (d) $\psi = 110$ (e) $\psi = 150$
 (f) $\psi = 210$ (g) $\psi = 270$ (h) $\psi = 300$ (i) $\psi = 330$.



Normalized Frequency

Shaft Angle (Degree)

Figure 7. Continued

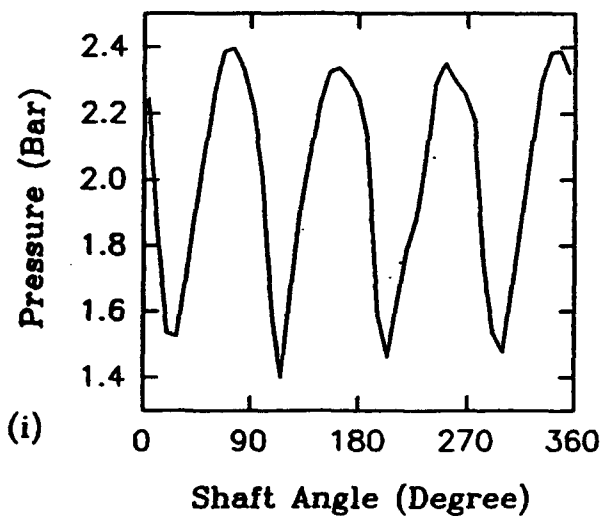
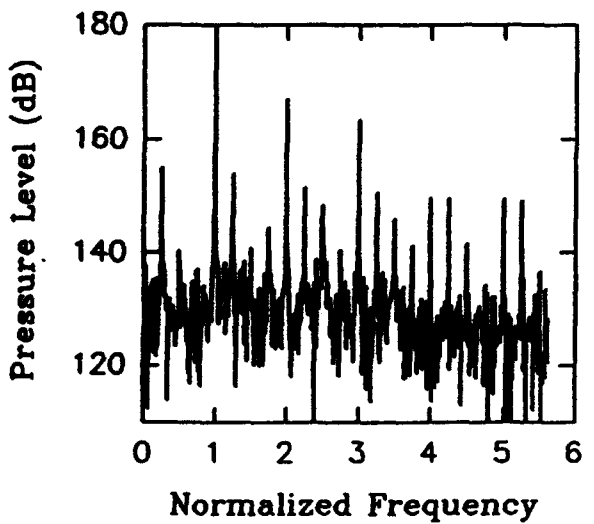
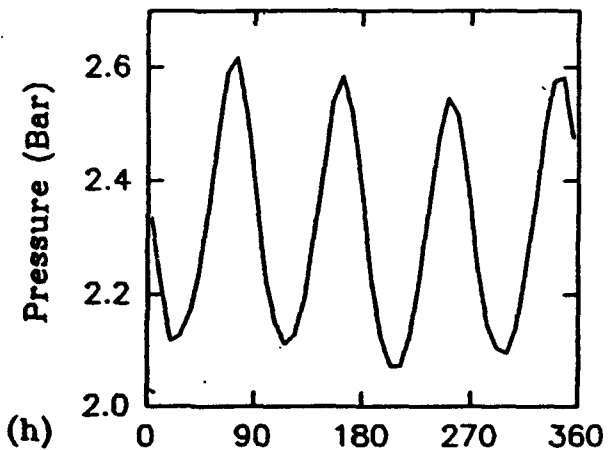
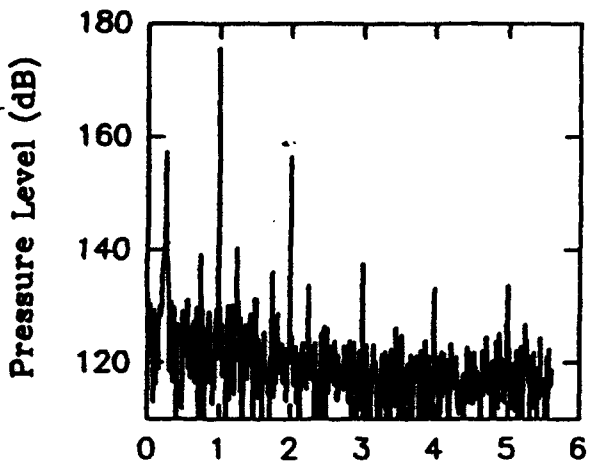
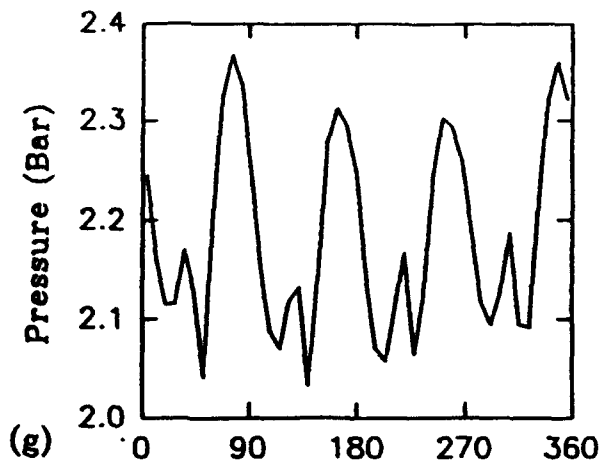
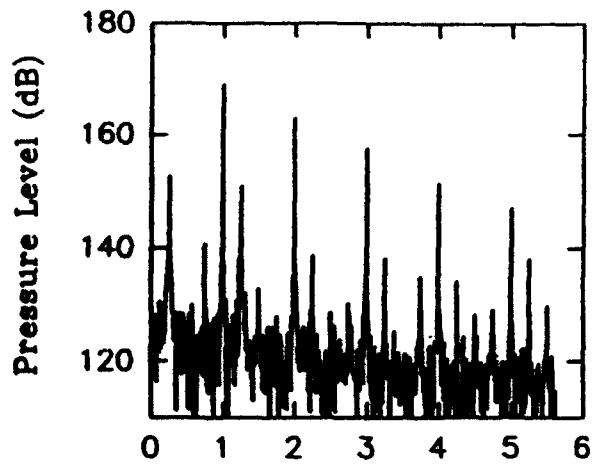


Figure 7. Continued

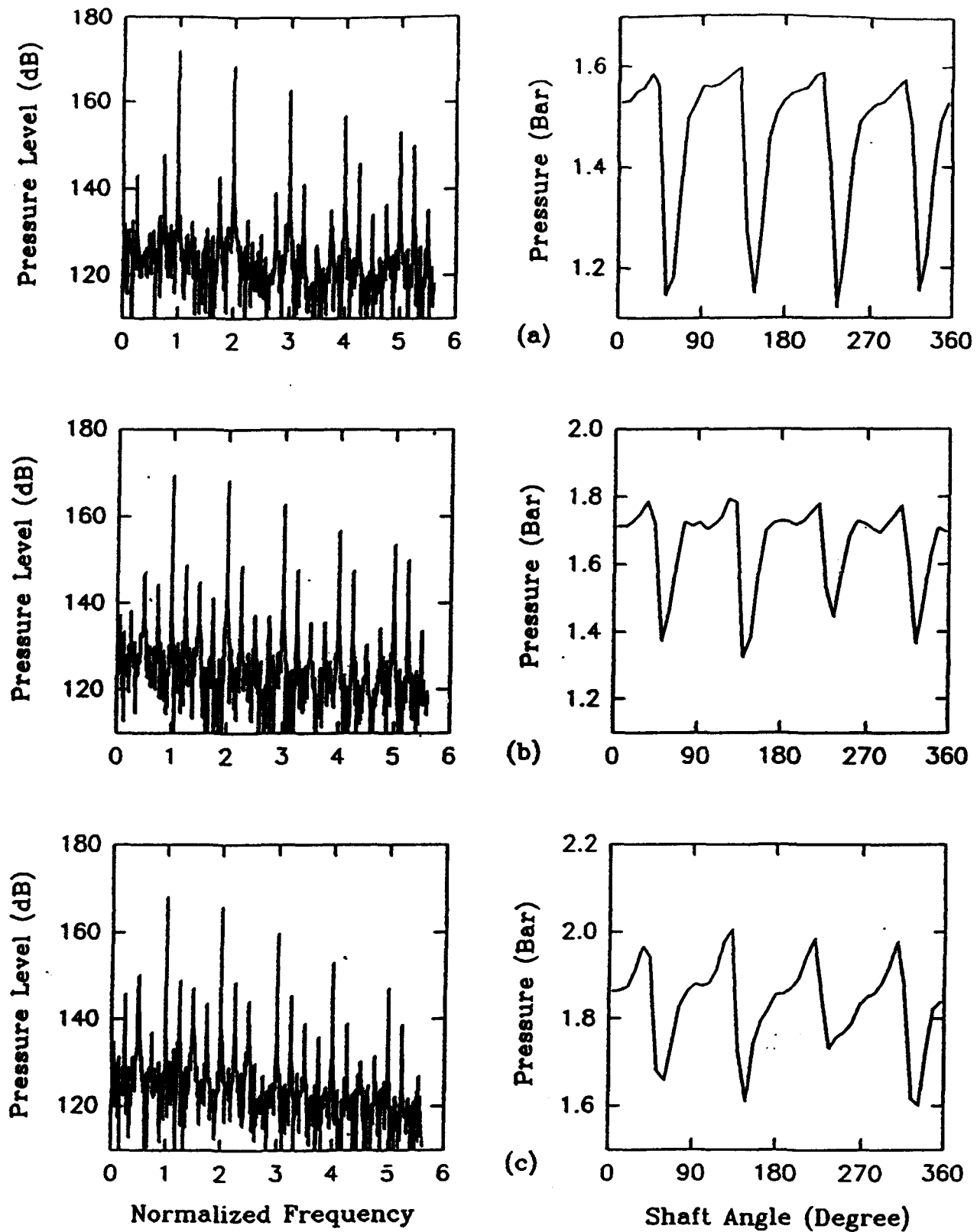


Figure 8. Ensemble averaged static pressure distribution at $\Psi=0$.
 (a) 0.93 Q_n (b) 0.77 Q_n (c) 0.57 Q_n
 (d) 0.49 Q_n (e) 0.29 Q_n (f) 0.15 Q_n

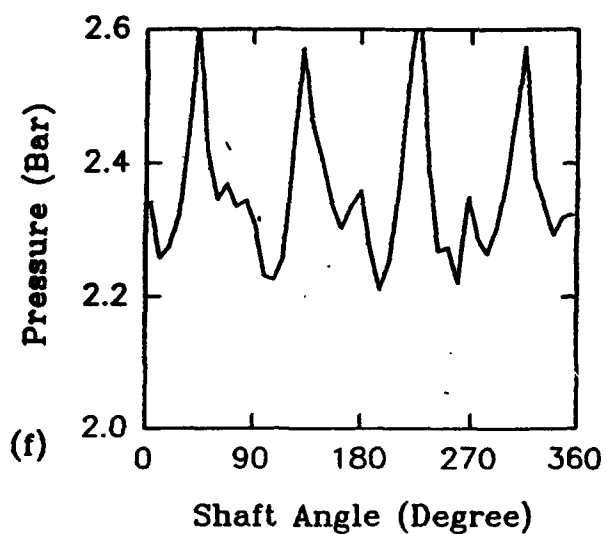
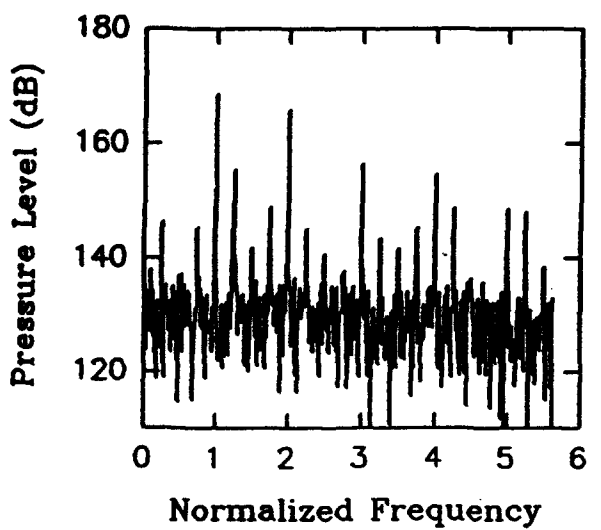
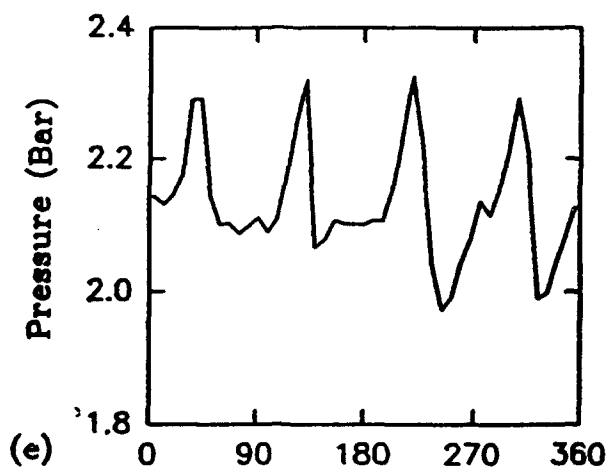
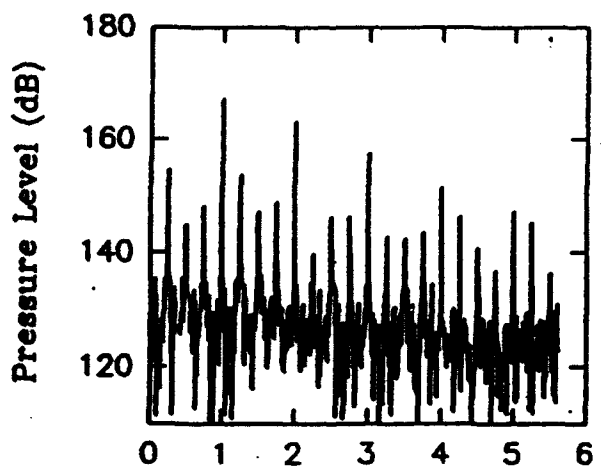
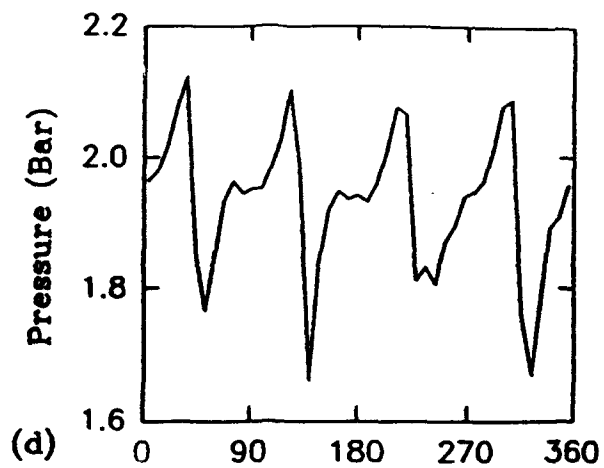
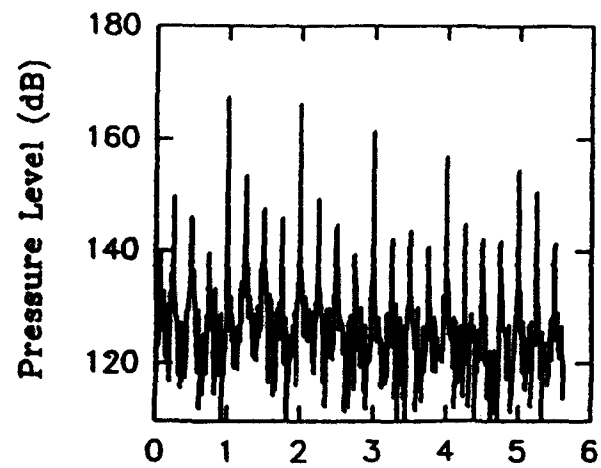


Figure 8. Continued

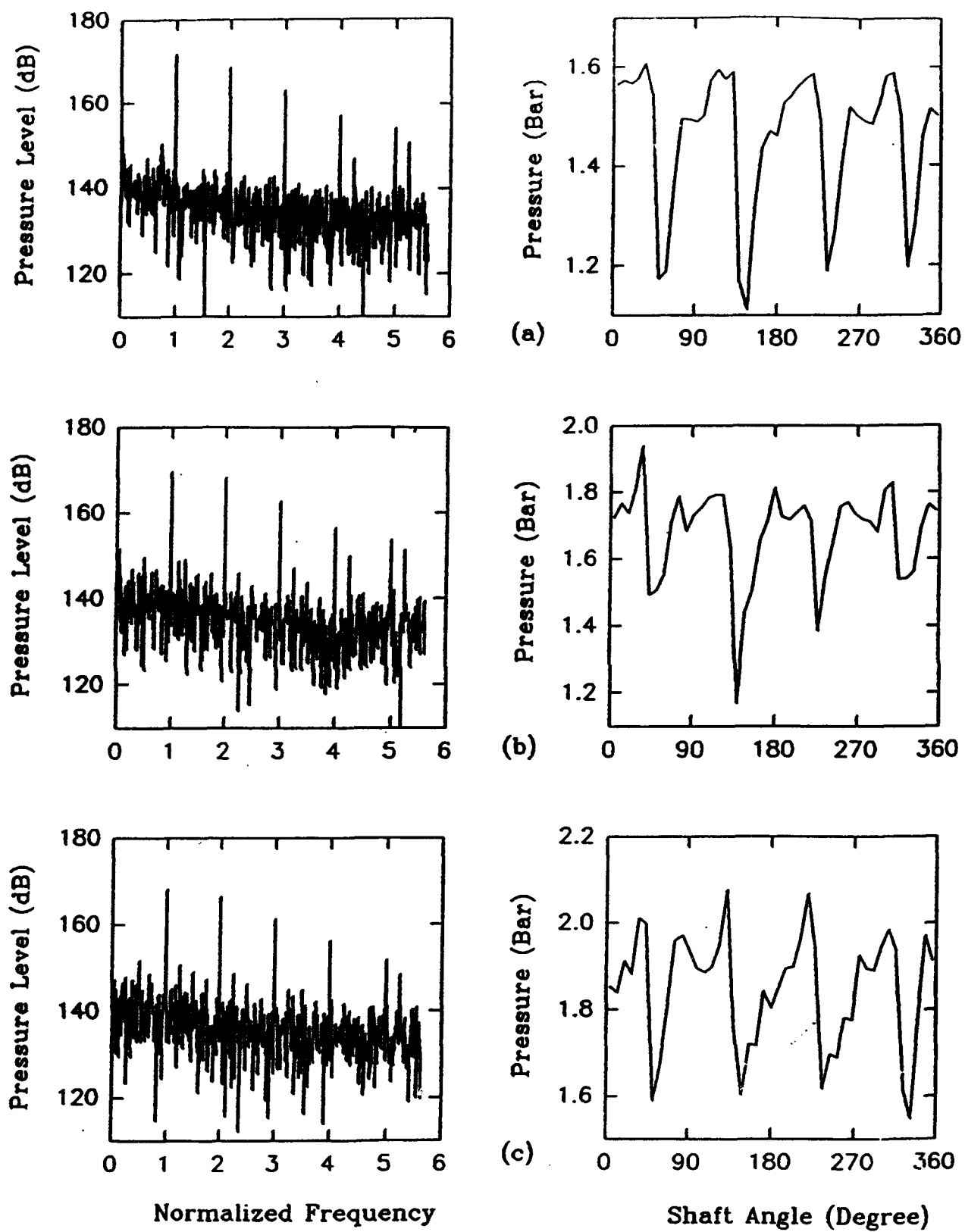
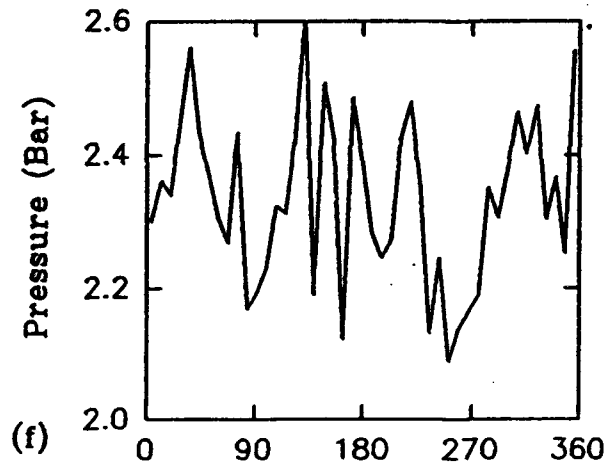
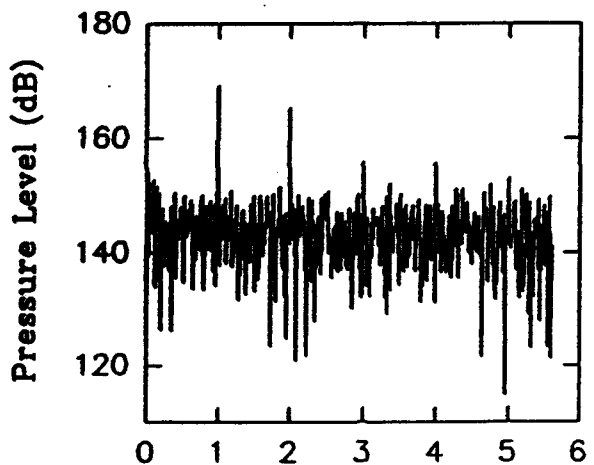
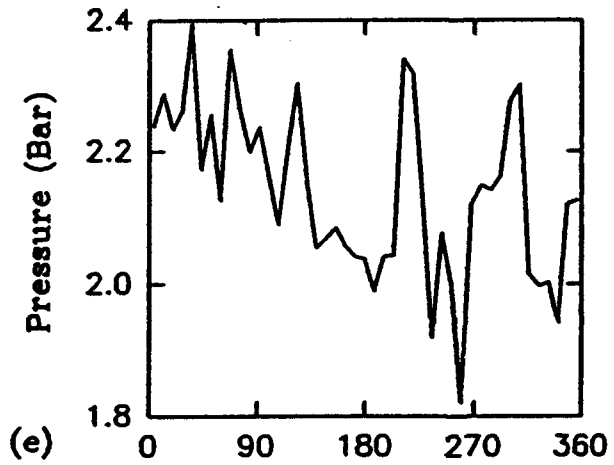
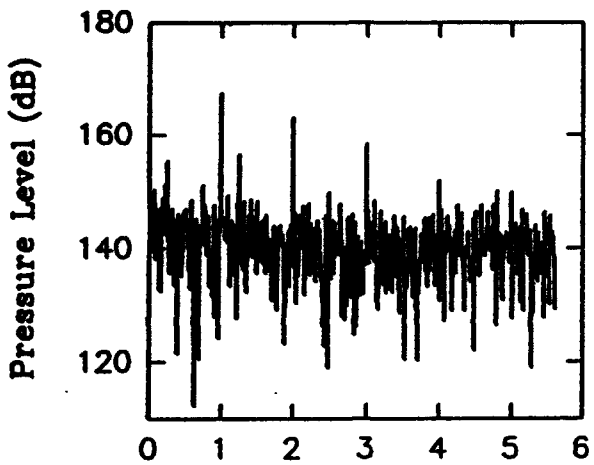
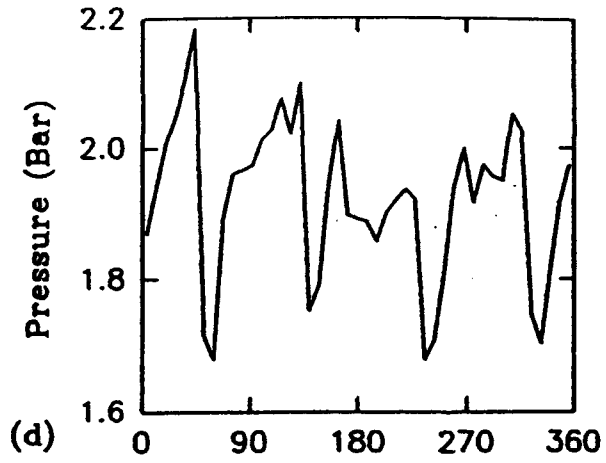
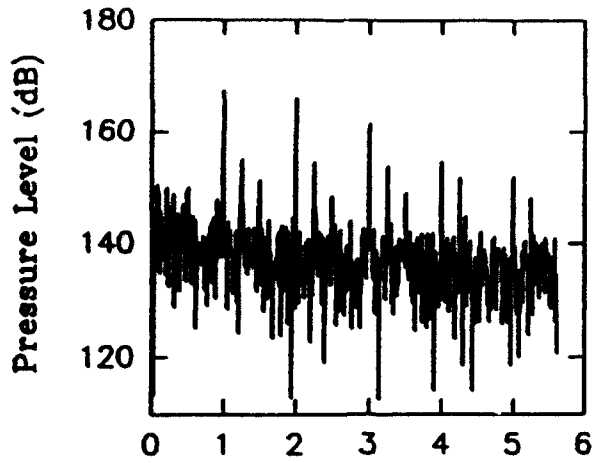


Figure 9. Instantaneous static pressure distribution at $\Psi = 0$.
 (a) 0.93 Qn (b) 0.77 Qn (c) 0.57 Qn
 (d) 0.49 Qn (e) 0.29 Qn (f) 0.15 Qn



Normalized Frequency

Shaft Angle (Degree)

Figure 9. Continued

APPENDIX

IMPERIAL COLLEGE OF SCIENCE, TECHNOLOGY AND MEDICINE

**Thermofluids Section,
Department of Mechanical Engineering,
Exhibition Road, London SW7 2BX, U.K.**

Flow Characteristics in a Centrifugal Pump

by

C.H. Liu, C. Vafidis and J.H. Whitelaw

November 1991

TF/91/31

Flow Characteristics in a Centrifugal Pump

C.H. Liu, C. Vafidis and J.H. Whitelaw

Department of Mechanical Engineering, Thermofluids Section,
Imperial College of Science, Technology and Medicine,
Exhibition Road, London SW7 2EX, U.K.

ABSTRACT

Measurements of turbulent flow in a centrifugal pump have been made by laser-Doppler velocimetry with flow rates between the design point and near shut-down. The pump comprised a radial flow impeller with four backswept blades and a single volute, and the working liquid had the same refractive index as the transparent casing. The velocity was quantified in terms of angle-resolved values with one degree resolution of shaft rotation and 360-degree averaged values in the impeller passages, the volute and the inlet and exit pipes, and the results are presented in absolute and relative frames.

The flows in the impeller passages were found to depart from blade curvatures at off-design conditions with increasing blade-to-blade variations of velocity and separation on the shroud surface and on the suction surfaces of the blades at low flow rates. The secondary flows in the passages were mainly from the suction to pressure surfaces, dominated by the influences of the relative motion between the shroud and impeller surfaces and the tip leakage flow, and are responsible for the non-uniform passage velocity distributions. The variations from one passage to another and with circumferential angle of the volute were quantified by angle-resolved velocities. The differences of 0.5 mm in dimensions and one degree in spacing of the four blades caused differences in passage velocity of up to 6% of the impeller tip velocity close to the design flow rate and up to 16% near shut-down. The discharge flow rate for the same passage varied up to 25% at three circumferential angles of the volute at a medium flow rate. The flow in the volute passage decelerated in the circumferential direction with greater velocity variations at the lower flow rates at which the cross-stream flow formed a vortex. The poor matching of the impeller and volute at off-design conditions caused swirl and separation in the inlet and exit pipes.

NOMENCLATURE

Roman letters

A	area
C_n	relative cross-stream mean velocity
C_s	relative streamwise mean velocity
D_e	exit pipe diameter (=28.5 mm)
D_i	inlet pipe diameter (=36 mm)
Ek	Ekman number ($= \frac{\mu}{4\rho R_t^2 \omega}$)
H	head
M	normalised angular momentum ($= \frac{r \bar{w}}{R_t^2 \omega}$)
n	number of blade
N	impeller rotation speed
N_s	specific speed ($= \frac{\sqrt{\Phi}}{\Gamma^{0.75}}$)
N_{sUS}	specific speed ($= \frac{N\sqrt{Q}}{H^{0.75}}$: Q: GPM; H: feet, N: rpm)
Q	flow rate
Q_n	design flow rate ($= 2.72 \times 10^{-3} \text{ m}^3/\text{s}$)
r, θ , z	cylindrical coordinates (see Figure 2)
Re	Reynolds number ($= \frac{U D}{\nu}$)
Ro	Rossby number ($= \frac{W_t}{2R_t \omega}$)
R_t	impeller outer diameter (= 62.7 mm)
S	slip factor ($= \frac{\bar{w}}{r\omega - v \tan \beta}$)
t	impeller blade thickness (=2.5 mm)
U, V, W	absolute mean velocities (see Figure 2)
u', v', w'	absolute rms velocities (see Figure 2)
U_e	bulk mean velocity in exit pipe
U_i	bulk mean velocity in inlet pipe
V_R	theoretical radial velocity at R_t , ($= \frac{Q}{(2\pi R_t - n \frac{t}{\cos \beta}) (Z_t + \delta)}$)

\bar{v}	area averaged radial velocity. ($= \frac{1}{A} \int_A v \, da$)
W_R	theoretical absolute tangential velocity at R_t . ($= W_t - V_R \tan \beta$)
W_t	impeller peripheral velocity at R_t
\bar{w}	mass averaged tangential velocity. ($= \frac{\int v w \, da}{\int v \, da}$)
x, y, z	Cartesian coordinates (see Figure 2)
Z_b	passage width at impeller discharge (≈ 6.7 mm)
Z_t	impeller blade height at R_t ($= 6.2$ mm)

Greek letters

β	impeller blade angle at R_t ($= 58$ degrees)
δ	blade tip clearance
Φ	flow coefficient ($= \frac{Q}{2\pi R_t Z_t W_t}$)
\emptyset	impeller shaft angle
Γ	head coefficient ($= \frac{g H}{W_t^2}$)
μ	Stodola slip factor ($= 1 - \frac{\pi \cos \beta}{n}$)
ν	kinematic viscosity of the liquid
ρ	density of the liquid
Ω	relative angular position on the impeller
σ	Busemann slip factor ($= \frac{A_1 - A_2 \frac{V_R}{W_t} \tan \beta}{1 - \frac{V_R}{W_t} \tan \beta}$)
ω	impeller angular velocity
Ψ	volute circumferential angle

1. INTRODUCTION

Centrifugal pumps are usually designed with fixed geometry and the performance is optimum at one operating condition, but a range of operating conditions may be required. The flows within rotors have attracted the interest of researchers for many years, but the complexities of rotating and stationary components and irregular geometries have implied measurement difficulties, so that investigations have been based largely on flow visualisation and wall pressure measurements (Acosta, 1954; Fischer and Thoma, 1954; Bowerman and Acosta, 1957; Senoo, Yamaguchi and Nishi, 1968; Lennemann and Howard 1970). Local velocities inside pump rotors have been reported, for example, by Binder and Knapp (1958), Howard and Lennemann (1971), Howard and Kittmer (1975) and Murakami, Kikuyama and Asakura (1980), but their results have not resolved the complex three-dimensional flow fields, and the accuracy and range of applicability has been limited by the intrusive nature of the probes. Efforts to resolve impeller flows have been paralleled by considerations of simpler rotating passages such as those of Fowler (1968), Johnston, Halleen and Lezius (1972), Moore (1973) and Rothe and Johnston (1976). A summary of the earlier works with pumps and rotating passages is provided in Table 1.

The development of laser velocimetry has allowed more detailed measurements within impeller passages and several investigations of the flows in pumps have been reported, for example those of Hamkins and Flack (1987), Flack, Hamkins and Brady (1987), Sideris and Van den Braembussche (1987), Miner, Beaudoin and Flack (1989) and Paone, Reithmuller and van den Braembussche (1989), and are paralleled by those considering centrifugal compressors, for example those of Eckhardt (1976, 1980), Adler and Levy (1979), Schodl (1980), Krain (1981, 1988), Khezzar, Vafidis and Whitelaw (1987) and Hah and Krain (1990). Recent reviews of the literature related to compressors have been provided by Cumsty (1989) and Whitefield and Baines (1990). The various investigations have considered non-uniform velocities, the importance of the secondary flows and

interactions between impeller and diffuser. However, the measurements have been confined mainly to locations accessible through the inlet or exit and to limited regions of the impeller passages, often with ensemble-averaged velocities based on small samples so that little turbulence information has been reported. Moreover, some experiments, particularly with pumps, have been made with simplified geometries to allow optical access. A summary of these investigations of pump flows which have used laser velocimetry is provided in Table 2. Recent advances in numerical modeling should also be noted, and Moore, Moore and Timmis (1984), Martelli and Michelassi (1990) and Vu and Shyy (1990), for example, have presented results of turbulent flows in stationary and rotating components of turbomachines.

The application of laser-based instrumentation to liquid-flow pumps is complicated, even with the casing manufactured from a transparent material, by the refractive-index differences between air, casing and liquid. To overcome this problem, the inlet and exit ducts, the present casing and volute were manufactured from acrylic with the same refractive index as the liquid. This technique has been used to allow measurements of the flows in inlet ports of internal combustion engines by Yianneskis, Cheung and Tindal (1988), the flow in a model of the space-shuttle main engine mixing chamber by Thompson, Senaldi, Vafidis, Whitelaw and McDonald (1989), the flow in the coolant passages of an engine cylinder head by Liu, Margary, Vafidis and Whitelaw (1990) and two-phase flows by Nouri, Whitelaw and Yianneskis (1987) and Liu, Nouri, Tse and Whitelaw (1989). Details of the method have been documented by Nouri, Whitelaw and Yianneskis (1988).

The present work provides details of the turbulent characteristics of the flow in a centrifugal pump, with focus on the unsteady effects related to the hydrodynamic generation of noise. According to Yuasa and Hineta (1979), the noise and vibration of pumps are closely related to the non-uniform velocity and pressure, especially near the cutwater, and the fluctuations are dominated by the fundamental and harmonics of the blade passing frequency. Preliminary experiments by Liu, Nouri,

Vafidis and Whitelaw (1990), obtained with a similar pump running with lower flow rate, showed that the combination of laser velocimetry, transparent casing and fluid of the same refractive-index allowed detailed measurements except where the inlet pipe masked the inner part of the impeller. Their results also revealed differences of more than an order of magnitude between 1- and 360-degree averaged velocities and that the influence of the impeller passage on the flow in the volute was present up to at least half of the volute diameter. Complementary measurements of wall pressure and far-field sound intensity have been reported by Tse, Sabnis, McDonald and Whitelaw (1991) with the same pump arrangement.

The following section describes the flow configuration, the instrumentation and possible sources of measurement uncertainty. The results are presented and discussed in the third section with separate consideration given to the inlet and exit flows, the absolute and relative flows in the impeller passages and the flow in the volute passage. The report ends with a summary of the more important conclusions.

2. FLOW CONFIGURATION AND INSTRUMENTATION

Figure 1 shows the experimental arrangement, including the pump, the circuit for the temperature-controlled liquid, the laser velocimeter and the encoder which identified the shaft angle and rotating speed of the impeller. The centrifugal pump (Price model SC100-150) was driven by an electric motor (Leroy Somer Motor, LS80L2) at a speed of 2910 rpm (N) and circulated liquid from and to a 70 litre tank through 36 mm (D_i) and 28.5 mm (D_e) inlet and outlet pipes respectively. The impeller, Figure 2, had four backswept blades of 2.5 mm thickness (t) with the blade height tapered from 11.2 mm at the 21 mm inner radius to 6.2 mm (Z_t) at the 62.7 mm (R_t) outer radius. The clearance between the impeller tip and shroud was adjusted to 0.5 mm, smaller than the manufacturer's nominal value, and the resulting passage width (Z_b) was 11.7 and 6.7 mm at the radii of 21 and 62.7 mm, respectively, where the

circumferential cross-section areas of the passage were 1427 and 2572 mm². The curve of the impeller blade was a logarithmic spiral with blade angle of around 30 degrees in the entrance section between radii of 12 and 20 mm, and 58 degrees (β) in the discharge section between radii of 40 and 62.3 mm, with a smooth transition from 30 to 58 degrees between radii of 20 and 40 mm.

The original cast stainless steel casing of the pump was replaced by a cast acrylic component of rectangular external shape and internal dimensions identical to those of the metal components. This was achieved by moulding a core of the metal casing in silicon rubber, creating a casting of plaster of Paris, moulding a core of low melting-point alloy (MCP 70) and a second casting, this time of acrylic. The final cast was machined to provide flat external surfaces and polished on its internal and external surfaces. The finished acrylic casing was annealed at 82°C for 35 hours with slow heating and cooling. The final internal dimensions were measured and found to be within 0.5 mm of those of the original casing and volute.

The working fluid was a mixture of 31.8% by volume of 1,2,3,4-tetrahydronaphthalene (tetraline) and oil of turpentine with density (ρ) and kinematic viscosity (ν) of 0.893 kg/m³ and 1.74x10⁻⁶ m²/s, respectively, at 25°C. The Reynolds number based on the impeller diameter (125.4 mm) and tip velocity (19.1 m/s) was 1.38x10⁶. The mixture was maintained at a temperature of 25±0.2°C by a temperature controller (Eurotherm, type 818), with a heater and cooler installed within the storage tank and a platinum resistance sensor near the pump outlet to maintain a refractive index of 1.49, identical to that of the cast acrylic. The flow rate of the mixture was regulated between 2.52x10⁻³ and 4x10⁻⁴ m³/s by a valve downstream of the pump outlet, which corresponded to a range of flow coefficients (ϕ) between 0.054 and 0.0086. The flow rate was measured by a sharp edge orifice meter, calibrated to an accuracy of better than 3%. The flow conditions of the experiment are provided in Table 3.

The motion in a rotating system involves a Coriolis force which is important when its magnitude is comparable with the other forces in the system, i.e. the inertial and viscous forces. The non-dimensional parameters of Ekman (Ek) and Rossby (Ro) numbers are defined based the ratio of viscous to Coriolis forces and inertial to Coriolis forces, respectively, and allow the estimation of the relative importance of the forces in the system. Typical values of the Ekman and Rossby numbers were calculated based on the impeller diameter and tip velocity as 3.4×10^{-7} and 0.5, respectively, and suggest similar magnitudes for the Coriolis and inertial forces and a smaller value for the viscous force, except in the boundary layer where the three can have similar values.

The design point of a pump with volute diffuser is determined from the criteria of equal angular momentum of the flow at the impeller discharge and at the throat of the volute (Karassik, Krutzsch, Fraser and Messina, 1976), usually corresponding to the condition of highest efficiency, and depends on the rotating speed. The flow rate at the design point of the pump running at 2910 rpm was $2.72 \times 10^{-3} \text{ m}^3/\text{s}$ (Q_n), based on theoretical velocities at impeller discharge plane and at throat of the volute, which is equivalent to a flow coefficient of 0.058. The experimental conditions comprised a range of flow rates from 93% to 15% of the design flow rate, Table 3. The performance of the pump is characterised by the head coefficients (Γ) of Figure 3 which shows that it is almost identical to that of the manufacturer's specification with the metal casing and is higher with the perspex casing by 18% near the design flow coefficient and by 15% near shut-down. The differences are due probably to the smaller impeller tip clearance ($\approx 0.5\text{mm}$) and the machined and polished inner surfaces of the perspex casing which reduced the leakage flow and friction.

The laser velocimeter, Figure 1, was similar to that of Liu *et al.* (1990) and comprised a one watt argon-ion laser tuned to the green line (514.5 nm wave-length) and operating at powers from 0.1 to 0.8 watt depending on the angle of light collection. The

transmission optical components were based on a diffraction grating which divided the beam and provided frequency shifts up to 13 MHz. The collection optical system comprised a lens of 33 mm aperture and 200 mm focal length with a 100 μm diameter pinhole and a photomultiplier (EMI model 9817B). Rotation of the transmission optical components allowed the measurement of two orthogonal components of velocity, and the third component was measured by realigning the velocimeter. The optical components were secured to an optical bench which was translated in three orthogonal directions with accuracy of location better than 0.1 mm in each direction. A summary of the optical characteristics of the velocimeter is provided in Table 4.

The Doppler signal, based on natural contaminants in the liquid and with a data arrival rate up to 3×10^4 per second, was processed by a frequency counter (TSI model 1990c) and interfaced to a microcomputer (IBM PC-AT), together with the pulse train from the optical shaft encoder with its resolution of 0.25 degrees. The digital information was collected in sequences of up to 1.4×10^6 velocity values and used subsequently to provide angle-resolved velocity traces of up to 2300 rotation cycles or ensemble averaged values based on angular windows of one degree. The ensemble averaged velocity statistics in each angular window were calculated from sample sizes between 1000 and 4000 velocity values depending on the magnitude of the rms of the fluctuations.

The zero of the impeller shaft angle (\emptyset) on each revolution was identified by a marker pulse from the shaft encoder which was purposely arranged to coincide with one of the impeller blade tips. The alignment was made by illuminating the outer rim of the blade tip at around the middle of its height by a focused laser beam aligned on the plane of the volute circumferential angle (Ψ) of 330 degrees, and the reflected light was collected by a photomultiplier. Every time a blade tip passed that plane, a pulse was generated with its width corresponding to that of the blade tip, and a total of four pulses were generated in one revolution. The marker pulse from the shaft encoder was then aligned with the centre of one of the blade pulses by

displaying them simultaneously on an oscilloscope. In this way, the marker of the shaft encoder was aligned with the centre of the blade thickness at the outer rim of the impeller, and the origin of shaft angle θ was aligned with the plane $\psi=330$ degrees.

The possible sources of uncertainty associated with laser velocimeters have been considered in many contributions, and only velocity gradient and statistical broadening were important here. Spatial gradients were greatest in the vicinity of the pressure and suction surfaces of the blades and the maximum uncertainties, minimised by the small effective length of the measurement volume (Table 4), were less than 0.5% in the estimates of the rms velocities; the corresponding angle-broadening errors were less than 1%. Statistical uncertainties were maintained unimportant by ensuring a sufficient number of velocity data in each ensemble average. Ensemble-averaged information over 360 degrees is presented at locations where the impeller influence is small. As a consequence of the above, the maximum uncertainties in the ensemble-averaged mean and rms velocities are not expected to exceed 2% and 5% of the local values respectively and should be less in the large majority of cases. The use of refractive index matching minimised positioning errors to less than 0.2 mm.

3. RESULTS AND DISCUSSION

The coordinate systems of the experiment are identified in Figure 2 and were chosen to facilitate presentation of results in different parts of the pump and in absolute and rotating frames. The inlet and exit flows are described by the stationary Cartesian coordinates, x - y - z , located in the inlet and exit pipes respectively, and the absolute flows in the impeller and volute are described by the cylindrical coordinates, r - θ - z , located in the volute with an additional set of cylindrical coordinates, r - θ - z , for the relative flow within the impeller. The impeller shaft angle θ was measured in the counter-clockwise direction with its origin at $\psi=330$ degrees. The exit pipe was normal to the plane of $\psi=330$ degrees which was also the origin of the x -coordinate in

the exit pipe. The relative angular coordinate Ω on the impeller was measured in a direction from suction to pressure surface with its origin at the centre of the blade thickness. The velocity measurements were based on a stationary probe volume with the angle dependent velocity resolved according to the impeller shaft angle. The measuring stations of the flows in the impeller and volute are identified by the volute circumferential angle Ψ measured in the counter-clockwise direction from the cutwater which was on an angular plane 30 degrees to that of $\Psi=330$ degrees.

The velocity measurements are presented in five sub-sections. The first describes the flows in the inlet and exit pipes where the velocity was insensitive to the rotation of the impeller and the data were averaged over 360 degrees. The second and third are concerned with the absolute and relative flows in the impeller passages and the influence of the volute, and the velocity is quantified by angle-resolved measurements to one degree of shaft rotation. The fourth sub-section considers the flow in the volute passage, and the last quantifies the slip factor based on integrations of angle-resolved velocities. The velocity values are normalised by the blade tip velocity ($W_t=19.1$ m/s), except in the inlet and exit pipes where the bulk mean velocity in the exit pipe (U_e , in Table 3) is used.

3.1 Flows in the Inlet and Exit Pipes

Profiles of axial mean velocity in the inlet pipe, 25 mm upstream of the impeller hub ($z/D_1=0.7$) and on two orthogonal planes, are presented in Figure 4 and show symmetry along the z-diameter and asymmetry along the y-diameter, reflecting the asymmetric pressure distribution in the volute. Integration of the radial profiles resulted in mass flow rates within 1% and 4% of the values measured by the flow meter for $0.93Q_n$ and $0.57Q_n$, respectively, and with poorer agreement at lower flow rates due to increased asymmetry and flow separation. The boundary layer thickened with evident regions of flow reversal and swirl near the pipe wall and larger normalised cross-stream velocities at $0.29Q_n$ and $0.15Q_n$, in contrast to the more uniform flow at

0.93 Q_n and 0.57 Q_n . The induced tangential velocity (the z -profile of V) has a maximum close to the outer radius and vanishes toward the axis, due to mis-matching of the inlet blades and flow angles at small flow rates. The increased radial velocities (the y -profile of V) at small flow rates are associated with the less-uniform axial flow and separation, and due partly to the upstream influence of the expansion of the duct at a short distance downstream of the measuring station. The maximum negative axial velocities are U_e and $1.8U_e$ for 0.29 Q_n and 0.15 Q_n , respectively, and occur close to the upper wall with induced tangential velocities up to $2.5U_e$ and $5.2U_e$. The increasing non-uniformity of the inlet velocity profiles at low flow rates is likely to cause variation of impeller passage flow and this is quantified in the following sections.

The rms of the fluctuating velocities in the inlet pipe, Figure 5, are asymmetric at the lowest flow rate and associated with the mean velocity distributions. The turbulence is near-isotropic except close to the outer radius where the flow rotated and separated at the lower flow rates. The minimum rms values on the centre of the pipe are $0.05U_e$, $0.07U_e$, $0.12U_e$ and $0.27U_e$ for Q/Q_n of 0.93, 0.57, 0.29 and 0.15, respectively, and are equivalent to local turbulence intensities of 8%, 11%, 20% and 43% based on the inlet bulk mean velocities U_1 in Table 3. The maximum rms velocities coincide with large axial velocity gradients near the wall and flow reversal at small flow rates. The high turbulence intensities in the inlet pipe may be attributed to the straight inlet pipe of eight diameters in length connected to an upstream flexible hose.

The distributions of axial mean velocity in the diverging section of the exit pipe ($x=1.8D_e$), a short distance downstream of the cutwater, and in the straight section ($x=3.2D_e$), are presented in Figures 6 and 7, respectively, and show qualitative axial symmetry with a minimum in the central region at 0.93 Q_n . A region of streamwise flow separation occurred close to the wall ($z=-1$) in the diverging pipe at 0.57 Q_n , Figure 6, and changed position and increased with decrease in flow rate to increase the non-uniformity of the velocity profiles. The separated wake,

inferred by the orthogonal diametral profiles, occupies up to 5%, 20% and 35% of pipe diameter with negative velocity values up to $-0.15U_e$, $-0.88U_e$ and $-1.49U_e$ for Q/Q_n of 0.57, 0.29 and 0.15 respectively. The streamwise flow separation at lower flow rates was accompanied by increased cross-stream velocities and caused the location of the separated wake to vary in the downstream straight pipe, Figure 7. The mean flow did not depend on the periodicity of the impeller rotation, and the poor match of flow angles and volute geometry in the upstream passage at off-design flow rates caused separation in the exit pipe.

The rms of the fluctuating velocities of Figure 8 are related to the mean values of Figure 7 in the straight pipe and are near-isotropic with uniform distributions at higher flow rates and increasingly anisotropy and spatial variations at the lower flow rates. The exit flow was fully turbulent with typical rms values of $0.17U_e$, $0.2U_e$, $0.65U_e$ and U_e for Q/Q_n of 0.93, 0.57, 0.29 and 0.15, respectively, and corresponding to 3% to 4% of the impeller tip velocity.

3.2 Flows in the Impeller Passages

The impeller discharge flow is characterised in Figures 9 and 10 by the circumferential profiles of the three components of mean velocity in the absolute frame on the mid-plane of the impeller passage at discharge, with Figure 10 highlighting the effects of flow rate. The velocities in the four impeller passages, Figure 9, show that the blade-to-blade variations and the passage-to-passage differences of velocity increase with decrease of flow rate, with the maximum differences between passages occurring close to the blade surfaces. Inspection of the impeller geometry showed maximum differences of 0.5 mm in passage width (Z_b) and up to one degree in blade circumferential spacing, and these imperfections were responsible for the observed passage-to-passage variations of velocity. The maximum differences in the radial and tangential velocities between passages were $0.025W_t$ and $0.06W_t$, respectively, at the highest flow rate, and increased to $0.03W_t$ and $0.16W_t$ at the lowest flow rate. The blade-to-blade

variations of velocity in W , V and U components are up to $0.16W_t$, $0.14W_t$ and $0.09W_t$, respectively, at $0.93Q_n$ and increased to $0.25W_t$, $0.32W_t$ and $0.12W_t$ at $0.15Q_n$.

The variations of discharge velocity with flow rate are more clearly illustrated in Figure 10 which considers one impeller passage, as in the remainder of this paper. It should be noted that the velocity values belong to an absolute frame so that the tangential velocity is much larger than the other two components and the normalised value will be unity at the blade surfaces, i.e. at $\Omega=2$ and 88 degrees. The results show uniform tangential and axial components of velocity, except close to the surfaces of the blades, with the radial component increasing from suction (SS) to pressure (PS) surfaces at the flow rate of $0.93Q_n$. Decrease of flow rate caused the decrease of radial velocity and increase of velocity gradient between blade surfaces leading to radial flow reversal near the suction surface at $0.15Q_n$. The tangential velocity in the absolute frame also decreased with the radial velocity in accord with the increased slip effect, and a more detailed discussion is provided in sub-section 3.5. The axial velocity component has increased values with changes of sign at small flow rates suggesting increasing complexity of the secondary flow as discussed in detail in the later text.

It is obvious that these complexities and large blade-to-blade variations of velocity limit the value of investigations by methods without angle-resolving ability and, as has been pointed out by Liu *et al.* (1990), the ensemble-averages over 360 degrees can lead to over- or under-estimation of the local velocity by more than 100%. Figure 10 shows that the rms velocities are near-uniform and near-isotropic at high flow rates, and that the decrease of flow rate caused the increase of rms values and the blade-to-blade variations, with peak values close to the suction surface and in the wake region, as reported by Moore (1973) in a rotating diffuser, Flack *et al.* (1987) in a centrifugal pump and Kjork and Lofdahl (1989) in a centrifugal fan.

A clear picture of the impeller flow is given by Figure 11 in terms of mean velocity vectors in the absolute frame at $0.93Q_n$

and by Figure 12 in the relative frame at the flow rates from $0.93Q_n$ to $0.15Q_n$. The results were obtained by measurements at six radial and three axial locations on the plane of $\Psi=330$ degrees and correspond to combinations of angle-resolved radial and tangential velocities at each point. The absolute flow of Figure 11 shows that the velocity increases radially, as a consequence of the work done by the impeller, with the outward angle higher at the pressure surface and lower at the suction surface. The outward angles of the vectors are small and approach zero close to the shroud, suggesting a tendency towards radial flow reversal.

It should be noted that the flow fields of Figures 11 and 12 was constructed from Eulerian measurements at stationary points on the plane of $\Psi=330$ degrees and corresponded to the behaviour of the flow passing the probe volume. However, the results are presented as the mean flow behaviour centred around the measuring point (± 45 degrees in the present case), as illustrated in the figure, which is justified provided the relative flow is invariant with rotation. Since the geometry of the volute is asymmetric with pressure distributions a function of the circumferential angles, the relative flow in the impeller passages may be subject to upstream effects due to the pressure field. The extent of variation of relative flow with the volute circumferential angle was examined by the measurements on the planes of $\Psi=60$ and 240 degrees, and the results are presented in sub-section 3.3.

The relative flow on the mid-plane of the passage in Figure 12 generally follows the curvature of the blade at the flow rate closest to the design point ($0.93Q_n$) with departures from blade curvature at inner radii close to the hub and a less regular flow close to the shroud. The reduction of flow rate decreased the velocity vectors and increased the flow angle (the angle between radius and relative velocity vector), and the flow tended to decelerate towards the suction side of the passage and accelerate towards the pressure side, Figure 12, $0.57Q_n$, $0.29Q_n$ and $0.15Q_n$. The obedience of the mean flow to the blade curvature is suggested by the mean flow angles in Figure 13 and 14. The flow

angles of Figure 13 on the mid-plane at $0.93Q_n$ increased along the radius with values smaller than the blade angle (58 degrees) at inner radii and larger than the blade angle at discharge. The flow angles remained close to the blade angle near the pressure surface where the streamlines followed the blade curvature. The flow angles at discharge were larger than the blade angle at all flow rates, Figure 14, and decreased almost linearly from suction to pressure surfaces and increased monotonically with the decrease of flow rate, leading to values larger than 90 degrees at the smallest flow rate where the radial flow was reversed.

Figure 12 also shows a tendency for the velocity vectors to change direction and to form vortices, more evident at small radii and close to the shroud, as the flow rate decreased. The velocity vectors at $r/R_t=0.71$ had a tendency to diminish on the pressure side of the passage at lower flow rates, $0.29Q_n$ and $0.15Q_n$, in contrast to the larger vectors on the suction side of the passage, suggesting an eddy within the blade passage. Measurements at smaller radii close to the concave surfaces of the blades were limited by the obstruction of the inlet pipe and the backward curved blades, combined with the near 90 degrees angle of light collection optimised to eliminate reflection from the impeller surface. Measurements were obtained over the outer 35% of the impeller radius and all the way along the periphery of the passage at discharge ($r/R_t=1$) and up to 63% at the inner radius of $0.65R_t$. The inward velocity vectors close to the shroud are common for an unshrouded impeller design, due to the radial pressure gradient and the relative motion of the shroud and impeller, which increased in magnitude and angle as the flow rate was decreased leading to radial flow reversal at radii up to $0.71R_t$ at the smallest flow rate. The increasing irregularity of the flow and separation at off-design conditions are related to the centrifugal and Coriolis acceleration, the irrotational nature of the flow and viscosity and are discussed in the following paragraphs.

The centrifugal and Coriolis forces are balanced by radial and blade-to-blade pressure gradients from inner to outer radii and from suction to pressure surfaces, respectively. The static

pressure is therefore lower on the suction surface and higher on the pressure surface. Since the pressure at discharge is dominated by that of volute, the pressure gradient along the suction surface is stronger to give rapid deceleration of the flow. The pressure gradient from one surface to another gives rise to secondary flows in which the boundary layer fluid is transported from pressure to suction surfaces along the walls of the hub and shroud, and the core fluid is convected in the opposite direction, leading to accumulation of low energy fluid on the suction side of the passage. The tendency for separation to occur on the suction side of the passage had also been reported by Dean and Senoo (1960) and Eckhardt (1976, 1980) with compressor rotors.

Fowler (1968), Moore (1973) and Rothe and Johnston (1976) had investigated flows in two-dimensional channels with converging and diverging angles, and Johnston, Halleen and Lezius (1972) considered a straight channel, rotating in a span-wise direction. They concluded that rotation enhanced the tendency towards stall which occurred on the suction surfaces of their ducts, and that the Coriolis acceleration stabilised the turbulent boundary layers on suction surface and destabilised them on pressure surface, resulting in local suppression of turbulent mixing in the suction-side boundary layer and consequent tendency for stall. However, the backward curvature of the blade causes streamline curvature and can generate forces opposite to that due to rotation and with similar magnitude to enhance the tendency of stall on the convex surface of the blade.

Potential flow in the impeller passages can be represented by superposition of a through-flow and a relative eddy, Stanitz (1952). The relative eddy is due to the irrotational nature of the flow and has the angular velocity of rotation but the opposite direction. In the present case, it rotated in a clockwise direction and was bounded by the blades surfaces consistent with acceleration and deceleration along the suction and pressure surfaces respectively, and acceleration from suction to pressure surfaces at large radii and the opposite at small radii. It caused the departure of streamlines from blade curvature, so that the

flow angles were larger than the blade angle at discharge and the impeller head output was less than the theoretical value.

The radial mean velocities of Figure 15 show the deceleration and acceleration along the suction and pressure surfaces respectively, and the reversed flow close to the shroud. The relative eddy is evident in the profiles at small radii where a clockwise-rotating vortex exists at $0.15Q_n$, in agreement with the trend predicted by Stanitz (1952) with potential theory where recirculation existed on the pressure surface. This vortex decreased in size and moved closer to the suction surface towards outer radii, due to the backward leaning geometry of the passage, and the radial flow on the pressure side of the passage was enhanced at discharge. Similar trends exist at higher flow rates, but the vortex is less obvious due to the stronger through-flow.

The streamwise and cross-stream velocities of Figures 16 and 17 were obtained by resolving the radial and tangential components. The streamwise component of Figure 16 increased uniformly with radius with smaller variations between hub and shroud and across the passage than the radial component. The variations with flow rate were also less for the streamwise velocity and this, together with the more uniform distributions, suggests that the non-uniform distributions in radial component were mainly caused by the secondary flows. Flow reversal in streamwise direction was observed at small radii, close to shroud, and in the pressure side of the passage at the smallest flow rate, and is related to the near-stagnation region of Figure 12.

Figure 17 shows that the cross-stream component of mean velocity had positive and negative values at $r/R_t=0.71$ and only negative values at discharge and increased from hub to shroud and from pressure to suction surfaces due to the relative motion of the impeller and the shroud, influenced by the curvature of the blade and the relative eddy. The velocity on the shroud surface, $z/Z_b=1$, is the cross-stream component of the tangential velocity relative to the impeller, i.e. $-0.38W_t$, $-0.48W_t$ and $-0.53W_t$ at

$r/R_t=0.71, 0.9$ and 1 respectively, with the arrow indicating the relative motion. Decrease of flow rate increased the secondary flow at $r/R_t=0.9$ and 1 , and the cross-stream velocities on the mid-plane at discharge, $z/Z_b=0.5$ and $r/R_t=1$, were up to $0.1W_t$, at $0.93Q_n$ and $0.35W_t$ at $0.15Q_n$ close to the suction surface. The magnitude of the cross-stream velocity at $r/R_t=0.71$ was more uniform with flow rate, but the changes of sign suggest the formation of vortices due to passage pressure gradients and leakage flow, and a counter-clockwise vortex is evident close to the suction surface at $r/R_t=0.9$ for the small flow rates. Similar vortices have been reported by Eckhardt (1976), Farge, Johnson and Maksoud (1989) and Ishida, Senoo and Ueki (1990) with their centrifugal compressors and by Engenda and Rautenberg (1987) with a centrifugal pump and were attributed to the combined effects of the pressure gradients, the blade tip leakage flow and the impeller-shroud relative motion. The passages of those earlier investigations had smaller aspect ratios and tip clearance-to-blade height ratios than the present impeller which may limit the extent of the leakage flow, so that the relative motion of the impeller and shroud would dominate, particularly at large radii where the tangential velocity of the relative motion was high.

The axial component of velocity (not shown in figure) is smaller than the other two components particularly in the central region of the passage and at small radii. Larger axial velocities occur at discharge and Figure 10 shows that the maximum and minimum are within $\pm 0.1W_t$. The axial velocities close to blade surfaces at smaller radii support form of the vortices discussed above.

3.3 Variations of Relative Flow in the Impeller with Rotation

Centrifugal pumps use volutes to collect the discharge from the impeller and are arranged to match the impeller discharge flow at the design flow rate. The cross sectional area of the passage is a function of the circumferential angle (Ψ) to maintain a constant angular momentum of the flow (Karassik *et al.*, 1976) with a cutwater to separate the outlet duct. The asymmetric shape of the volute generates circumferential pressure distribution which depends on the operating condition (Iversen *et al.*, 1960; Sideris and Van den Braembussche, 1987), and off-design operation results in larger pressure variations which, in turn, affect the flow in the impeller and pump performance (Bowerman and Acosta, 1957; Hamkins and Flack, 1987). The results in this sub-section describe the impeller flow measured at the circumferential angles Ψ of 60, 240 and 330 degrees at a flow rate of $0.57Q_n$.

The relative flows for Ψ of 60 and 240 degrees, Figure 18, correspond to the passage of Figure 12 and are similar to that at $\Psi=330$ degrees (Figure 12, $0.57Q_n$), with the velocity vectors and flow angles smaller at the smaller angles. The measurements at Ψ of 60 and 240 degrees allowed closer to the suction surface where the region of higher velocity at $r/R_t=0.65$, 0.71 and 0.8 , indicating acceleration due to the relative eddy, is clearly identified in Figures 18b and 18c, which was less obvious in Figure 12.

The profiles of velocity and flow angle on the mid-plane of the passage at discharge are shown in Figures 19 and 20, respectively, for the three locations and have lower mean values for the radial component and higher mean values for the absolute tangential component at $\Psi=60$ and 240 degrees, Figure 19, with the rms values similar at the three locations. The results suggest a variation of flow rate, and this is supported by the higher absolute tangential velocities for lower radial velocities. Figure 20 shows larger flow angles and uniform distribution at $\Psi=60$ degrees, in contrast to lower values and larger variation at $\Psi=330$

degrees, again suggesting the influence of the volute, and is related to the slip effect of the last sub-section. The radial velocity profiles were averaged over 360 degrees and resulted in $0.08W_t$, $0.092W_t$ and $0.116W_t$ for the profiles of $\Psi=60$, 240 and 330 degrees respectively. Area averages of the radial velocity profiles on the three axial planes over the peripheral area of the passage at discharge resulted in lower values of $0.044W_t$, $0.053W_t$ and $0.059W_t$ due to velocity gradients from hub to shroud. The results confirm that passage flow rates depend on the circumferential angles of the volute, with that at $\Psi=60$ and 240 degrees 25% and 10%, respectively, lower than that at $\Psi=330$ degrees. These variations of passage flow rate are associated with a flow rate of $0.57Q_n$ and could cause uneven momentum of discharge from the multiple passages of the impeller which, together with the volute pressure distribution, could give a net radial thrust exerting on the impeller.

3.4 Flows in the Volute Passage

Sub-section 3.3 has shown that the impeller discharge flow was not uniform, and the results in this sub-section consider the flow in the volute which stem from the impeller discharge. Velocities were measured in detail for the flow rate of $0.57Q_n$ with sample results for higher and lower flow rates.

Figure 21 shows that the streamwise component of mean velocity at Ψ of 60, 240 and 330 degrees in the volute at $0.57Q_n$ had a tendency to decelerate along the passage, and that the velocity varied with impeller shaft angle. The results at shaft angles $\theta=0$, 30 and 70 degrees are presented to identify the variations, based on velocity traces over 360 degrees. The radial profiles are characterised by velocity maxima at the impeller discharge with near-uniform distribution close to the volute wall. The profile close to the cutwater, $x/D_c=1.15$, has sharp gradient towards the cutwater and rapid deceleration on the back surface of the wall ($z=-1$, Figure 2), due to the influence of the cutwater and the divergence of the outlet duct. The deceleration along the passage of the volute is due to the geometry and operating conditions that the flow decelerates and static pressure increases

in the circumferential direction at flow rates below the design point (Binder and Knapp, 1958; Bowerman and Acosta, 1957; Hamkins and Flack, 1987). Flow acceleration and static pressure increasing in the circumferential direction would occur for the flow rates above the design point (Sideris and Van den Braembussche, 1987). Similar characteristics of volute flows have been reported by Van den Braembussche and Hände (1990) in a simplified geometry with a straight conical channel.

The rms velocities associated with the mean values of Figure 21 are presented in Figure 22 and show larger values at $\Psi=60$ degrees and near the cutwater where the maximum was $0.94W_t$ and the variations with shaft angle up to $0.2W_t$, indicating the local unsteadiness of the flow due to the interaction of the impeller and the cutwater. Local maxima of the rms velocity are also associated with velocity gradients of the mean flow.

The details of the flow near the cutwater are further identified in Figure 23 by the mean velocity vectors on the plane $z=0$ at five shaft angles and show large change near the cutwater with the vectors away from the cutwater insensitive to the rotation of the impeller. The stagnation point, inferred from the vectors, was on the outer surface of the lip at $0.57Q_n$, similar to the results of Miner, Beaudoin and Flack (1989), and moved towards the inner surface at higher flow rates. The location of the stagnation point may control out- or in-flow through the cutwater clearance at flow rates above and below the design point and separation when the stagnation point occurs at extreme positions (Binder and Knapp, 1958).

The decrease of flow rate caused a general decrease in circumferential velocity, Figures 21 and 24, and increased variation with shaft angle, as is evidenced by the typical values of the streamwise mean velocity of the near-uniform profiles at $\Psi=330$ degrees of $0.56W_t$, $0.53W_t$, $0.42W_t$ and $0.39W_t$ for Q/Q_n of 0.93, 0.57, 0.29 and 0.15 respectively, with variations of up to $0.06W_t$ at $0.93Q_n$ and $0.11W_t$ at $0.15Q_n$ based on 360-degree traces of velocity. The results are associated with the non-uniform discharge flow of the impeller, and the values of the

periodic variations of the mean velocity with impeller rotation were equivalent to around 11% of local velocity at $0.93Q_n$ and 28% at $0.15Q_n$.

Figure 25 shows the cross-stream mean flow in the volute in terms of velocity vectors on the plane of $\Psi=330$ degrees at five shaft angles and for flow rates of $0.93Q_n$ and $0.57Q_n$, obtained by resolving the radial and axial components of velocity. The transverse flow is mainly radially outward with little signature of the impeller rotation at $0.93Q_n$, except close to the impeller and in the region of small vectors. The cross-stream velocities decreased with flow rate which caused the formation of a counter-clockwise circulation. The flow in the outer region ($r/R_1 > 1.13$) of the cross section is almost insensitive to impeller rotation with the signature of blade passing detected only close to the impeller.

The variations of velocity with impeller rotation decayed in the outlet, Figure 26, with the velocity traces at $x/D_c=1.8$ and 3.2 the same as the measurements of Figures 6 and 7 where the velocities were 360-degree averaged. The variations of velocity in streamwise (U) and radial (V) directions were of the same order of magnitude and decreased with axial distance faster for the lower flow rate. Measurements at $x/D_c=3.2$, two exit pipe diameters downstream of the cutwater, and at the centre of the pipe (not shown in figure) showed that velocities varied slightly for the flow rates up to around $0.8Q_n$ and larger variations for higher flow rates. These variations corresponded to 14% and 6% of the local bulk mean velocity in the exit pipe for 100% and 80% of the design flow rate respectively. The separated wake and vorticity in the exit pipe of Figure 6 are expected to be responsible partly for the variations of mean velocity at lower flow rates.

3.5 Slip Factors

The angle-resolved radial and tangential velocities quantified the transfer of angular momentum to the flow and the slip factor inside the impeller. The normalised angular

momentum of the flow (M) and slip factor (S), according to Hamkins and Flack (1987), are calculated from the area- and mass-averaged radial and tangential velocities by integration of the measured angle-resolved values at each radial station. The expressions for M and S are defined as,

$$M = \frac{r \bar{w}}{R_t^2 \omega} \quad (1)$$

$$S = \frac{\bar{w}}{r\omega - v \tan \beta} \quad (2)$$

The slip factor is based on the ratio of the actual to theoretical values of absolute tangential velocity, and the angular momentum is normalised by the radius of impeller and angular speed of rotation, and both were evaluated at each radial station of measurement.

Figure 27 shows that the angular momentum of the flow increases with radius, as expected, to reach maxima of 0.62 and 0.66 at the discharge plane for $0.93Q_n$ and $0.29Q_n$ respectively. The tendency for the angular momentum to reach maxima inside the impeller is evident at $0.29Q_n$ and may be attributed to reverse blade loading at low flow rate according to Hamkins and Flack (1987). The ideal value of angular momentum based on the area-averages of measured radial velocity can be obtained by dividing equation (1) by equation (2), and the results suggest that the flow loses momentum along the radius with larger loss for the lower flow rate. The departure of angular momentum from ideal is due partly to the slip effect and partly to friction and is quantified by the slip factor of Figure 28 which has a trend opposite to that of angular momentum. The slip factor was larger than unity at small radii, supporting the effect of a relative eddy, and is in contrast to that reported by Hamkins and Flack (1987) who measured in the region of larger radii ($0.8 \leq r/R_t \leq 1$) where the slip factor was always less than one.

Figure 29 shows that the slip factors at the impeller discharge increased monotonically with flow rate, and they are

compared with the theoretical values of Stodola (μ) and Busemann (σ), defined by (Wiesner, 1967; Dixon, 1975):

$$\mu = 1 - \frac{\pi \cos \beta}{n}$$

$$\sigma = \frac{A_1 - A_2 \frac{V_R}{W_t} \tan \beta}{1 - \frac{V_R}{W_t} \tan \beta}$$

The formula of Stodola was obtained assuming no through-flow and the value of μ was 0.58 based on β of 58 degrees and n of 4. The Busemann slip factor σ was calculated using the theoretical radial velocity V_R in Table 3, with A_1 equal to 0.69, which is a constant depending on the number of blades and the blade angle, and A_2 equal to unity. The experimental value at $0.93Q_n$ was 0.78 which was around 15% and 25% larger than the theoretical values of Busemann and Stodola, respectively. The slip factors calculated by the velocities measured at Ψ of 60, 240 and 330 degrees at $0.57Q_n$ were within 6% with each other in spite of variations in passage flow rate of up to 25%, again demonstrating the influence of the volute.

4. CONCLUDING REMARKS

Measurements of turbulent flow in a centrifugal pump with an unshrouded impeller with four backward leaning blades and a single volute have been made by laser-Doppler velocimetry close to the recommended flow rate and at lower flow rates. A transparent casing with refractive index identical to that of the fluid allowed detailed examination of the inlet, a large part of inter-blade region, the volute and the outlet of the pump. The more important findings are summarised below:

1. The impeller flow departed from blade curvatures at off-design conditions with increased blade-to-blade variations of relative velocity, in contrast to a generally well-guided flow at the design flow rate. Decrease of flow rate from the design point caused deceleration of radial flow on the shroud surface and on

the suction surface of the blades and increase of secondary flows and vorticity in the passages. The radial velocity reversed close to the suction surface at flow rates below 30% of the design point and close to the shroud surface at all flow rates. The velocity measurements confirmed the influence of the relative eddy by higher velocity on the suction surface and near-stagnation flow near the pressure surface at small radii and lower flow rates. However, the geometry of the passage enhanced the influence of the relative motion between the shroud and impeller surfaces and the viscous effects, which, together with the leakage flow through the tip clearance of the blades, caused the secondary flow to be mainly from suction to pressure surface with vortices close to blade surfaces at smaller radii.

2. The unsteady effects of the impeller discharge are caused mainly by the blade-to-blade variations of the flow and partly by the variations in blade-passage geometry and with the circumferential angle of the volute. The measurements confirmed differences of the angle-resolved velocities between the four impeller passages, which increased with the decrease of flow rate and with maximum differences close to the surfaces of the blades. Differences in mean velocity of up to 2.5% and 6% of the impeller tip velocity for the radial and tangential components, respectively, were measured close to the design flow rate and up to 3% and 16% at the flow rate close to shut-down, and were related to the differences of up to 0.5 mm in blade dimensions and up to one degree in blade circumferential spacing. The variations of relative flow in the passages with the circumferential angle of the volute were identified by the velocities obtained at three circumferential angles of 60, 240 and 330 degrees downstream of the cutwater. The measurements at 57% of the design flow rate showed variations up to 25% of the discharge flow rate from the same passage at the three locations, which would caused a radial thrust to be exerted on the impeller.

3. The velocities in the volute passage decelerated in the circumferential direction at 57% of the design flow rate where the geometry of the volute was over-sized. The decrease of flow rate increased the variations of velocity with impeller rotation.

and the cross-stream flow formed a circulation, due to the increased non-uniformity of the impeller discharge flow and separation on the shroud surface. The variations of velocity decayed in the exit pipe and was around 4% of the impeller tip velocity at the design flow rate and a near constant level of around 1% for the flow rates below 80% of the design value at a station two pipe diameters downstream of the cutwater.

4. The results confirmed a continuous increase of angular momentum with radius to a maximum at discharge close to the design flow rate and larger departures of angular momentum from ideal at small flow rates due to the slip effect. The slip factor was larger than unity inside the impeller and decreased with radius. The slip factor at impeller discharge increased monotonically with flow rate, and the value of 0.78 at 93% of the design flow rate was around 15% and 25% larger than the theoretical values of Busemann and Stodola respectively.

ACKNOWLEDGEMENT

The authors benefitted from discussions with Drs. H. McDonald and D.G.N. Tse of Scientific Research Associates Inc., U.S.A. Thanks are also due to Mr P. Stanley for his contribution to the manufacture of the acrylic model, and to Mr. J. Laker for his construction of electronic components of the instrumentation.

REFERENCES

- Acosta, A.J. (1954) An experimental and theoretical investigation of two-dimensional centrifugal pump impellers. *Trans. ASME*, 76, 749.
- Adler, D. and Levy, Y. (1979) A laser-Doppler investigation of the flow inside a backswept, closed, centrifugal impeller. *J. Mech. Eng. Sci., IMechE*, 21, 1.
- Binder, R.C. and Knapp, R.T. (1958) Experimental determinations of the flow characteristics in the volutes of centrifugal pumps. *Trans. ASME*, 80, 649.
- van den Braembussche, R.A. and Hände, B.M. (1990) Experimental and theoretical study of the swirling flow in centrifugal compressor volutes. *J. Turbomachinery, Trans. ASME*, 112, 38.
- Bowerman, R.D. and Acosta, A.J. (1957) Effect of the volute on the performance of a centrifugal-pump impeller. *Trans. ASME*, 79, 1057.
- Cumpsty, N.A. (1989) Compressor Aerodynamics. Longman, U.K.
- Davis, M.C. and Flack, R.D. (1990) Laser velocimetry measurements in a laboratory vaned diffuser. *Experiments in Fluids*, 8, 1.
- Dean, Jr. R.C. and Senoo, Y. (1960) Rotating wakes in vaneless diffusers. *J. Basic Eng.*, *Trans. ASME*, 82, 563.
- Dixon, S.L. (1975) Fluid Mechanics, Thermodynamics of Turbomachinery. Pergamon Press.
- Eckardt, D. (1975) Instantaneous measurements in the jet-wake discharge flow of a centrifugal compressor impeller. *J. Eng. for Power, Trans. ASME*, 97, 337.
- Eckhardt, D. (1976) Detailed flow investigations within a high-speed centrifugal compressor impeller. *J. Fluids Eng.*, *Trans. ASME*, 98, 390.
- Eckhardt, D. (1980) Flow field analysis of radial and backswept centrifugal compressor impellers. Part 1: flow measurements using a laser velocimeter. in Performance Prediction of Centrifugal Pumps and Compressors. ASME-paper, 77.
- Engeda, A. and Reutenberg, M. (1987) Comparisons of the relative effect of tip clearance on centrifugal impeller. *J. Turbomachinery, Trans. ASME*, 109, 545.

- Farge, T.Z., Johnson, M.W. and Maksoud, T.M.A. (1989) Tip leakage in a centrifugal impeller. *J. Turbomachinery*, Trans. ASME, 111, 244.
- Fischer, K. and Thoma, D. (1954) Investigation of the flow conditions in a centrifugal pump. *Trans. ASME*, 76, 141.
- Flack, R.D., Hamkins, C.P. and Brady, D.R. (1987) Laser velocimeter turbulence measurements in shrouded and unshrouded radial flow pump impellers. *Int'l J. of Heat and Fluid Flow*, 8, 1, 16.
- Fowler, H.S. (1968) The distribution and stability of flow in a rotating channel. *J. Eng. for Power*, Trans. ASME, 90, 229.
- Hah, C. and Krain, H. (1990) Secondary flows and vortex motion in a high-efficiency backswept impeller at design and off-design conditions. *J. Turbomachinery*, Trans. ASME, 112, 7.
- Hamkins, C.P. and Flack, R.D. (1987) Laser velocimeter measurements in shrouded and unshrouded radial flow pump impeller. *J. Turbomachinery*, Trans. ASME, 109, 70.
- Howard, J.H.G. and Kittmer, C.W. (1975) Measured passage velocities in a radial impeller with shrouded and unshrouded configurations. *J. Eng. for Power*, Trans. ASME, 97, 207.
- Howard, J.H.G. and Lennemann, E. (1971) Measured and predicted secondary flows in a centrifugal impeller. *J. Eng. for Power*, Trans. ASME, 93, 126.
- Ishida, M., Senoo, Y. and Ueki, H. (1990) Secondary flow due to the tip clearance at the exit of centrifugal impeller. *J. Turbomachinery*, Trans. ASME, 112, 19.
- Iversen, H.W., Rolling, R.E. and Carlson, J.J. (1960) Volute pressure distribution, radial force on the impeller, and volute mixing losses of a radial flow centrifugal pump. *J. Eng. for Power*, Trans. ASME, 82, 136.
- Johnston, J.P., Halleen, R.M. and Lezius, D.K. (1972) Effects of spanwise rotation on the structure of two-dimensional fully developed turbulent channel flow. *J. Fluid Mech.*, 56, 3, 533.
- Karassik, I.J., Krutzsch, W.C., Fraser, W.H. and Messina, J.P. (editors) (1976) Pump Handbook. McGraw-Hill Inc.
- Khezzer, L., Vafidis, C. and Whitelaw, J.H. (1987) Laser velocimetry for the measurement of air velocity in a centrifugal compressor. Imperial College, Fluids Section Report FS/87/36.

- Kjork, A. and Lofdahl, L. (1989) Hot-wire measurements inside a centrifugal fan impeller. *J. Fluids Eng.*, Trans. ASME, **111**, 363.
- Krain, H. (1981) A study on centrifugal impeller and diffuser flow. *J. Eng. for Power*, Trans. ASME, **103**, 688.
- Krain, H. (1988) Swirling impeller flow. *J. Turbomachinery*, Trans. ASME, **110**, 122-128.
- Lennemann, E. and Howard, J.H.G. (1970) Unsteady flow phenomena in rotating centrifugal impeller passages. *J. Eng. for Power*, Trans. ASME, **92**, 65.
- Liu, C.H., Margary, R., Vafidis, C. and Whitelaw, J.H. (1990) Flow in the coolant passages of an internal combustion engine cylinder head. *Exp. in Fluids*, **10**, 50.
- Liu, C.H., Nouri, J.M., Vafidis, C. and Whitelaw, J.H. (1990) Experimental study of the flow in a centrifugal pump. in Proc. 5th Int'l Symp. on Appl. of Laser Techniques to Fluid Mechanics, Lisbon, Portugal, 9-12 July, 1990.
- Liu, C.H., Nouri, J.M., Whitelaw, J.H. and Tse, D.G.N. (1989) Particle velocity in swirling, confined flow. *Comb. Sci. and Tech.*, **68**, 131.
- Martelli, F. and Michelassi, V. (1990) Using viscous calculations in pump design. *J. Fluids Eng.*, Trans. ASME, **112**, 272.
- Miner, S.M., Beaudoin, R.J. and Flack, R.D. (1989) Laser velocimeter measurements in a centrifugal flow pump. *J. Turbomachinery*, Trans. ASME, **111**, 205.
- Moore, J. (1973) A wake and an eddy in a rotating, radial-flow passage. Part 1: experimental observations. *J. Eng. for Power*, Trans. ASME, **95**, 205.
- Moore, J., Moore, J.G. and Timmis, P.H. (1984) Performance evaluation of centrifugal compressor impellers using three-dimensional viscous flow calculations. *J. Eng. for Gas Turbine and Power*, Trans. ASME, **106**, 475.
- Murakami, M., Kikuyama, K. and Asakura, E. (1980) Velocity and pressure distributions in the impeller passages of centrifugal pumps. *J. Fluids Eng.*, Trans. ASME, **102**, 420.
- Nouri, J.M., Whitelaw, J.H. and Yianneskis, M. (1988) A refractive index matching technique for solid/liquid flows. In Laser Anemometry in Fluid Mechanics 3, Ladoan, 335.

- Nouri, J.M., Whitelaw, J.H. and Yianneskis, M. (1987) Particle motion and turbulence in dense two-phase flow. *Int'l J. Multiphase Flow*, **13**, 729.
- Paone, N., Riethmuller, M.L. and van den Braembussche, R.A. (1989) Experimental investigation of the flow in the vaneless diffuser of a centrifugal pump by particle image displacement velocimetry. *Exp. in Fluids*, **7**, 371.
- Rothe, P.H. and Johnston, J.P. (1976) Effects of system rotation on the performance of two-dimensional diffusers. *J. Fluids Eng., Trans. ASME*, **98**, 422.
- Schodl, R. (1980) A laser-two-focus (L2F) velocimeter for automatic flow vector measurements of turbomachineries. *J. Fluids Eng., Trans. ASME*, **102**, 412.
- Sideris, Th.M. and van den Braembussche, R.A. (1987) Influence of a circumferential exit pressure distortion on the flow in an impeller and diffuser. *J. Turbomachinery, Trans. ASME*, **109**, 48.
- Stanitz, J.D. (1952) Some theoretical aerodynamic investigations of impeller in radial- and mixed-flow centrifugal compressor. *Trans. ASME*, **74**, 473-497.
- Thomas, R.N., Kostrzewsky, G.J. and Flack, R.D. (1986) Velocity measurements in a pump volute with a non-rotating impeller. *Int'l J. Heat and Fluid Flow*, **7**, 1, 11.
- Thompson, B.E., Senaldi, J., Vafidis, C., Whitelaw, J.H. and McDonald, H. (1989) Flow in a model of the SSME main injector bowl. in Proc. CASI 1st Canadian Symposium on Aerodynamics, Ottawa, Canada, 4-5 Dec. 1989.
- Tse, D.G.N., Sabnis, J.S., McDonald, H. and Whitelaw, J.H. (1991) Active control of pressure, sound and velocity of centrifugal pumps. Scientific Research Associates Inc., Report R91-920036-A2.
- Vu, T.C. and Shyy, W. (1990) Viscous flow analysis as a design tool for hydraulic turbine components. *J. Fluids Eng., Trans. ASME*, **112**, 5.
- Whitfield, A. and Baines, N.C. (1990) Design of Radial Turbomachines. Longmans.
- Wiesner, F.J. (1967) A review of slip factor for centrifugal impellers. *J. Eng. for Power, Trans. ASME*, **89**, 558.

- Yianneskis, M., Cheung, R.S. and Tindal, M.J. (1988) A method of investigating flows in inlet ports of complex shape. in Proc. Int'l Conf. on Combustion in Engines. IMechE, London, 10-12 May.
- Yuasa, T. and Hineta, T. (1979) Fluctuation flow behind the impeller. *Bulletin of the JSME*, **22**, 174, 1746.

TABLE 1 Investigations of flows in centrifugal pumps and passages made by non-laser based techniques.

Authors (Year)	Experimental Techniques	Pump Configuration	Operating Range (Spec.)	Quantities Measured	Main Findings
Acosta (1954)	passage fixed pressure probe	<ul style="list-style-type: none"> laboratory pump shrouded impeller with parallel hub and shroud; $D_1=305$ mm; $Z_1=24$ mm; $\beta=60^\circ$ log spiral blades; $n=2, 4$ and 6 vaneless diffuser 	$N=150$ to 200 rpm; $\Phi=0.14$ to 0.31	static pressure	<ul style="list-style-type: none"> experimental data correlated well with the prediction by potential theory when the inlet flow to the vanes is optimised
Fischer & Thoma (1954)	dye-injection visualisation and rotoSCOPE	<ul style="list-style-type: none"> laboratory pump shrouded impeller; $D_1=280$ mm; $Z_1=20$ mm; $\beta=62^\circ$ log spiral blades; $n=6$ vaneless diffuser 	$N=450$ rpm $\Phi=0.2$ to $1.58 \Phi_n$	N/A	<ul style="list-style-type: none"> flow patterns different from the predictions of potential theory high velocity and wake regions observed near pressure and suction surfaces, respectively

TABLE 1 Continued (1)

Authors (Year)	Experimental Techniques	Pump Configuration	Operating Range (Spec.)	Quantities Measured	Main Findings
Bowerman & Acosta (1957)	static pressure tap; total-head probe; torque meter	<ul style="list-style-type: none"> laboratory pump with shrouded impeller and parallel hub and shroud; $D_t=262$ mm; $Z_t=30$ mm; $\beta=66.5^\circ$ log spiral blades three 2-D double volutes with log spiral walls to match 0.75, 1 and 1.2 of impeller design flow rate (Φ_1) 	$\Phi=0$ to 0.22 ($\Phi_1=0.117$)	static and dynamic pressure in volute; shaft power	<ul style="list-style-type: none"> volute flow qualitatively similar to potential flow with the degree of departure depending on flow rate volute flow subjected to real fluid effects due to impeller discharge the presence of the volute affected the performance of impeller to give a different pump characteristics at off-design operation efficiency highest near the matching point of the impeller-volute combination
Binder & Knapp (1958)	pitot tube with slide valve to synchronize impeller rotation	<ul style="list-style-type: none"> commercial pumps double suction Impeller; $D_t=350, 317$ mm; $Z_t=43, 39$ mm; $\beta=67.2^\circ, 70^\circ$; $n=8, 7$ single volute 	$N=2000$; 2500 rpm $(N_{sUS}$ $=1400,$ $\textcircled{2500}$ rpm; $=1720$ $\textcircled{2900}$ rpm)	velocity and pressure in volute	<ul style="list-style-type: none"> radial velocity distributions depended on flow rates with non-uniformity at high and low flow rates out- and in-flow in the cutwater region at high and low flow rates, respectively non-uniform velocity and pressure distributions related to the unbalanced radial force on the impeller

TABLE 1 Continued (2)

Authors (Year)	Experimental Techniques	Pump Configuration	Operating Range (Spec.)	Quantities Measured	Main Findings
Ivers, Rolli, & Carisc (1967)	static pressure taps and probe; strain-gauged bearing housing	<ul style="list-style-type: none"> commercial pump shrouded impeller; $D_1=258$ mm; $Z_1=13$ mm; $\beta=67.5^\circ$ log spiral blades; $n=9$ single volute 	$N=1000$ rpm; $Q=0$ to 300 GPM	static pressure in volute; shaft radial force	<ul style="list-style-type: none"> confirmed the correlation between the shaft radial force and the volute circumferential pressure distribution the magnitude and direction of net shaft radial forces varied with flow rate the radial force was a minimum around the best efficiency point
Fowler (1968)	passage fixed hot-wire probe; surface flow visualisation	<ul style="list-style-type: none"> 2-D channels with fixed height of 80 mm and 4° converging ($w_1=152$ mm), parallel ($w_1=135$ mm) and 10° diverging ($w_1=94$ mm) side walls; rotation in span-wise direction 	$Re=3 \times 10^3$ to 4×10^4 ; $Rn=0$ to 2.1; $Rn = \frac{\omega w_1}{U}$	passage exit velocity	<ul style="list-style-type: none"> convergence and divergence affected flow stability and had less effect on flow patterns the non-uniformity of velocity depended on the rotation number (Rn) and Reynolds number (Re) flow in the channel sensitive to downstream obstacles and adjacent channels

TABLE 1 Continued (3)

Authors (Year)	Experimental Techniques	Pump Configuration	Operating Range (Spec.)	Quantities Measured	Main Findings
Lennemann & Howard (1970)	hydrogen bubble tracer	<ul style="list-style-type: none"> laboratory pump shrouded and unshrouded impeller with parallel hub and shroud; $D_t=457$ mm; $Z_t=21$ mm; $\beta=64^\circ$ log spiral blades; $n=14$ vaneless diffuser 	<p>$N=140$rpm partial capacity ($\Phi_n=0.118$ $\odot 140$rpm)</p>	N/A	<ul style="list-style-type: none"> rotating stall with frequency lower than blade passing frequency at partial capacity influenced by the secondary flow patterns tip clearance influenced the secondary flow and the stall characteristics in the unshrouded impeller
Howard & Lennemann (1971)	passage fixed hot-film probe; hydrogen bubble tracer	<ul style="list-style-type: none"> similar to Lennemann & Howard (1970) 	<p>$N=140$rpm $\Phi=0.13$ ($\Phi_n=0.118$ $\odot 140$rpm)</p>	primary and secondary velocities	<ul style="list-style-type: none"> the deviation of streamwise velocity from those of usual primary flow was related to the secondary flow pattern
Johnston, Halleen & Lezius (1972)	static pressure taps; hydrogen bubble tracer	<ul style="list-style-type: none"> rectangular channel with height of 279 mm and width (w_1) of 39 mm fully developed flow rotating in span-wise direction 	<p>Re up to 35×10^3; Rn up to 0.57</p>	static pressure	<ul style="list-style-type: none"> boundary layer on the suction surface stabilised and thicker with the transition to turbulent flow suppressed large scale vortices developed on the pressure side boundary layer due to local destabilisation

TABLE 1 Continued (4)

Authors (Year)	Experimental Techniques	Pump Configuration	Operating Range (Spec.)	Quantities Measured	Main Findings
Moore (1973)	hot-wire probe; 5-hole pitot tube; static pressure taps	<ul style="list-style-type: none"> • 2-D diffuser with fixed height and entrance width (w_1) of 76 mm; 15° divergence angle; $A_2/A_1=3.1$ • rotation in span-wise direction 	$Re=5 \times 10^6$ $Rn=0.46$ to 1.78	mean and rms velocity; flow angle; static pressure	<ul style="list-style-type: none"> • large wake region on the suction surface at large flow rate and related with the secondary flow along the shroud and hub boundary layer from pressure to suction side • a pressure side eddy was observed at small flow rate
Howard & Kittmer (1975)	passage fixed hot-film probe; hydrogen bubble tracer	<ul style="list-style-type: none"> • similar to Lennemann & Howard (1970) • $\beta=68^\circ$ log spiral blades; $n=7$ • vaneless diffuser 	$N=140$ rpm $\Phi=1.11\Phi_n$ $(\Phi_n=0.134 @ 140$ rpm)	primary and secondary velocities	<ul style="list-style-type: none"> • stream-wise flows similar for the shrouded and unshrouded impellers with no tendency of separation • secondary flow patterns characterised by double vortices and a single vortex for the shrouded and unshrouded impellers, respectively, with the later influenced by tip leakage flow

TABLE 1 Continued (5)

Authors (Year)	Experimental Techniques	Pump Configuration	Operating Range (Spec.)	Quantities Measured	Main Findings
Rothe & Johnston (1976)	static pressure taps; hydrogen bubble tracer	<ul style="list-style-type: none"> • 2-D diffuser with fixed height of 279 mm and entrance width (w_1) of 39 mm; $A_2/A_1=1.4$ to 2.6 • rotating in span-wise direction 	<p>Re up to 3×10^4; Rn up to 0.2</p>	static pressure	<ul style="list-style-type: none"> • the stall pattern was more stable with rotation and occurred only on the suction surface • the suppression of turbulent mixing and shear stresses in the suction boundary layer and the Coriolis acceleration enhanced the stall to occur in the diffuser
Yuasa & Hineda (1979)	microphone; hot wire probe; anechoic chamber	<ul style="list-style-type: none"> • shrouded impeller with parallel hub and shroud; $D_1=278$ mm; $Z_1=12$ mm; $\beta=35^\circ$; $n=6$ • vaneless diffuser 	<p>Re=5×10^6 $\Phi=0.116$ and 0.206</p>	velocity and pressure behind the impeller discharge	<ul style="list-style-type: none"> • air replaced water as working fluid • pressure fluctuations affected by both viscous wake and circulation within blade passages • velocity and pressure fluctuation dominated by blade passing frequency and its harmonics with amplitudes decreasing with harmonic number and radius

TABLE 1 Continued (6)

Authors (Year)	Experimental Techniques	Pump Configuration	Operating Range (Spec.)	Quantities Measured	Main Findings
Murakami, Kikuyama & Asakura (1980)	3-hole yaw probe; oil film surface flow visualisation	<ul style="list-style-type: none"> shrouded impeller; $D_t=339$ mm; $Z_t=23$ mm; $\beta=63^\circ$ log spiral blades; $n=3$ and 7 single volute 	$N=400$ rpm $\Phi=0.33$ to $1.28\Phi_n$ $(\Phi_n=0.098 @ 400\text{rpm})$	primary and secondary velocities; static pressure	<ul style="list-style-type: none"> flow of the 7-blade impeller was better guided and coincided well with prediction by potential theory flow of the 3-blade impeller deviated from prediction at both design and off-design operations with separation on pressure surface at inner radii Busemann and Stodola slip factors correlated well with measurements for the 7-blade impeller, but under-estimated for the 3-blade impeller
Engeda & Rautenberg (1987)	pressure transducer; torque meter	<ul style="list-style-type: none"> five commercial pumps unshrouded and mixed-flow impeller; $D_t=404$ to 185 mm; $Z_t=17$ to 60 mm; $\beta=62^\circ$ to 66°; $n=6$ single volute 	$N_s=0.33, 0.57, 0.83, 1.23$ and 1.51 ; $\delta/Z_t=0.01$ to 0.16	head; flow rate; shaft power	<ul style="list-style-type: none"> increase of tip clearance caused a decrease of head, flow rate, input power and efficiency no evident dependence of tip clearance effect on specific speed

TABLE 2 Investigations of flows in centrifugal pumps made by laser velocimetry

Authors (Year)	Experimental Techniques	Pump Configuration	Operating Range (Spec.)	Quantities Measured	Main Findings
Thomas, Kostrzewsky & Flack (1986)	LDV	<ul style="list-style-type: none"> laboratory pump with shrouded impeller and parallel hub and shroud; $D_t=203.2$ mm; $Z_t=12.7$ mm; $\beta=74^\circ$ log spiral blades; $n=4$ 2-D single volute 	$\Phi=1.2$ and $1.6\Phi_n$	V, W	<ul style="list-style-type: none"> impeller replaced by two 32-vane swirlers to simulate the discharge flows radial and circumferential non-uniformity of velocity in the volute attributed to geometric mismatching of discharge flow angles and volute angle
Hamkins & Flack (1987)	LDV	<ul style="list-style-type: none"> laboratory pump shrouded and unshrouded impeller with parallel hub and shroud; $D_t=203.2$ mm; $Z_t=12.7$ mm; $\beta=74^\circ$ log spiral blades; $n=4$ 2-D single volute 	$N=620$ rpm $\Phi=0.4$ to $1.35\Phi_n$; $\delta/Z_t=0.06$; 0.08 $(N_{sus} \approx 1200,$ $\Phi_n=0.063)$	V, W	<ul style="list-style-type: none"> passage vortex in the unshrouded impeller was caused by tip leakage and relative wall motion slip factor decreased with radius and decreased with flow rate angular momentum increases uniformly with radius at impeller-volute matched flow rate but had a peak at inner radius at lower flow rate

TABLE 2 Continued (1)

Authors (Year)	Experimental Techniques	Pump Configuration	Operating Range (Spec.)	Quantities Measured	Main Findings
Flack, Hamkins & Brady (1987)	LDV	<ul style="list-style-type: none"> similar to Hamkins & Flack (1987) 	<p>$N=620\text{rpm}$ $\Phi=0.2$ to $1.35\Phi_n$ $(N_{9US}=1200,$ $\Phi_n=0.063)$</p>	<p>$V, W,$ $v', w', \overline{vw'}$</p>	<ul style="list-style-type: none"> more uniform velocity and lower turbulence level with shrouded impeller normal stress higher with negative shear stress values on the suction surface
Sideris, van den Braembussche (1987)	LDV; static pressure taps	<ul style="list-style-type: none"> shrouded mixed flow impeller; $D_t=204$ mm; $Z_t=20$ mm; $\beta=63.5^\circ$ log spiral blades; $n=8$ vaneless diffuser followed by a volute 	<p>$N=300\text{rpm}$ $Q=0.0026,$ 0.0054 and 0.0066 m^3/s</p>	<p>V, W and static pressure in vaneless diffuser</p>	<ul style="list-style-type: none"> static pressure in the volute increased, near constant and decreased with circumferential positions for low, medium and high flow rates, respectively. circumferential variations of velocity in the diffuser due to pressure were confirmed
Miner, Beaudoin & Flack (1989)	LDV	<ul style="list-style-type: none"> similar to Hamkin & Flack (1987); passage height increased to $Z_t=24.6$ mm 	<p>$N=620\text{rpm}$ $\Phi=0.4$ to $1.06\Phi_n$ $(N_{9US}=1583,$ $\Phi_n=0.063)$</p>	<p>V, W</p>	<ul style="list-style-type: none"> non-axisymmetric impeller flow at design flow rate radial flow reversal at 40% design flow rate free-vortex-like flow in the volute with blade passing rapidly damped with radius

TABLE 2 Continued (2)

Authors (Year)	Experimental Techniques	Pump Configuration	Operating Range (Spec.)	Quantities Measured	Main Findings
Paone, Riethmuller, van den Braembussche (1989)	PIDV	<ul style="list-style-type: none"> similar to Sideris & van den Braembussche (1987) 	<ul style="list-style-type: none"> $N=300$ rpm $Q=0.0026, 0.0054, 0.0066$ m³/s 	<ul style="list-style-type: none"> instantaneous velocity vectors in vaneless diffuser 	<ul style="list-style-type: none"> well guided flow at high flow rate flow separation on suction surface at low flow rate slip factors of 0.9 and 0.55 at impeller discharge for low and high flow rate, respectively
Davis & Flack (1990)	LDV	<ul style="list-style-type: none"> laboratory vaned diffuser with swirler generated inlet flow and downstream baffle vanes $D_1=270$ mm; $D_2=390$ mm; $Z_1=12.7$ mm; $\beta=70^\circ$; $n=0, 2, 4, 6$ and 8 	$\Phi > \Phi_n$	<ul style="list-style-type: none"> V, W, v', w' 	<ul style="list-style-type: none"> swirler discharge flow had 14° incident angle to the diffuser vane to represent the condition of larger-than-design flow rate large region of separation behind the diffuser vanes with counter rotating vortex pair

TABLE 3 Experimental conditions

Flow conditions	I	II	III	IV
Q (m ³ /s)	2.52×10^{-3}	1.57×10^{-3}	8×10^{-4}	4×10^{-4}
Q/Q_n	0.93	0.57	0.29	0.15
ϕ	0.054	0.034	0.017	0.0086
Γ	0.446	0.512	0.554	0.568
N_s	0.425	0.304	0.203	0.142
N_{sUS}	917	647	443	303
<i>Inlet pipe</i>				
U_i (m/s)	2.47	1.54	0.79	0.39
Re_i	54500	34000	17300	8670
<i>Exit pipe</i>				
U_e (m/s)	3.94	2.46	1.25	0.63
Re_e	69000	43000	22000	11000
<i>Impeller passages</i>				
V_R (m/s)	1.08	0.67	0.34	0.17
W_R (m/s)	17.3	18.	18.5	18.8

TABLE 4 Characteristics of the laser-Doppler velocimeter

<i>Transmitting optics</i>		
Laser: 1 watt Ar-Ion laser		
max. operating power	400	mW
wave-length	514.5	nm
Beam intersection angle	9.69	deg
Measurement volume diameter at $1/e^2$ intensity	52	μm
Measurement volume length at $1/e^2$ intensity	620	μm
Fringe spacing	3.04	μm
Number of fringes	17	
Frequency shift	0-13	MHz
<i>Receiving optics</i>		
Focal length of collimating lens	200	mm
Focal length of focusing lens	100	mm
Diameter of pinhole	100	μm
Effect length of measurement volume for 90° collection angle	200	μm

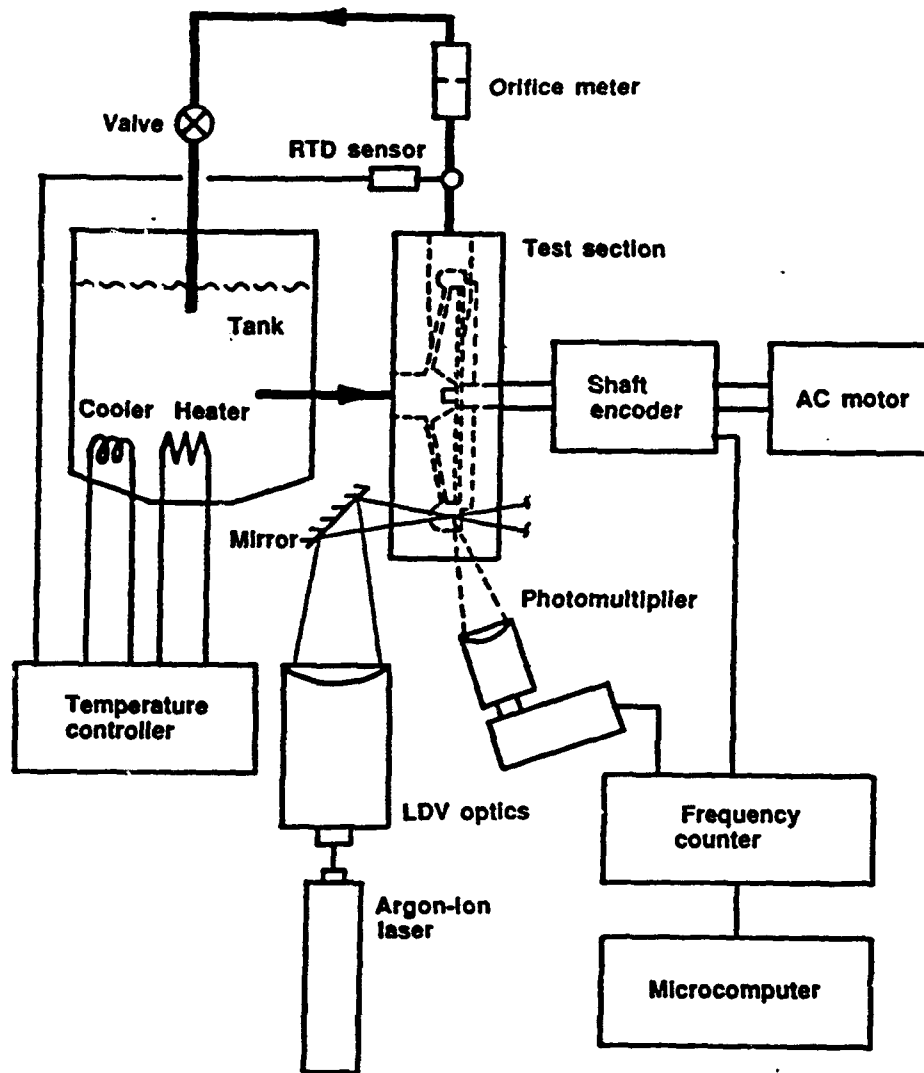


FIGURE 1 Flow configuration and instrumentation.

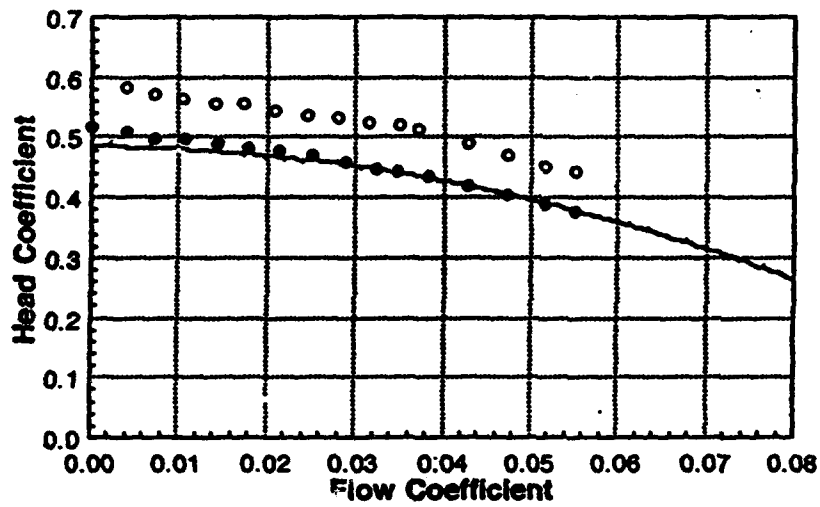


FIGURE 3 Head coefficient of the pump running at 2910 rpm.
 (\circ perspex casing; \bullet metal casing; — manufacturer's specification)

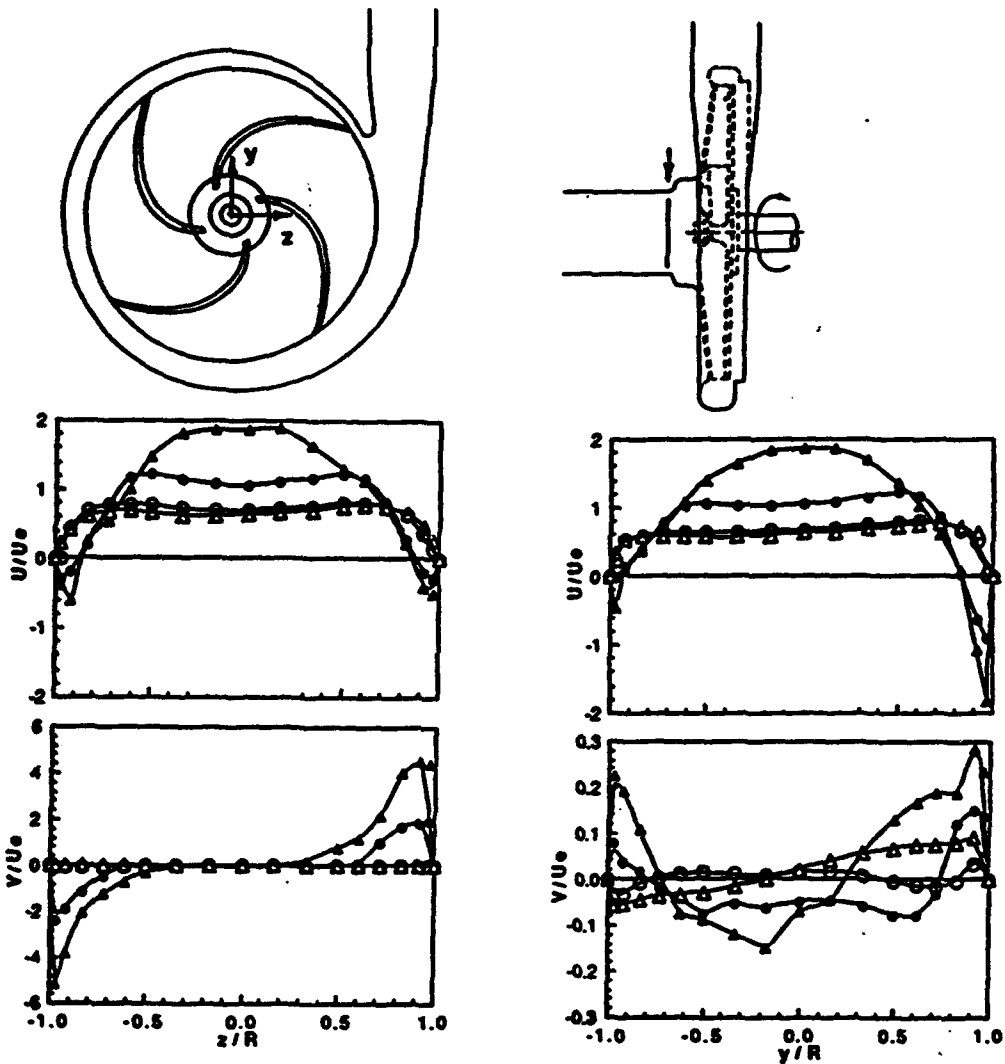


FIGURE 4 Radial profiles of x-component (U/U_c) and y-component (V/U_c) of mean velocity at the axial station z/D_1 of 0.7 in the inlet pipe and flow rates of $0.93Q_n$ (Δ), $0.57Q_n$ (\circ), $0.29Q_n$ (\cdot) and $0.15Q_n$ (\triangle).

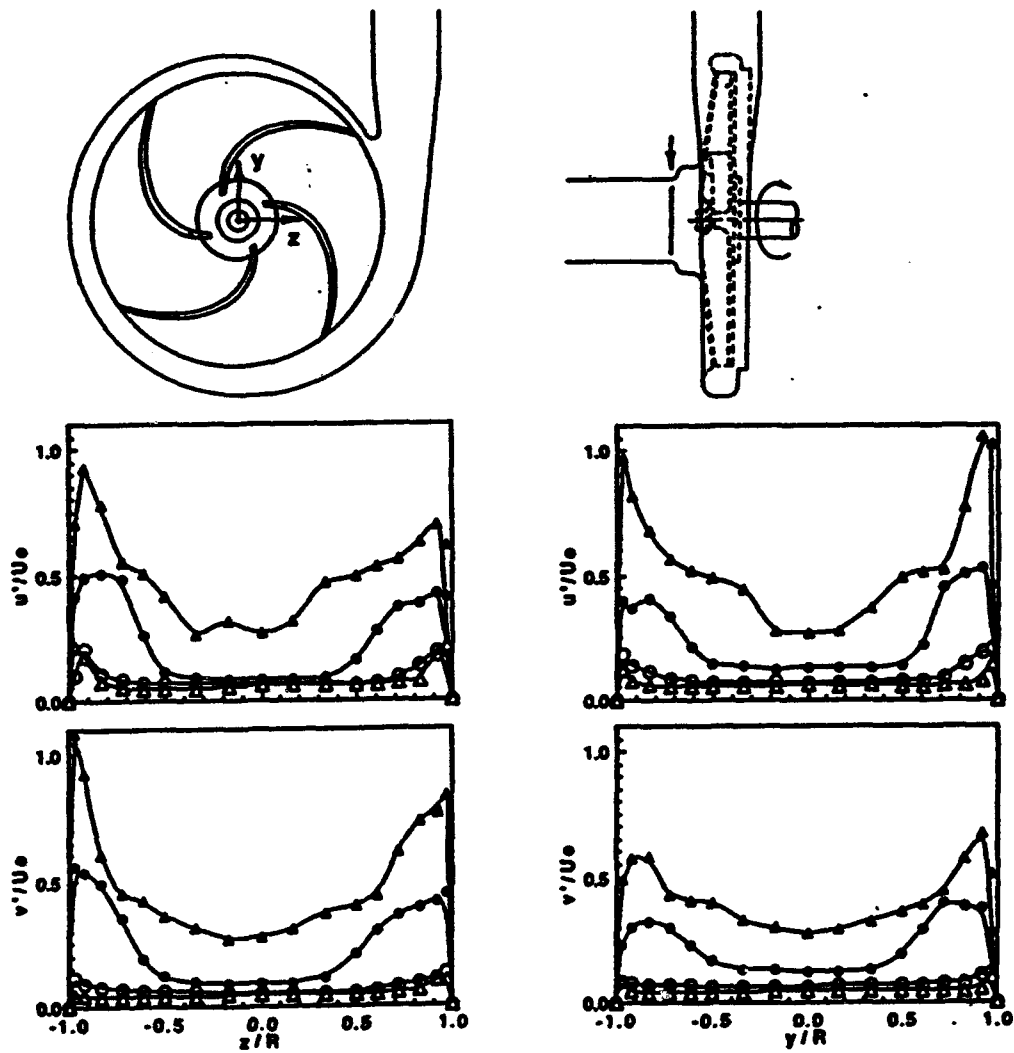


FIGURE 5. Radial profiles of x-component (u'/U_e) and y-component (v'/U_e) of rms velocity at the axial station z/D_1 of 0.7 in the inlet pipe and flow rates of $0.93Q_n$, $0.57Q_n$, $0.29Q_n$ and $0.15Q_n$. (see Figure 4 for symbols)

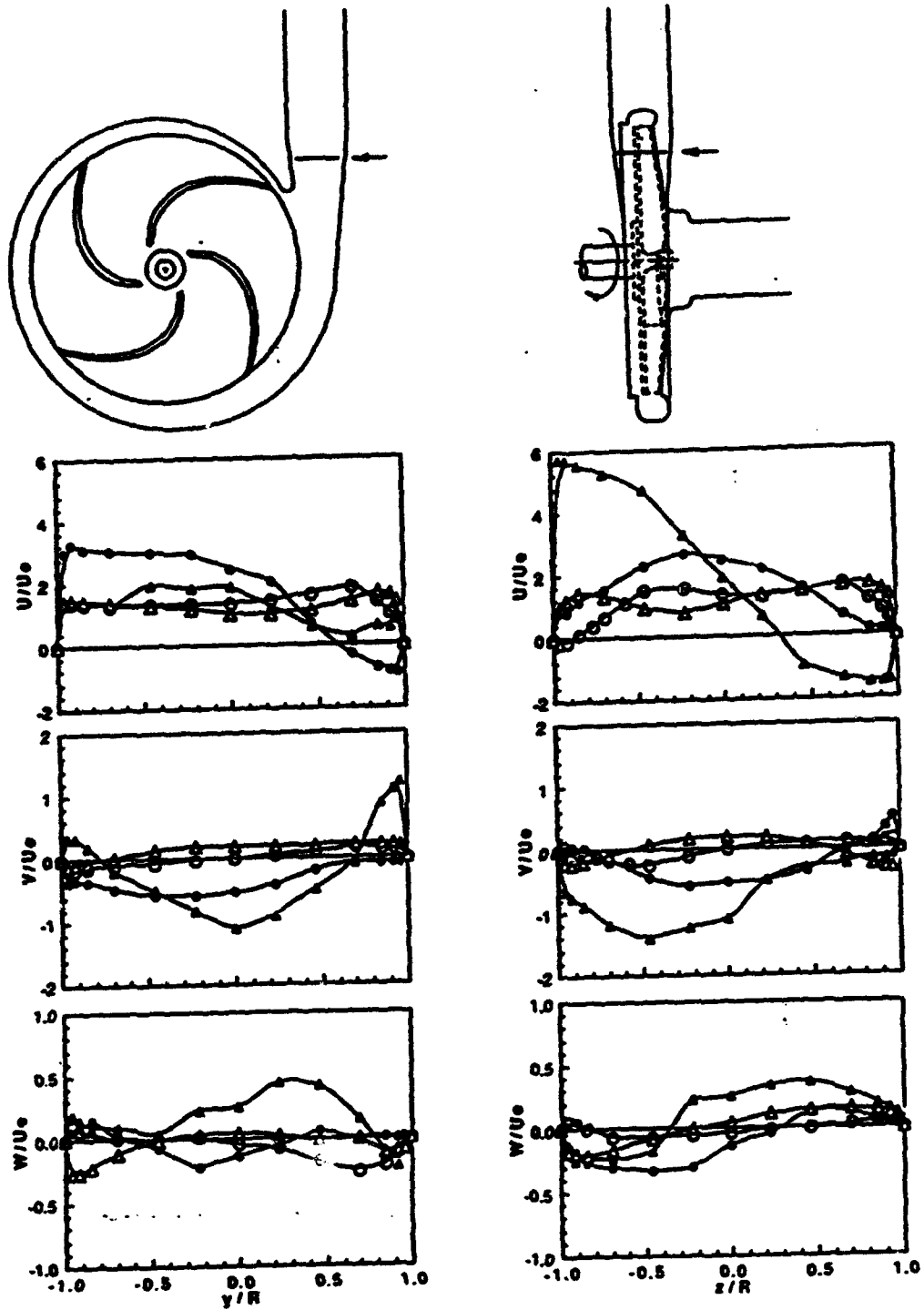


FIGURE 6 Radial profiles of x-component (U/U_e) and y-component (V/U_e) of mean velocity at the axial station x/D_e of 1.8 in the exit pipe and flow rates of $0.93Q_n$, $0.57Q_n$, $0.29Q_n$ and $0.15Q_n$. (see Figure 4 for symbols)

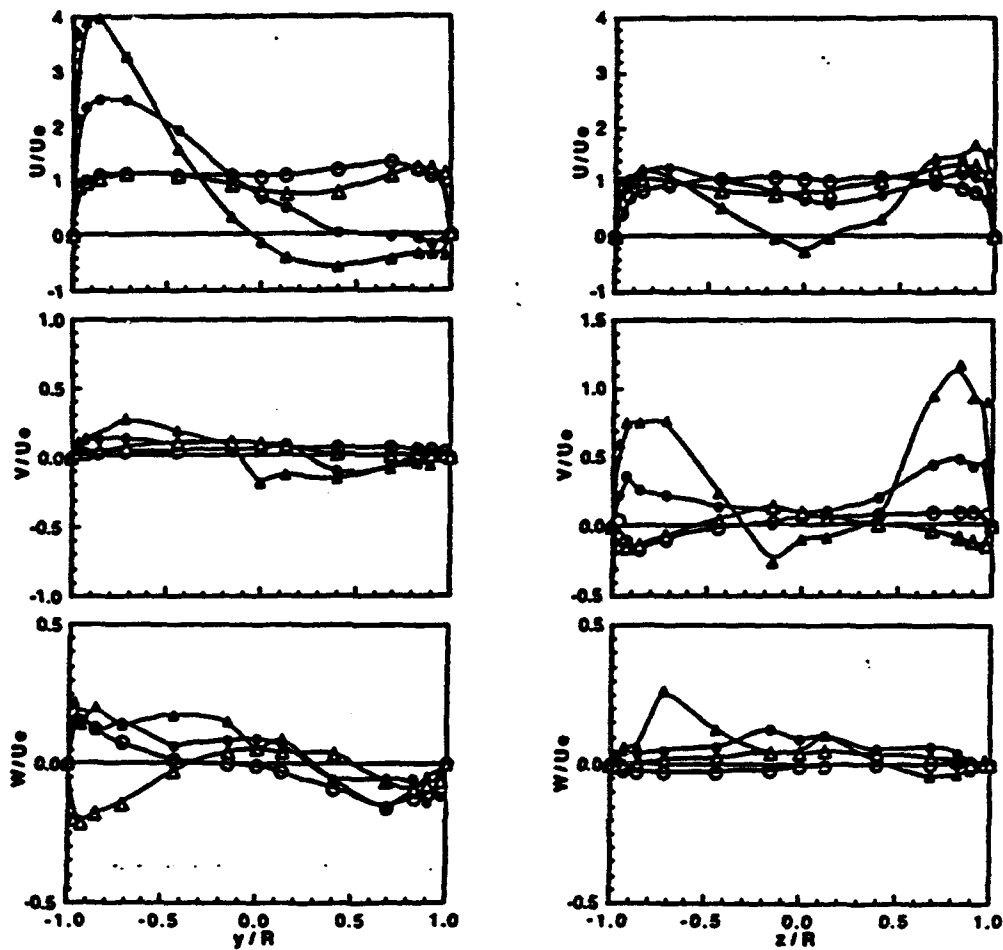
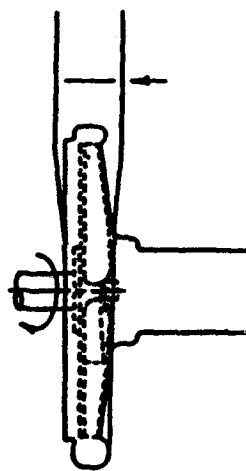
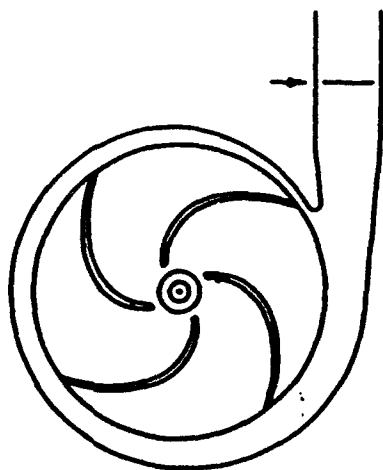


FIGURE 7 Radial profiles of x-component (U/U_e) and y-component (V/U_e) of mean velocity at the axial station x/D_e of 3.2 in the exit pipe and flow rates of $0.93Q_n$, $0.57Q_n$, $0.29Q_n$ and $0.15Q_n$. (see Figure 4 for symbols)

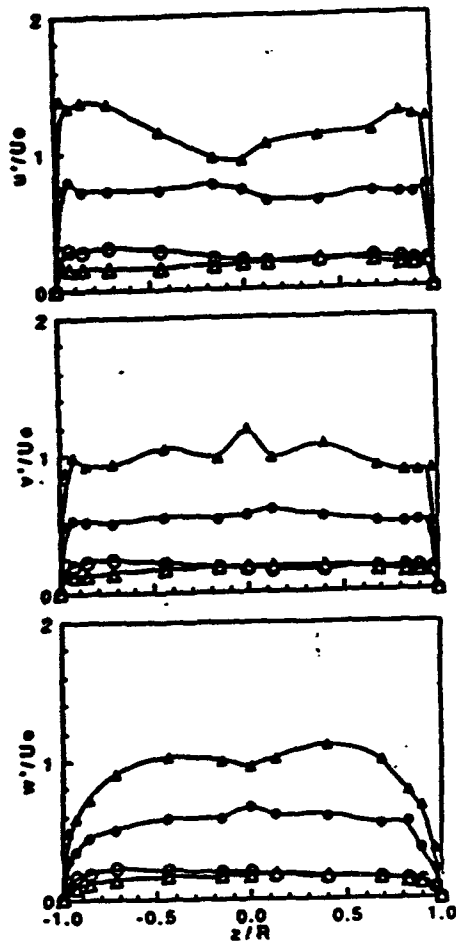
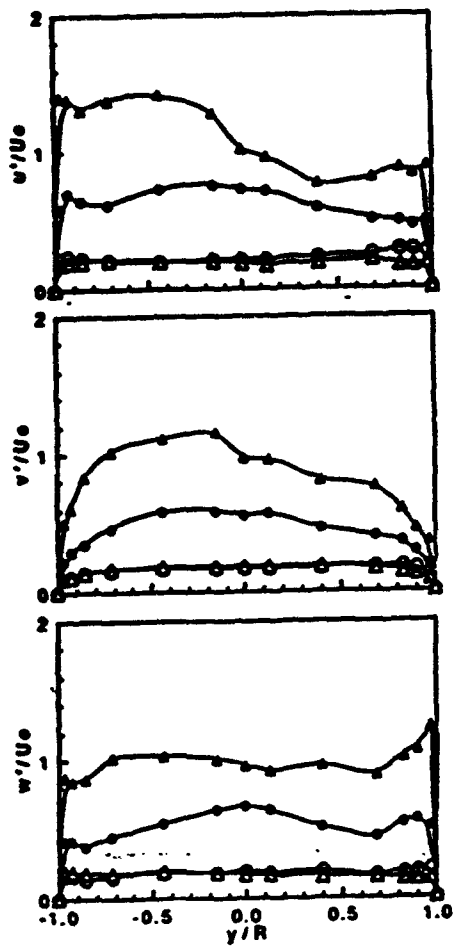
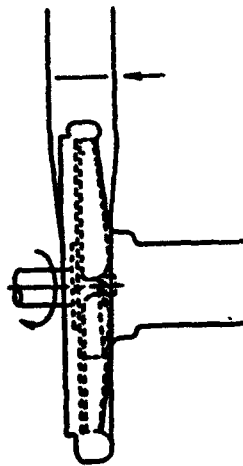
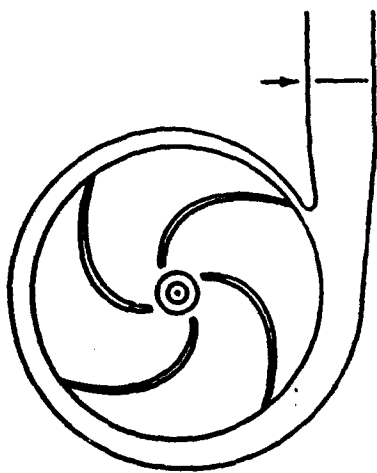


FIGURE 8 Radial profiles of x-component (u'/U_e) and y-component (v'/U_e) of rms velocity at the axial station x/D_e of 3.2 in the exit pipe and flow rates of $0.93Q_n$, $0.57Q_n$, $0.29Q_n$ and $0.15Q_n$. (see Figure 4 for symbols)

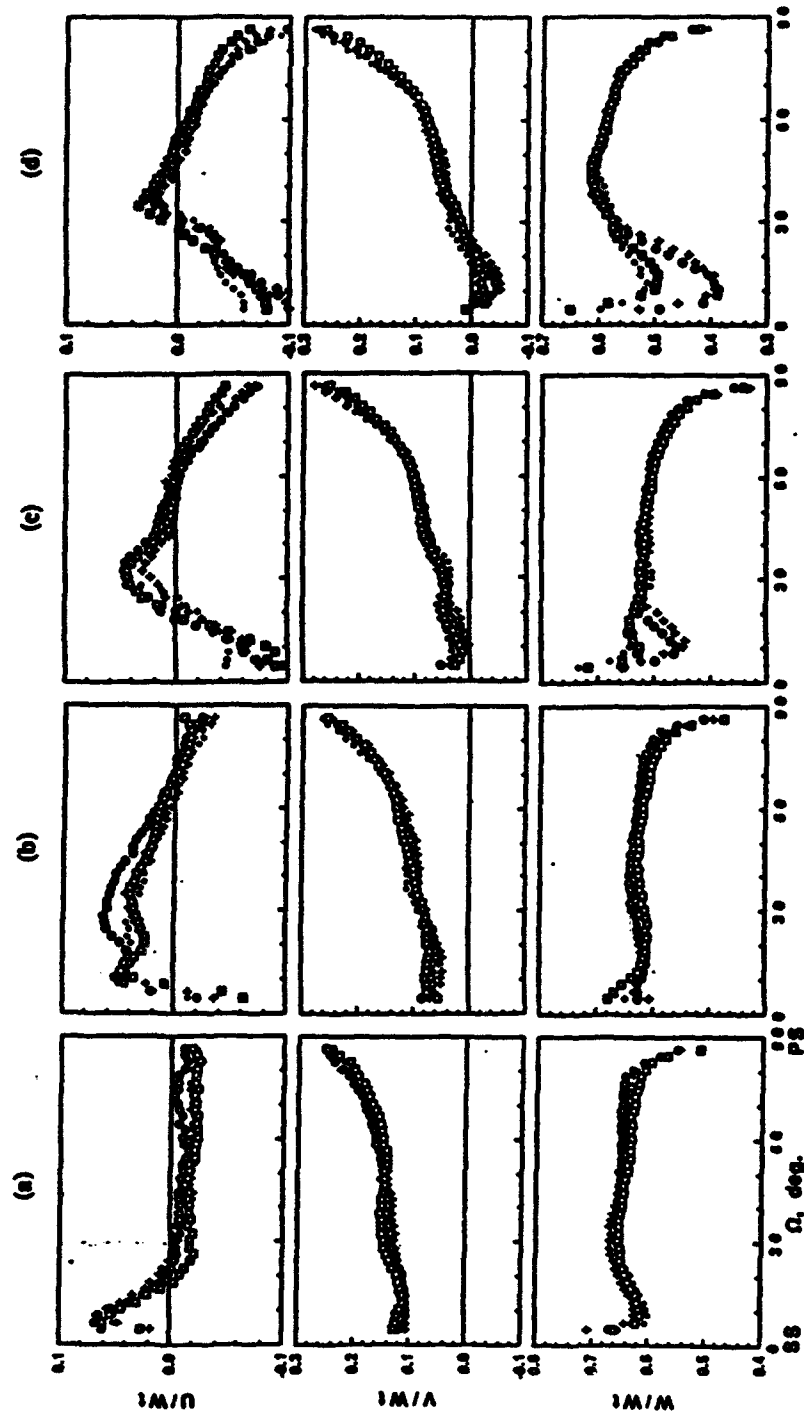


FIGURE 9 Blade-to-blade distributions of angle-resolved axial (U/W), radial (V/W) and tangential (W/W) components of mean velocity on the mid-plane of the impeller passage at discharge, $z/Z_t=0.5$ and $r/R_t=1$, measured at $\psi=330$ degrees and the flow rates of (a) $0.93Q_n$, (b) $0.57Q_n$, (c) $0.29Q_n$ and (d) $0.15Q_n$. Symbols for each of the four impeller passages.

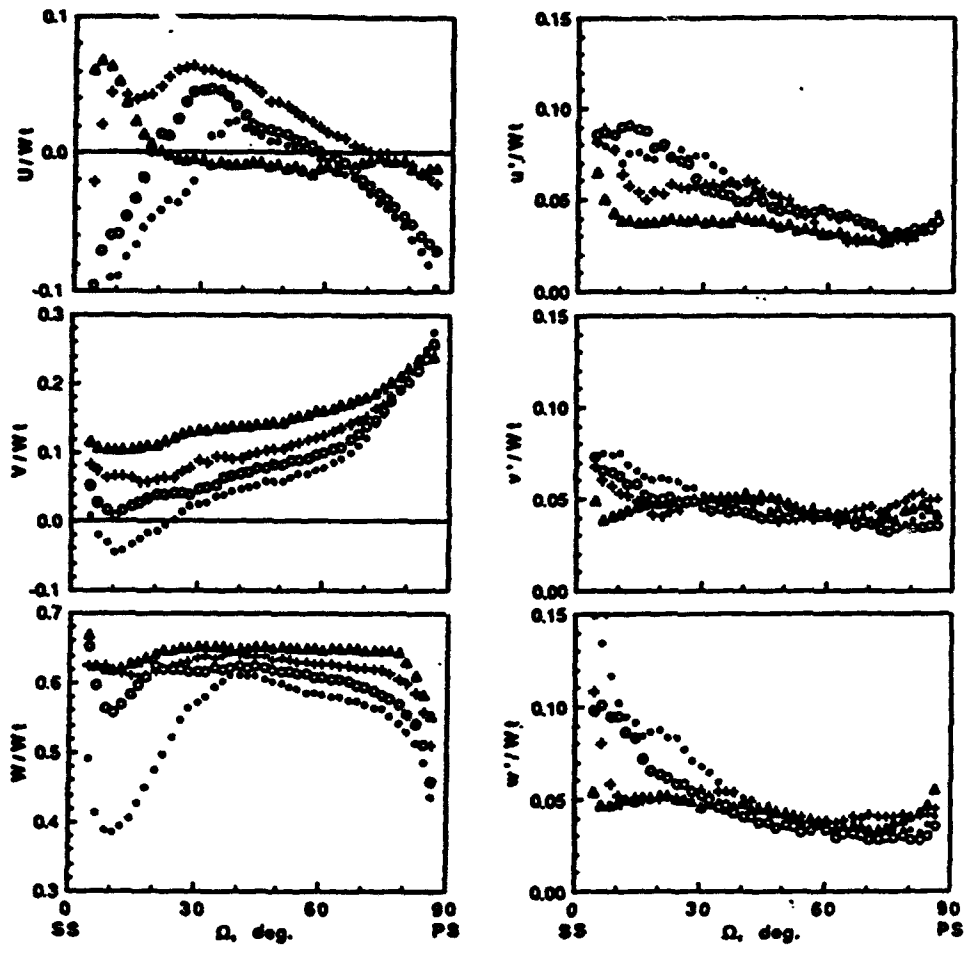


FIGURE 10 Blade-to-blade distributions of angle-resolved axial (U/W_t and u'/W_t), radial (V/W_t and v'/W_t) and tangential (W/W_t and w'/W_t) components of mean and rms velocities on the mid-plane of the impeller passage at the discharge, $r/R_t=1$ and $z/Z_t=0.5$, measured at $\Psi=330$ degrees and the flow rates of $0.93Q_n$ (Δ), $0.57Q_n$ ($+$), $0.29Q_n$ (\circ) and $0.15Q_n$ (\cdot).

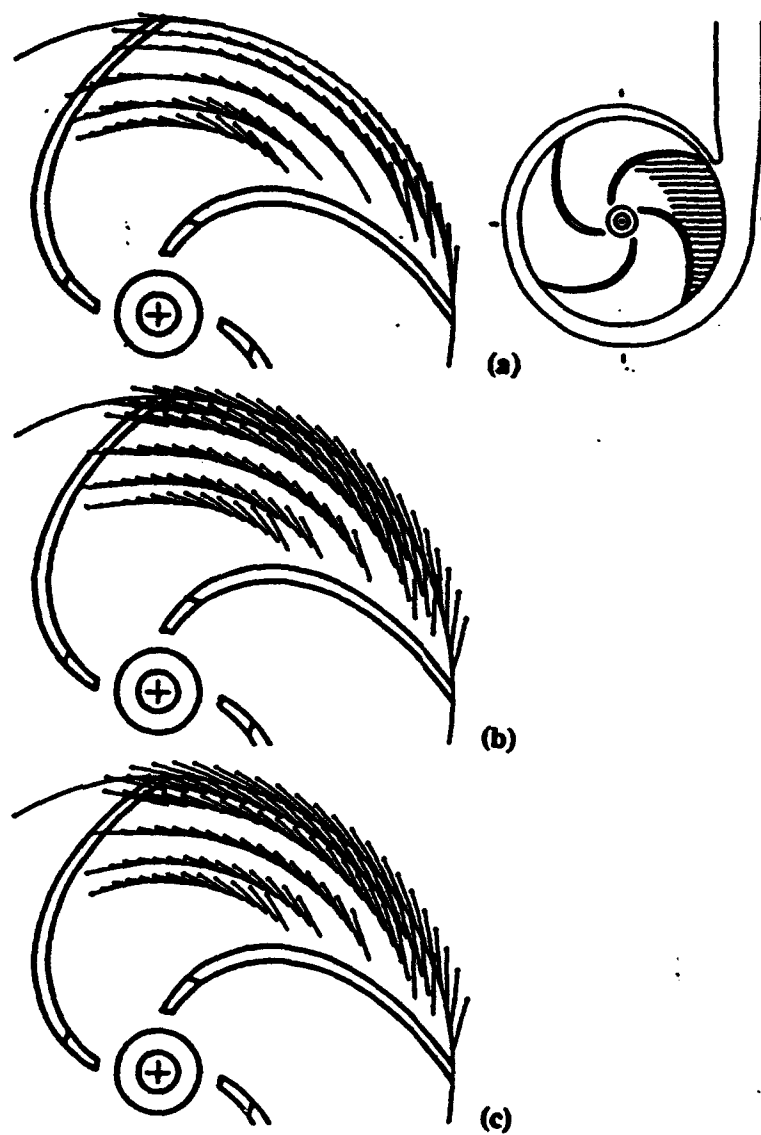


FIGURE 11 Mean velocity vectors of the absolute flow in an impeller passage at the flow rate of $0.93Q_n$ measured at $\Psi=330$ degrees. Radial locations $r/R_t=0.65, 0.71, 0.81, 0.9, 0.95$ and 1 .

(a) plane 1 mm from the shroud

(b) the mid-plane of the blade height

(c) plane 1 mm from the impeller hub

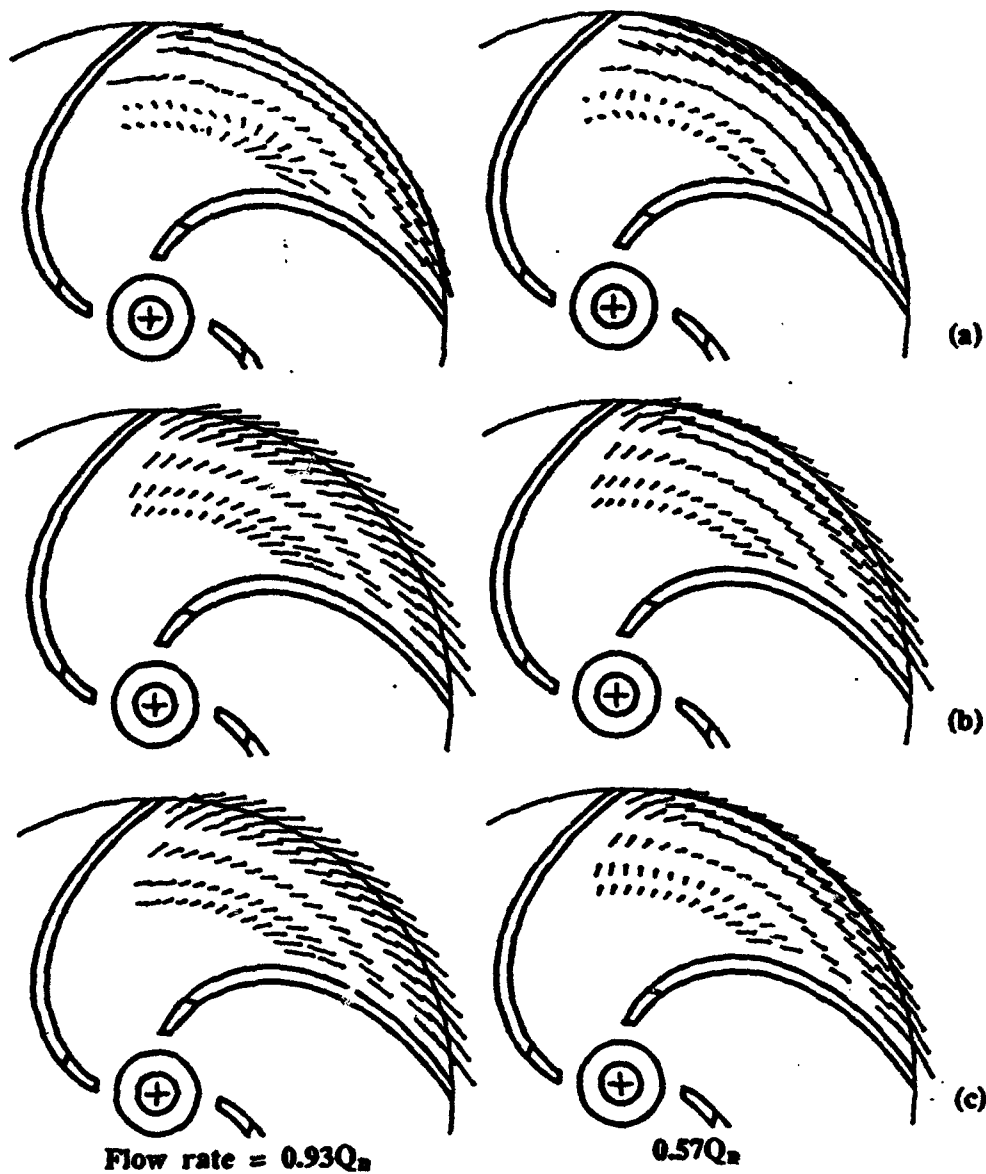


FIGURE 12 Mean velocity vectors of the relative flow in an impeller passage at the flow rates of $0.93Q_n$, $0.57Q_n$, $0.29Q_n$ and $0.15Q_n$ measured at $\Psi=330$ degrees. (see Figure 11 for radial locations)
 (a) plane 1 mm from the shroud
 (b) the mid-plane of the blade height
 (c) plane 1 mm from the impeller hub

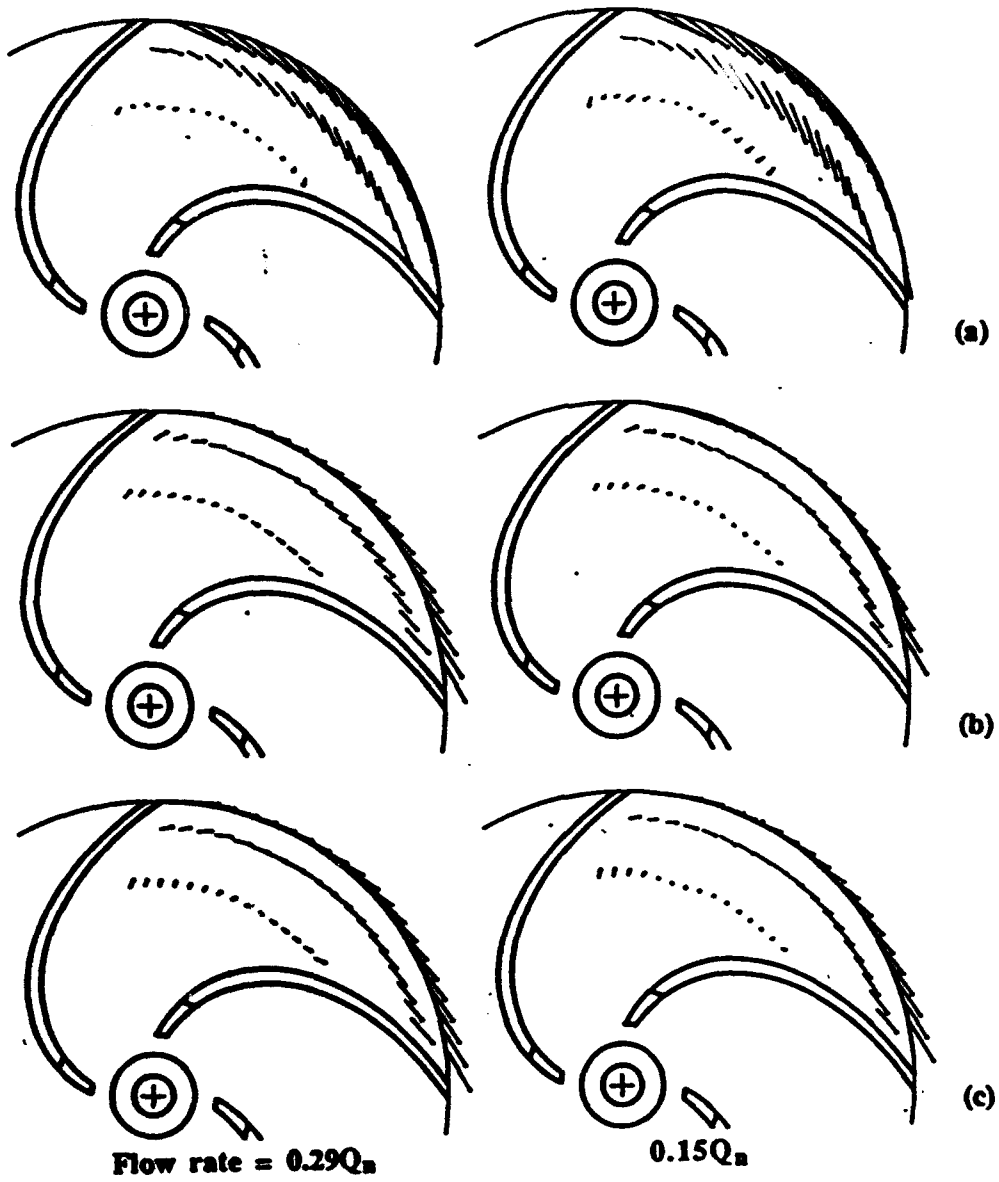


FIGURE 12 Continued.

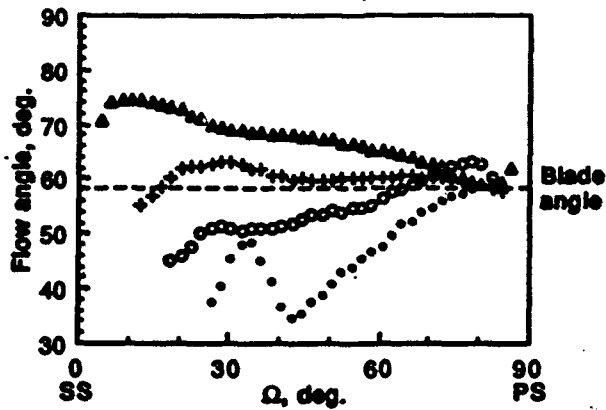


FIGURE 13 Blade-to-blade distributions of mean flow angle on the mid-plane of the impeller passage, $z/Z_1=0.5$, at the flow rate of $0.93Q_n$ measured at $\Psi=330$ degrees with the radial locations $r/R_1=0.7$ (\cdot), 0.8 (\circ), 0.9 ($+$) and 1 (Δ).

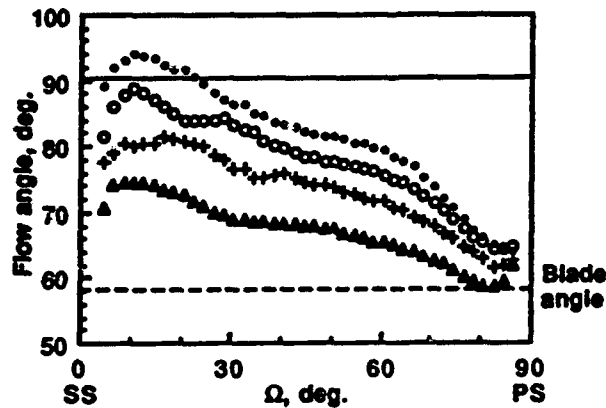


FIGURE 14 Blade-to-blade distributions of mean flow angle on the mid-plane of the impeller passage at discharge, $z/Z_1=0.5$ and $r/R_1=1$, measured at $\Psi=330$ degrees. (see Figure 10 for symbols)

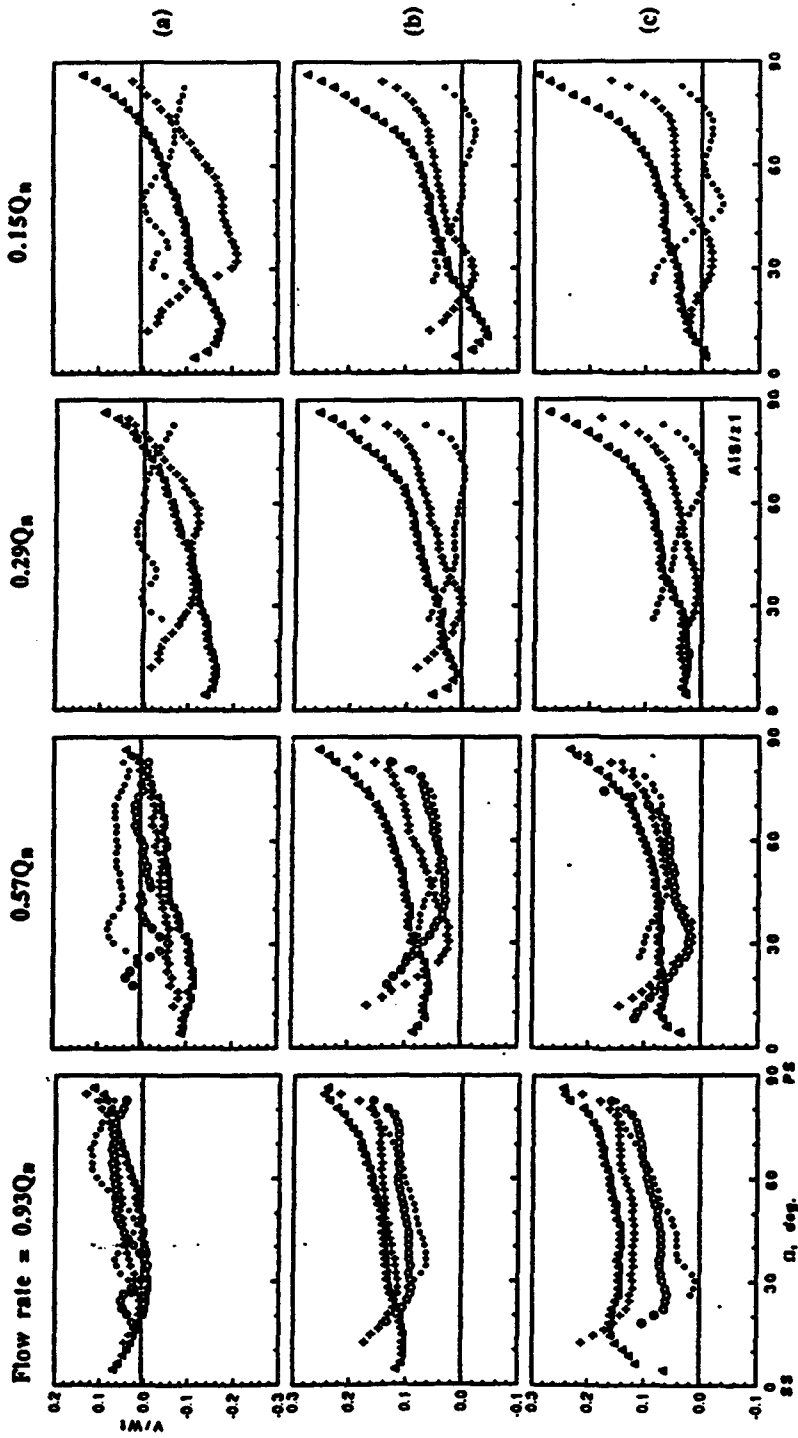


FIGURE 15 Blade-to-blade distributions of angle-resolved radial component of mean velocity (V/W_1) at the flow rates of $0.93Q_n$, $0.57Q_n$, $0.29Q_n$ and $0.15Q_n$ measured at $\psi=330$ degrees. (see Figure 13 for symbols)
 (a) plane 1 mm from the shroud
 (b) the mid-plane of the blade height
 (c) plane 1 mm from the impeller hub

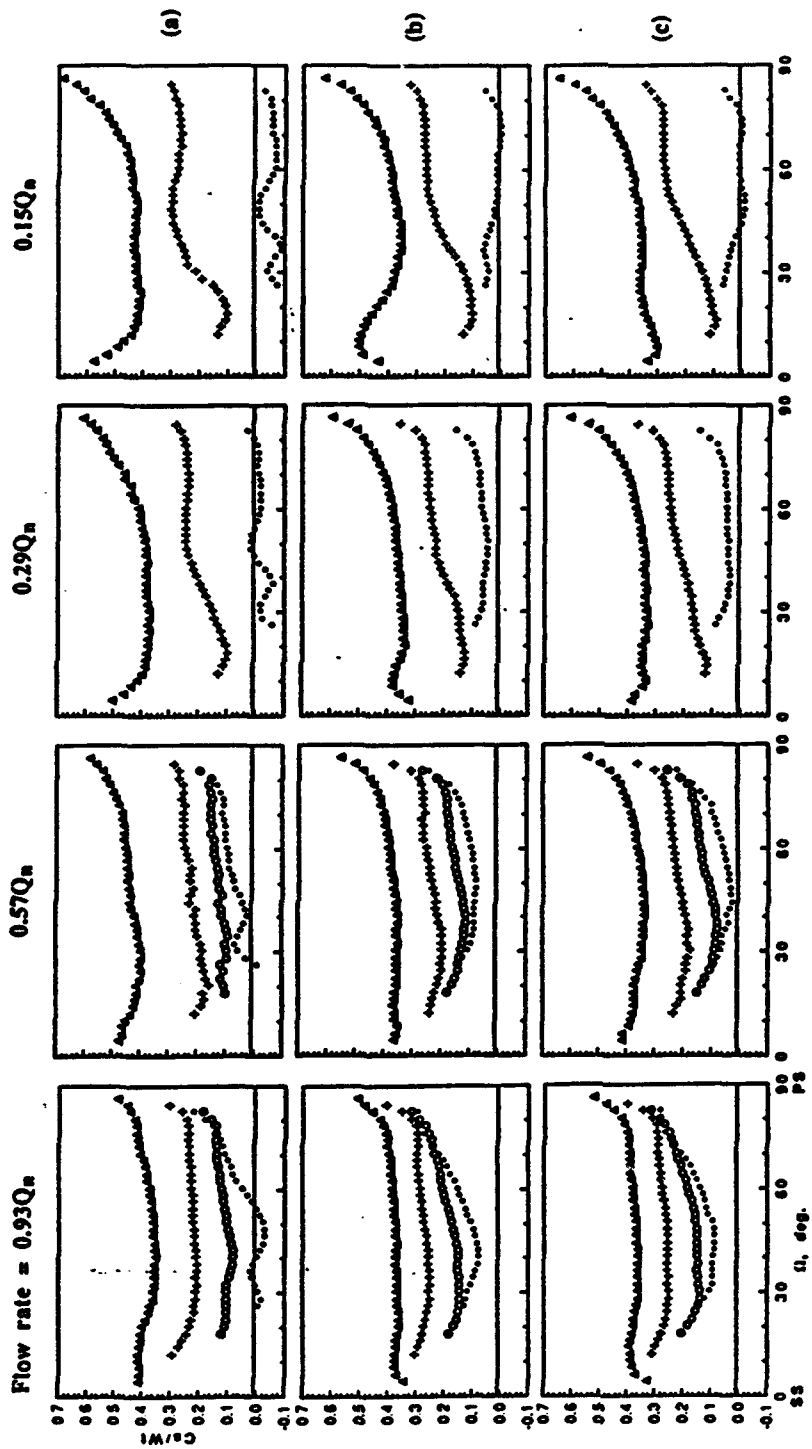


FIGURE. 16 Blade-to-blade distributions of angle-resolved streamwise component of mean velocity (C_s/W) at the flow rates of $0.93Q_n$, $0.57Q_n$, $0.29Q_n$ and $0.15Q_n$ measured at $\psi=330$ degrees. (see Figure 13 for symbols)
 (a) plane 1 mm from the shroud
 (b) the mid-plane of the blade height
 (c) plane 1 mm from the impeller hub

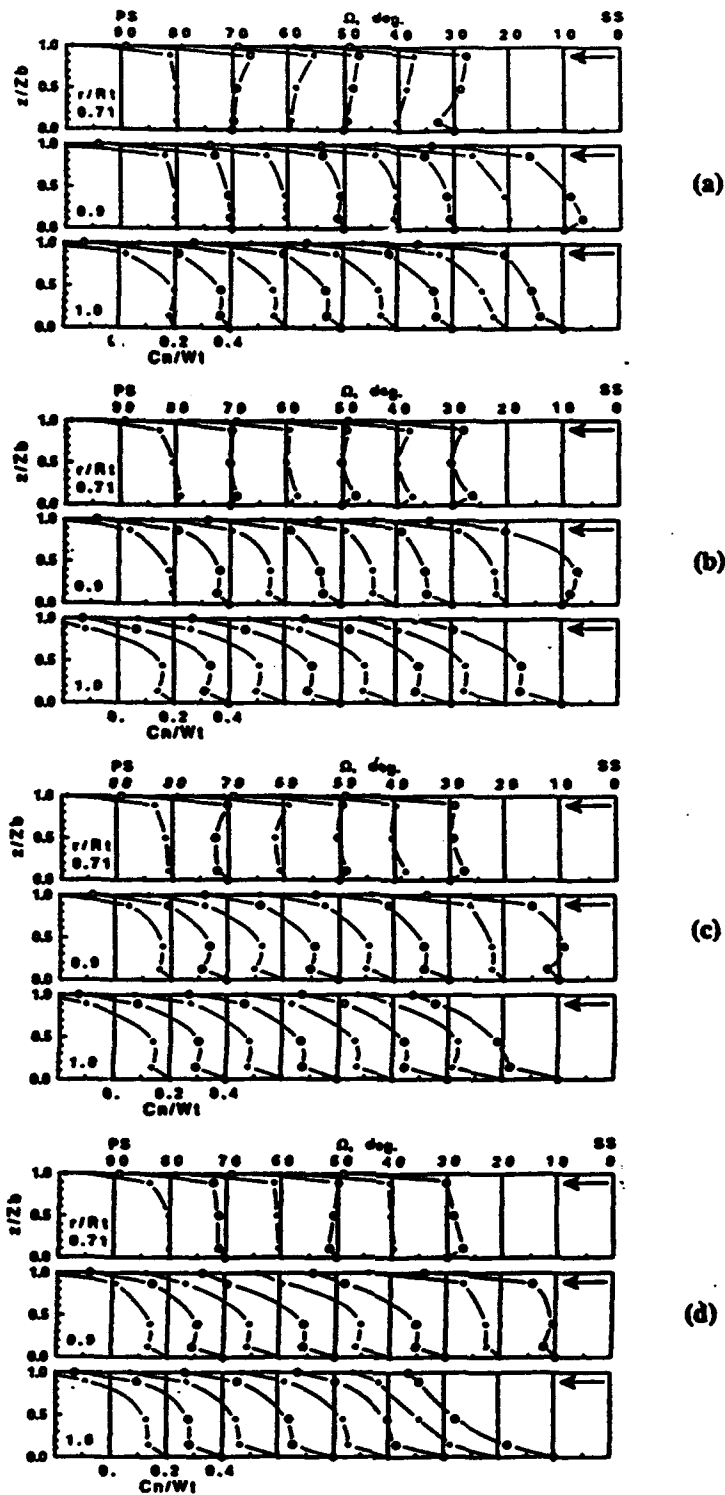


FIGURE 17 Angle-resolved cross-stream mean velocity (C_n/W_t) in an impeller passage measured at $\Psi=330$ degrees with the radial planes of r/R_t of 0.71, 0.9 and 1 and the flow rates of (a) $0.93Q_n$, (b) $0.57Q_n$, (c) $0.29Q_n$ and (d) $0.15Q_n$.

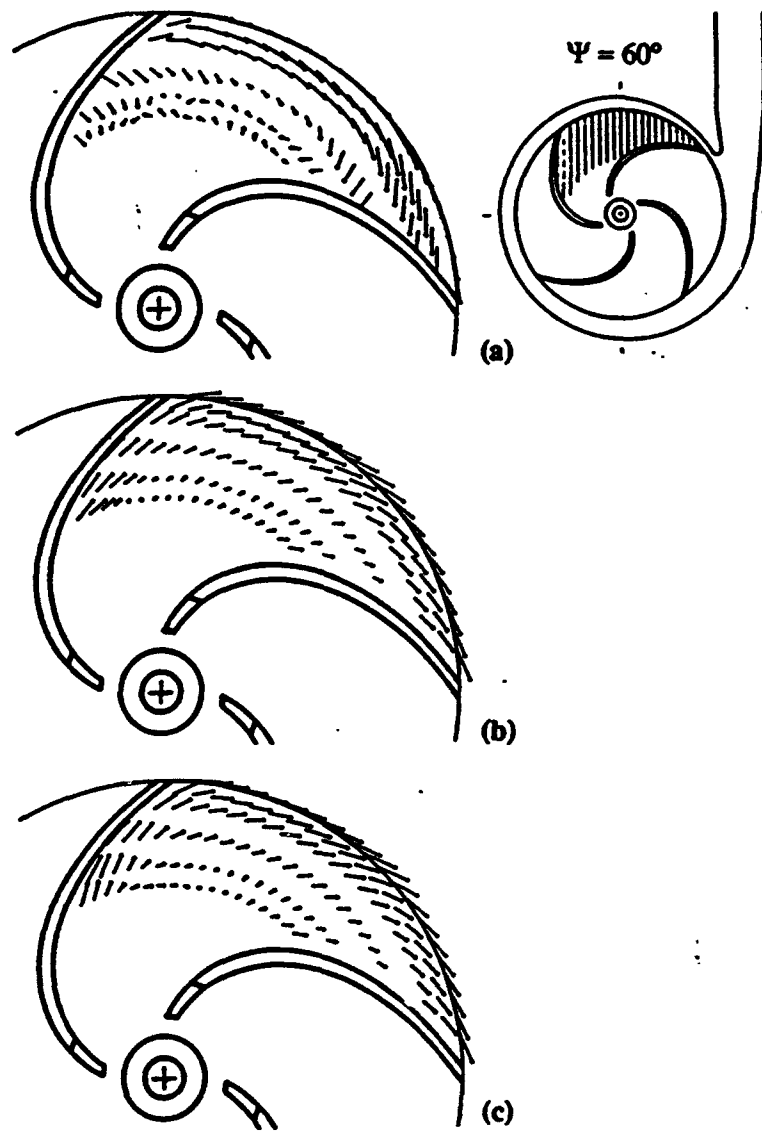


FIGURE 18 Mean velocity vectors of the relative flow in an impeller passage at the flow rate of $0.57Q_n$ measured at $\Psi=60$ and 240 degrees. (see Figure 11 for radial locations)
 (a) plane 1 mm from the shroud
 (b) the mid-plane of the blade height
 (c) plane 1 mm from the impeller hub

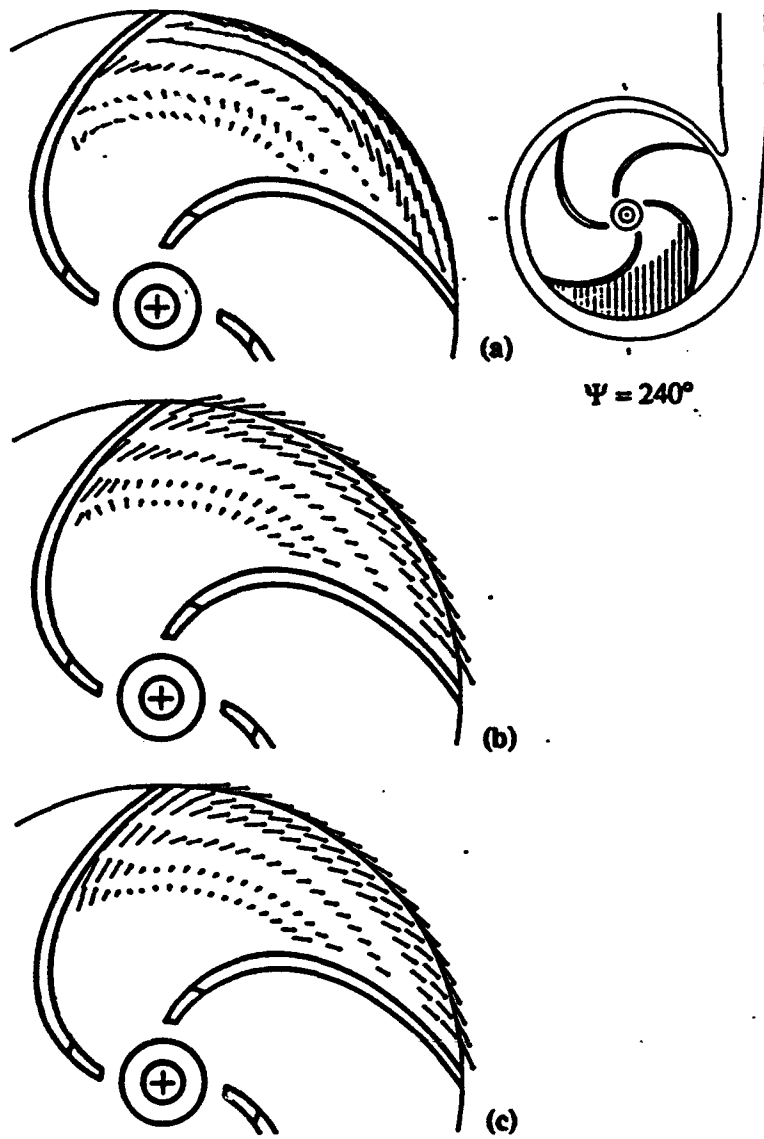


FIGURE 18 Continued.

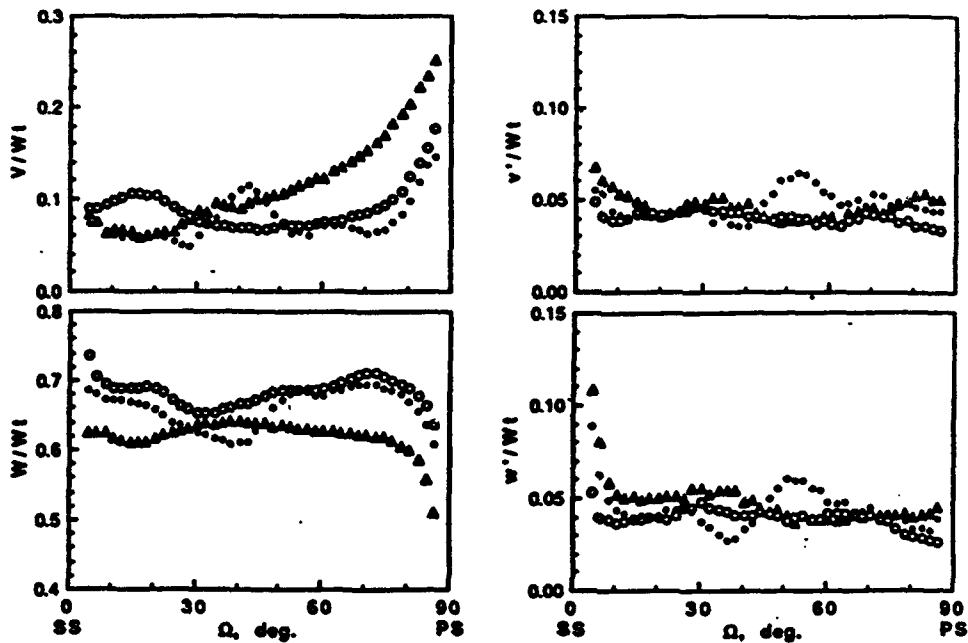


FIGURE 19 Blade-to-blade distributions of angle-resolved radial (V/W_t and v'/W_t) and tangential (W/W_t and w'/W_t) components of mean and rms velocities on the mid-plane of the impeller passage at discharge, $z/Z_1=0.5$ and $r/R_1=1$, at the flow rate of $0.57Q_n$ measured at $\Psi=60$ (\bullet), 240 (\circ) and 330 (Δ) degrees.

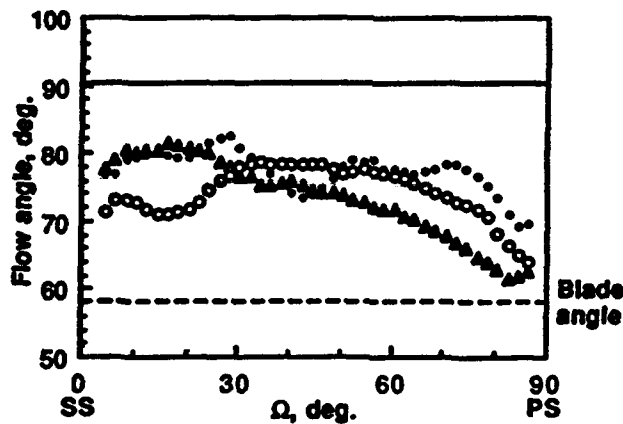


FIGURE 20 Blade-to-blade distributions of flow angle on the mid-plane of the impeller passage at discharge, $z/Z_1=0.5$ and $r/R_1=1$, at the flow rate of $0.57Q_n$ measured at $\Psi=60$, 24 and 330 degrees. (see Figure 19 for symbols)

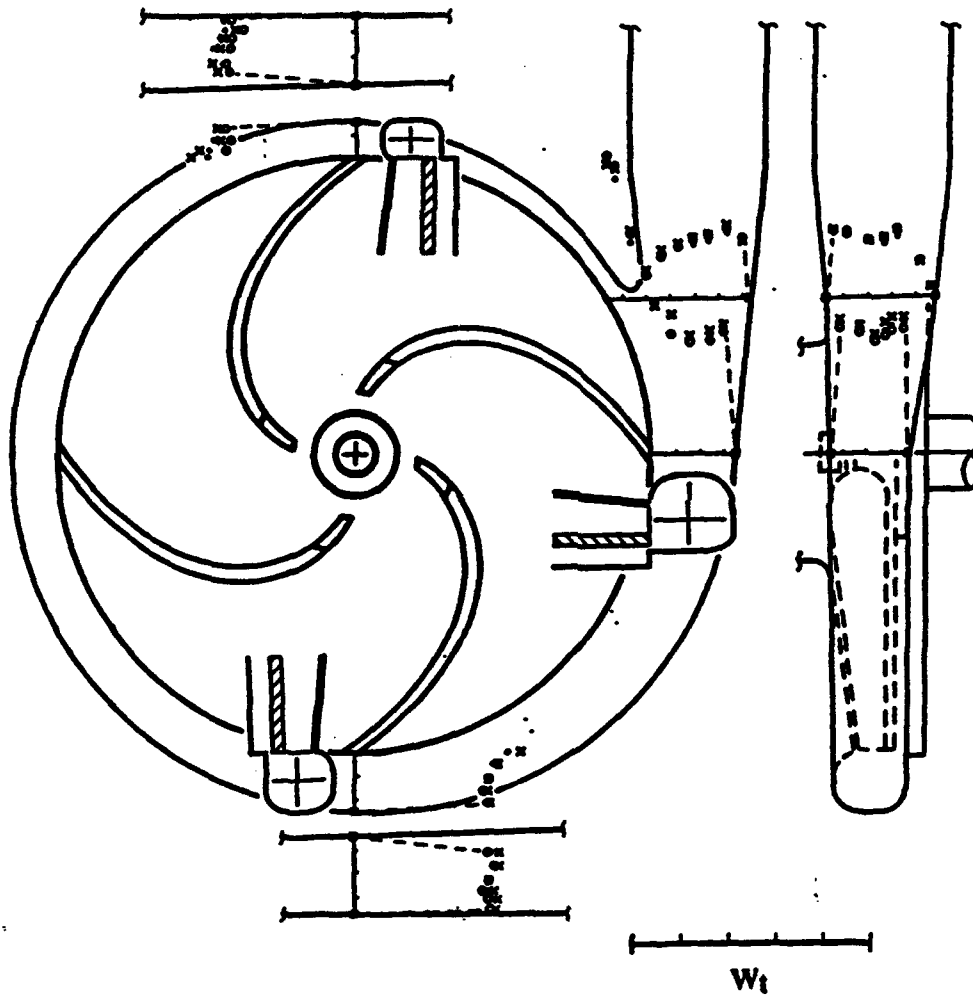


FIGURE 21 Angle-resolved tangential component of mean velocity (W/W_t) in the volute passage at the flow rate of $0.57Q_n$. Impeller shaft angles $\theta=0$ (\circ), 30 (\bullet) and 70 (\times) degrees.

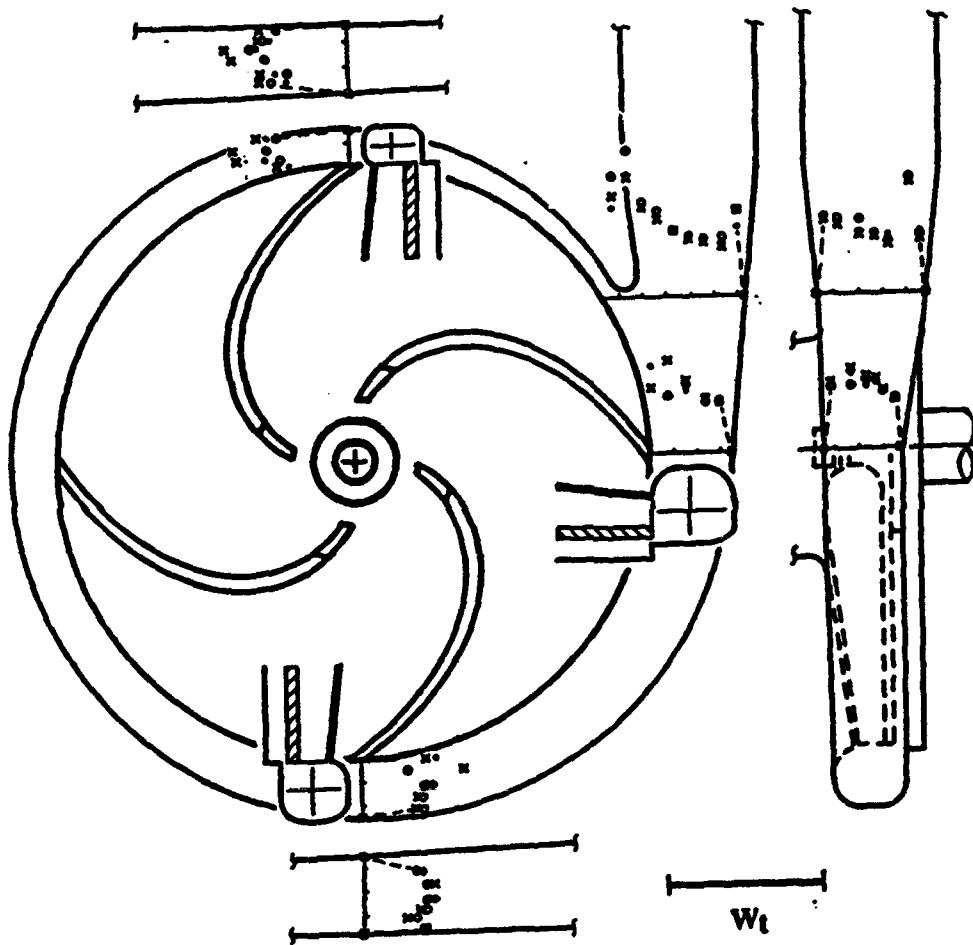


FIGURE 22 Angle-resolved tangential component of rms velocity (w'/W_t) in the volute passage at the flow rate of $0.57Q_n$. (see Figure 21 for symbol)

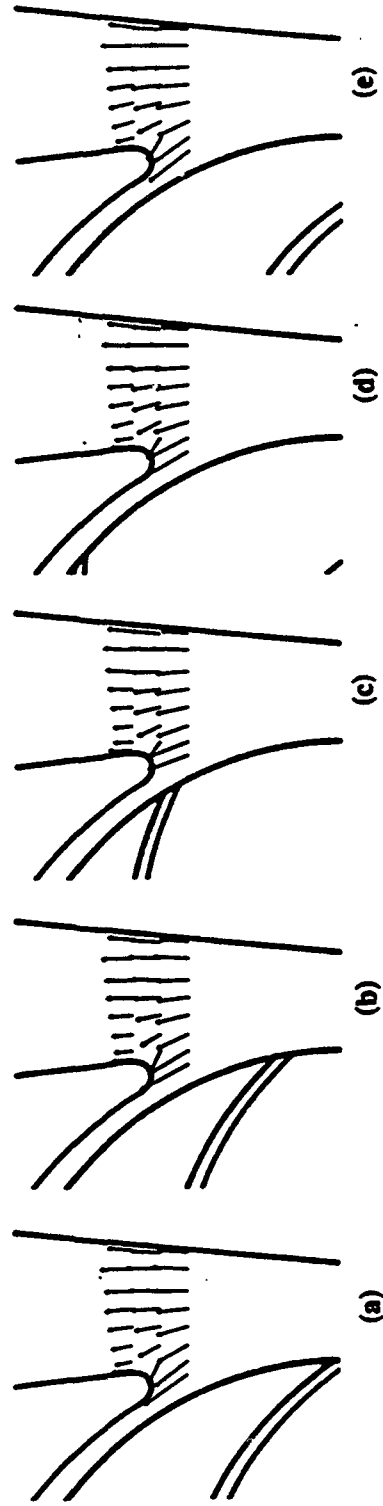


FIGURE 23 Mean flow vectors on the plane of $z=0$ close to the cutwater at the flow rate of $0.57Q_n$. Impeller shaft angles $\phi =$ (a)0, (b)10, (c)30, (d)50 and (e)70 degrees.

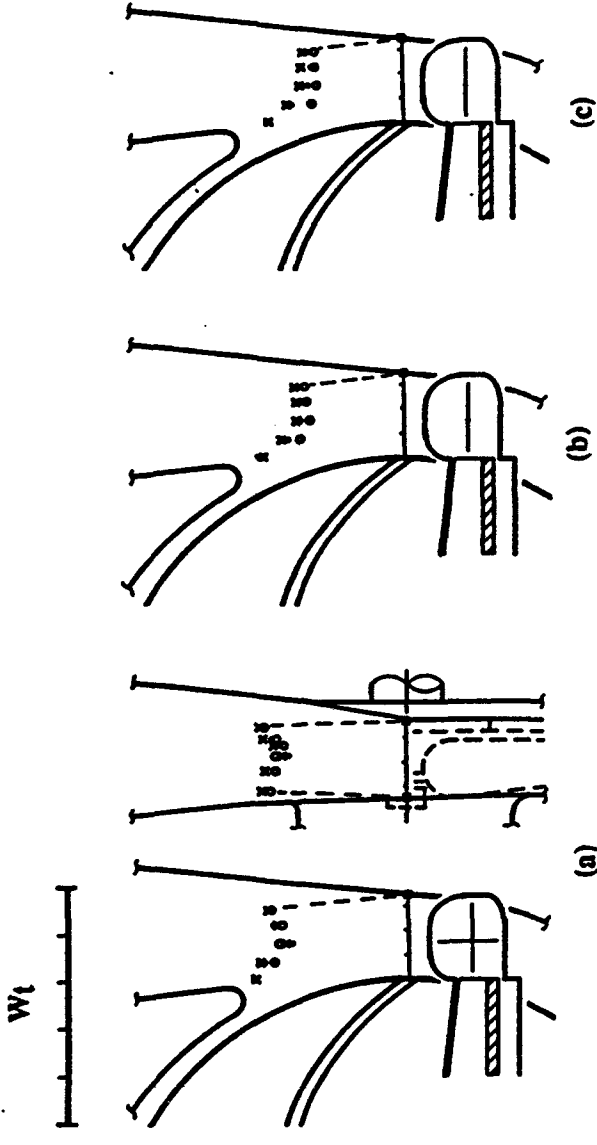


FIGURE 24 Angle-resolved tangential component of mean velocity (W/W_t) in the volute passage measured at ψ of 330 degrees with the flow rates of (a) $0.93Q_n$, (b) $0.29Q_n$ and (c) $0.15Q_n$. (see Figure 21 for symbols)

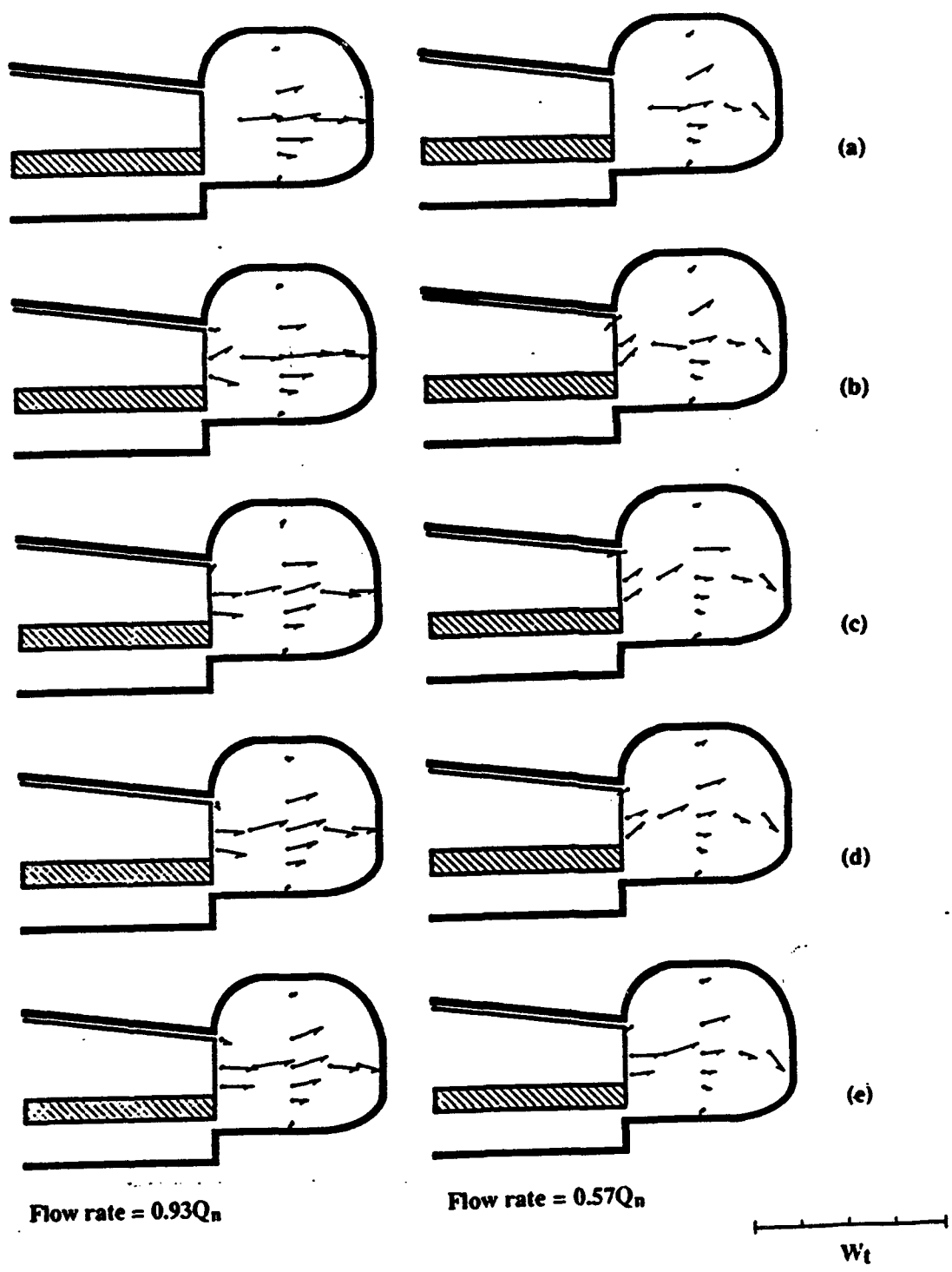


FIGURE 25 Cross-stream mean flow in the volute on the plane of $\Psi=330$ degrees at the flow rates of $0.93Q_n$ and $0.57Q_n$. Impeller shaft angles $\phi=(a)0$, (b)10, (c)30, (d)50 and (e)70 degrees.

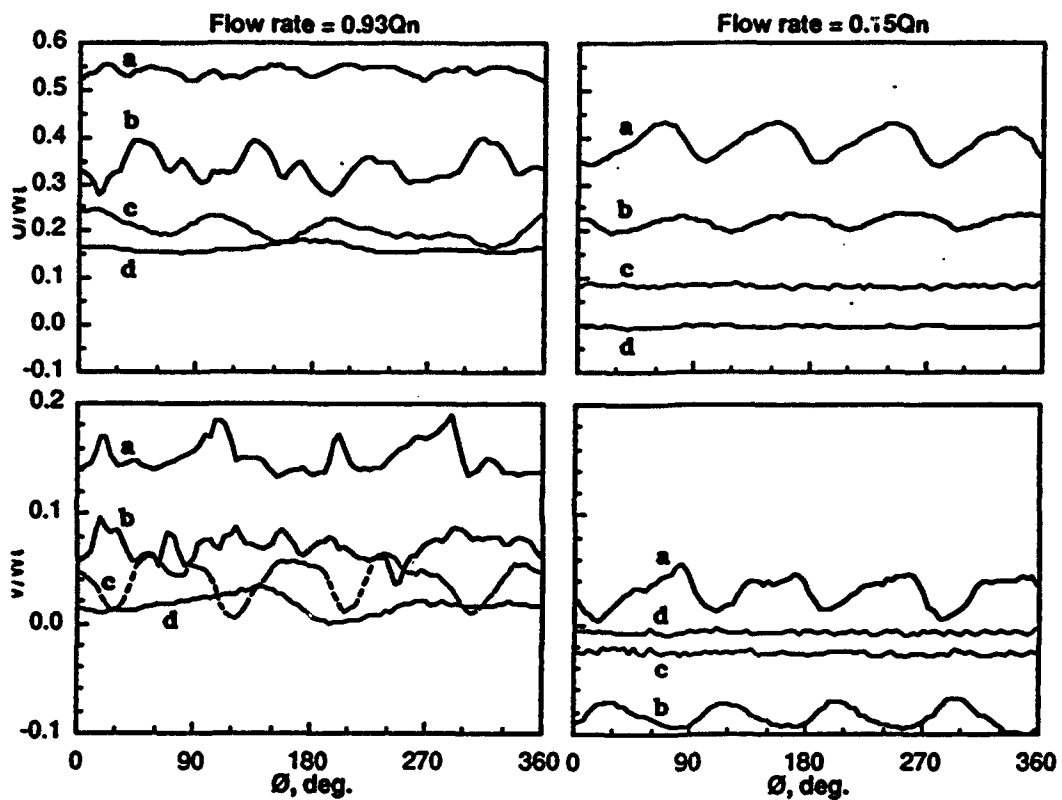


FIGURE 26 Angle-resolved axial (U) and radial (V) components of mean velocity traces on the centreline of the exit pipe at axial locations $x/D_e=(a)0, (b)1, (c)1.8$ and $(d)3.2$.

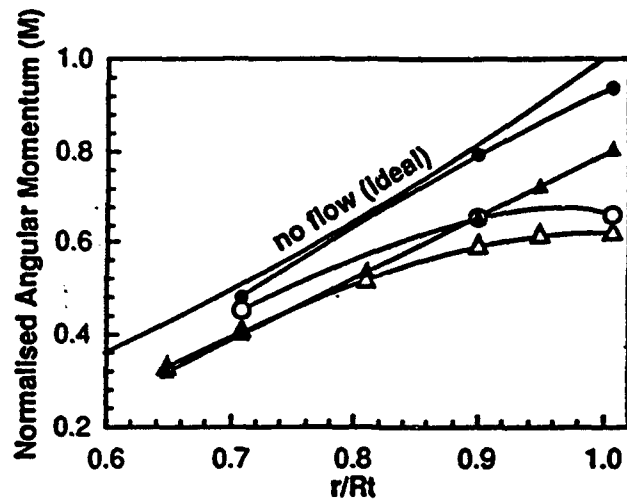


FIGURE 27 Radial distributions of angular momentum (M) at the flow rates of $0.93Q_n$ (Δ , \triangle) and $0.29Q_n$ (\circ , \bullet). (open symbol: experiment; block symbol: theoretical value)

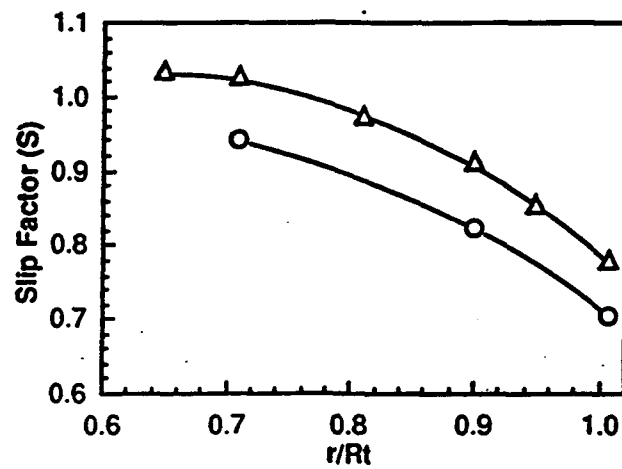


FIGURE 28 Radial distributions of slip factor (S) at the flow rates of $0.93Q_n$ (Δ) and $0.29Q_n$ (\circ).

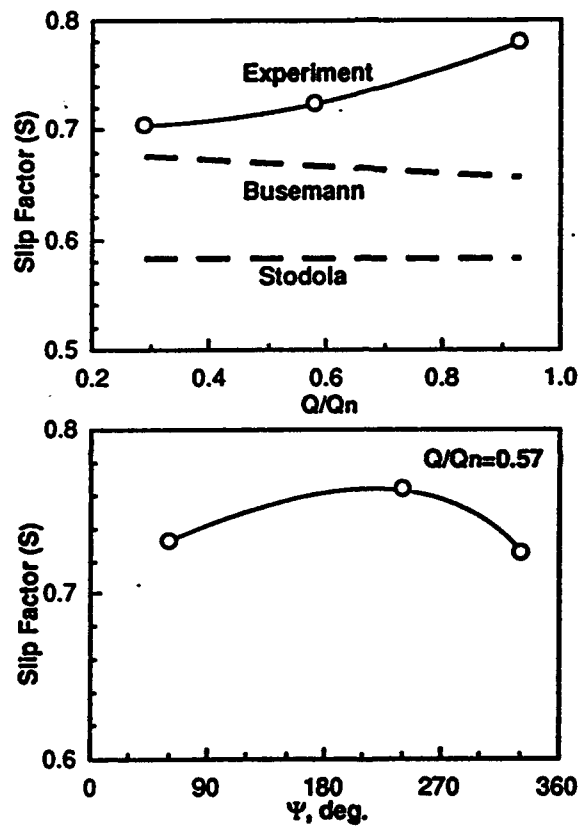


FIGURE 29 Variations of slip factor (S) with flow rate and volute circumferential angle at impeller discharge, $r/R_t=1$.

Scientific Research Associates, inc.

50 Nye Road, P.O. Box 1058
Glastonbury, Connecticut 06033
(203) 659-0333 FAX (203) 633-0676
January 28, 1994

Dr. Edwin P. Rood
Code 1132F
Scientific Officer
Fluid Mechanics Division
Office of Naval Research
800 North Quincy St.
Arlington, VA 222117

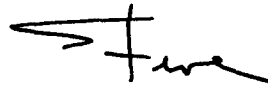
Subject: Contract N00014-91-C-0172; Final Report

Dear Ed:

Enclosed is the Final Report for the subject Contract. We are making final distribution in accordance with the distribution list in the Contract, as per SRA's recent conversation with Earl Quandt. Also enclosed is a DD250. As you know, final payment requires indication of acceptance of the Final Report by the Navy by completing the DD250. Please complete Block 21B and return the DD250 to us, with a copy to the addresses in Blocks 10 and 12. We have submitted our final DD882, Patent Report, to DCMAO and we believe that all contractual obligations have now been met and the contract is physically complete.

We believe this has been a fruitful program, and that the results will provide valuable information to ONR scientists relative to centrifugal pump design. We look forward to the opportunity to work with your group again. Please call me if we can be of service.

Very truly yours,



Stephen J. Shamroth
President

SJS:jc
Enclosures
cc: Director, Naval Research Laboratory
Code 2627
Washington, DC 20375

DTIC (2 copies)
Bldg. 5, Camerson Station
Alexandria, VA 22304-6145

ACO - DCMAO - Hartford (cc transmittal letter)